The Dissertation Committee for Brian Matthew Gawlik Certifies that this is the approved version of the following Dissertation:

Spectral Imaging for High-Throughput Metrology of Large-Area Nanostructure Arrays

Committee:

S.V. Sreenivasan, Supervisor

Edward T. Yu, Co-Supervisor

Dwayne Labrake

Dragan Djurdjanovic

Yaguo Wang

Spectral Imaging for High-Throughput Metrology of Large-Area Nanostructure Arrays

by

Brian Matthew Gawlik

Dissertation

Presented to the Faculty of the Graduate School of

The University of Texas at Austin

in Partial Fulfillment

of the Requirements

for the Degree of

Doctor of Philosophy

The University of Texas at Austin

December 2019

Acknowledgements

This work is based upon work supported by the National Science Foundation under Cooperative Agreement No. EEC-1160494 and the Scalable Nanomanufacturing Program (NSF Contract No. ECCS-1120823). Any opinions, findings and conclusions or recommendations expressed in this material are those of the author(s) and do not necessarily reflect the views of the National Science Foundation. I would also like to thank the T. W. Whaley, Jr. Friends of Alec Endowed Scholarship in the Cockrell School of Engineering for funding me throughout many semesters of my PhD.

Abstract

Spectral Imaging for High-Throughput Metrology of Large-Area Nanostructure Arrays

Brian Matthew Gawlik, PhD

The University of Texas at Austin, 2019

Supervisor: S.V. Sreenivasan

Co-supervisor: Edward T. Yu

Modern high-throughput nanopatterning techniques such as nanoimprint lithography make it possible to fabricate arrays of nanostructures (features with dimensions on the 10's to 100's of nm scale) over large area substrates (in^2 to m^2 scale) such as Si wafers, glass sheets, and flexible roll-to-roll webs. The ability to make such large area nanostructure arrays, or "LNAs" as we will call them, gives birth to an extensive design space enabling a wide array of applications. For instance, LNAs exhibit nanophotonic properties enabling optical devices like wire-grid polarizers (WGPs), transparent conducting metal mesh grids (MMGs), color filters, perfect mirrors, and anti-reflection surfaces. LNAs can also be utilized for increasing surface area as well as generally creating large arrays of discrete features to be utilized as building blocks for electronic components in memory storage devices, sensors, and microprocessors. These unique properties make

LNAs immediately attractive to certain industries such as the display and photovoltaic industries.

As fabrication methods for LNAs are becoming viable, various industries are becoming interested in pursuing high-volume manufacturing of LNAs for these applications. Unfortunately, metrology methods are currently rudimentary outside of the silicon integrated circuits industry, impeding manufacturing scalability in applications such as displays and photovoltaics. Metrology is essential in the manufacturing context, because it provides invaluable feedback on the success of the fabrication process, both during new process development and large-scale production by tracking of device quality metrics, including performance and reliability metrics, and enables classification of defects that cause devices to not achieve desired quality metrics.

Traditional nanometrology methods have fundamental issues which make their applicability to LNA manufacturing difficult. In particular, their low throughput is a major deal-breaker. Fortunately, the nanophotonic properties of LNAs offer a convenient basis for metrology which offers the potential to bridge the gap between the macro and nano scales. This is because the nanophotonic properties of LNAs are inherently geometry dependent, meaning that the optical effects observed from LNAs on the macroscale give direct insight into what is happening on the nanoscale. These optical properties can be characterized using spectral imaging methods such as RGB color imaging, multispectral imaging, and hyperspectral imaging. The throughput of these systems can be extremely high relative to traditional metrology approaches. For instance, a hyperspectral imaging system, when optimized, can achieve throughput of 2.6 m^2/hr with 61 spectral bands

(wavelength centers of 400 to 700 nm in steps of 5 nm) and a resolution of 10 x 10 μm. An RGB imaging system can achieve an even higher throughput of 15.3 m^2/hr. The 10 x 10 μm lateral resolution is often adequate for display and photovoltaic applications. The high throughput makes this approach is incredibly attractive.

In this dissertation, we show how spectral imaging techniques can be applied to metrology characterization tasks including defect detection and classification as well as providing a geometric measurement capability *via* a technique called optical critical dimension (OCD) scatterometry. In this work, we utilize exemplar manufacturing methods, namely JFIL nanoimprint lithography, to create a variety of exemplar LNAs on which we demonstrate the various metrology capabilities of spectral imaging. These LNAs include plasma etched vertical Si nanopillar arrays, metal assisted chemical etching (MACE) vertical Si nanowire arrays, WGPs, and MMGs. Each of these devices has unique manufacturing processes, and we show how the various manufacturing process steps can create a variety of different defects. Naturally, many of the defects originate in the nanoimprint process which lithographically defines the features. We show how defects like particle contamination, non-filling, residual layer thickness (RLT) variations, and adhesion failure uniquely manifest as changes in the optical signatures of the LNAs and use this principle to provide a basis for defect detection. Then, we show how image processing methods can be used to classify what types of defects have occurred over large areas such as wafer scale. Furthermore, we demonstrate that spectral imaging can be used as a geometric metrology using the OCD method, and show how hyperspectral imaging, in particular, can provide geometric measurement on wafer scale areas. The large field of

view (FOV), high spatial resolution, and high speed offered by the spectral imaging approach allows for identification of a variety of interesting defect signatures that would be difficult, or nearly impossible, to observe using other metrology approaches. Finally, we discuss ongoing development of a spectral imaging system for roll-to-roll (R2R) LNA manufacturing. Construction of this system will begin in the months following this dissertation and will primarily be applied to manufacturing of WGPs and MMGs on R2R.

In summary, these demonstrations are intended to serve as a demonstration of the use of spectral imaging wherever possible in LNA manufacturing. Naturally, this requires that the LNAs being manufacturing exhibit significant enough optical effects for the approach to work, but when this is the case, the advantages of the approach appear outstanding and thus have the potential to be utilized in volume manufacturing of LNAs.

Table of Contents

List of Tables

List of Figures

Table of Acronyms

Acronym	***Full name*, description**
CD	*Critical Dimension*
CD-SEM	*Critical Dimension Scanning Electron Microscopy*
FDTD	*Finite Difference Time Domain*
FOV	*Field of View*
HSV	*Hue, Saturation, Value*. Used to refer to the HSV color space or images (i.e an HSV image) which are in the HSV color space.
LCD	*Liquid Crystal Display*
LNA	*Large-Area Nanostructure Array*
MACE	*Metal Assisted Chemical Etching*
MMG	*Metal Mesh Grid*
OCD	*Optical Critical Dimension*
OSPS	*Object Space Pixel Size*. This refers to the size of the pixel in object space (as opposed to image space) in an spectral imaging system. It is the size of the pixel in image space (the size of a camera's pixel) divided by the magnification of the camera lens.
R2R	*Roll-to-Roll*
RGB	*Red, Green, Blue*. Used to refer to the RGB color space or images (i.e. an RGB image) which are in the RGB color space.
RLT	*Residual Layer Thickness*
ROI	*Region of Interest*
SEM	*Scanning electron microscope*. Refers to the instrument the Scanning Electron Microscope or the images taken by this instrument Scanning Electron Micrographs.
WGP	*Wire-Grid Polarizer*

Chapter 1: Introduction to Large Area Nanostructure Arrays and the Need for High-Throughput Metrology Systems

BACKGROUND

Modern high-throughput nanopatterning techniques such as nanoimprint lithography [1] make it possible to fabricate arrays of nanostructures (features with dimensions on the 10's to 100's of nm scale) over large area substrates (in^2 to m^2 scale) such as Si wafers and flexible roll-to-roll webs. The ability to make such large area nanostructure arrays, or "LNAs" as we will call them, gives birth to an extensive design space enabling a wide array of applications. For instance, LNAs exhibit nanophotonic properties enabling optical devices like wire-grid polarizers (WGPs) [2], transparent conducting metal mesh grids (MMGs) [3–5] , color filters [6–8], perfect mirrors [9], and anti-reflection surfaces [10–14]. LNAs can also be utilized for increasing surface area as well as generally creating large arrays of discrete features to be utilized as building blocks for electronic components in memory storage devices [15–17], sensors, and microprocessors.

These unique properties make LNAs immediately attractive to certain industries. The display industry, for example, has its eyes set on making use of WGPs and MMGs. WGPs promise power efficiency gains in liquid crystal displays (LCDs) and MMGs offer a cost-effective and flexible alternative to Indium Tin Oxide (ITO) as a transparent conducting layer. Applications may also exist in photovoltaics since LNAs can help tailor absorption profiles, either for broadband efficiency increase [12–14] or the generation of colored solar cells for decorative purposes [18–22]. Meanwhile, vertical nanowire/nanopillar arrays are being heavily researched for a breadth of applications including gas sensing [23–

This chapter includes significant discussion of hourglass shaped Si nanopillar arrays which were discussed extensively in our publication Gawlik et. al 8. In this work Gawlik conceived the idea, did most of the experimental and simulation work, and wrote most of the paper. Cossio and Kwon did most of the work in the sections regarding the angular dependence. Kwon also ran simulations to further angular dependence discussion in the appendix. Jurado and Palacios helped with fabrication of samples. Singhal offered help and guidance as well as editing help. Alu, Yu, and Sreenivasan helped with mentorship, editing, and direction.

[25], optical sensing [26–28], battery technology [29], ultracapacitor applications [30,31], and memory [15–17], as well as color filtering for printing [6,8], displays, and imaging devices [28].

Now that fabrication methods are viable, various industries are becoming interested in pursuing high-volume manufacturing of LNAs for these applications. Unfortunately, metrology methods are currently rudimentary, impeding manufacturing scalability. Metrology is essential in the manufacturing context, because it provides invaluable feedback on the success of the fabrication process, both during new process development and large-scale production. Metrology enables tracking of device quality metrics, including performance and reliability metrics, and enables identification of defects that cause devices to not achieve desired quality metrics. Metrology also provides a means for establishing the exact root-causes of defects which enables enhancement of yield defined as the percentage of fabricated devices that meet desired quality metrics. Sufficiently high yield is critical for cost-effective manufacture of LNAs.

Industries will need to adopt new metrology methods for LNA manufacturing in order to successfully scale, and these metrology methods must meet the unique demands of LNA manufacturing. This research sets out to respond to this need by establishing an effective metrology infrastructure for LNA manufacturing.

PROBLEMS WITH TRADITIONAL METROLOGY APPROACHES AS APPLIED TO LNAS

LNA manufacturing presents a uniquely challenging scenario for metrology, because cost effective manufacturing of LNAs will naturally trend towards extremely high throughput. This stems from the fact that many applications of LNAs are inherently on the

m^2 scale and require costs that are at or below \$50/m^2. Individual displays, for instance, are on the m^2 scale, made by the millions, and routinely sell for merely several hundred dollars. The individual device layers in the display, such as a WGP, need to be considerably less costly. These cost pressures combined with high capital costs of advanced manufacturing equipment require the manufacturing throughput to be high, on the order to 100 m^2/hr. Other applications, such as solar panels and smart windows, suggest that LNAs will need to be produced at high speeds and high yields. If LNA manufacturing becomes mature it may not be uncommon to see manufacturing of multi-meter-wide rolls happening at meter per minute rates, and at >95% yields. LNA metrology needs to be fast across large areas while maintaining suitably high spatial resolution so that it can catch small defects and resolve subtle area-to-area variations. The sheer scale of this manufacturing application asks a lot of metrology systems, nonetheless the challenge must be met, because it is critical to the success of LNA manufacturing.

Historically, particularly in the semiconductor industry, the primary metrology approach for all things micro – and eventually nano – has been microscopy, in which the geometry of individual features is measured directly either with beams of light or electrons. For as long as transistor feature sizes remained large enough to be resolved using optics, optical light microscopes were used, but as feature sizes became smaller than the diffraction limit of light the industry had to transition to using scanning electron microscopy (SEM) and occasionally atomic force microscopy (AFM). So-called CD-SEMs (critical dimension - scanning electron microscopes) are used for in-line top-down measurements in the semiconductor industry today. Off-line SEMs and AFMs are used for

more thorough investigations of defects, which often involves destructive cleaving or ion beam milling of the samples.

Despite their importance to the semiconductor industry, microscopy approaches like SEM and AFM don't apply well to LNAs for a few reasons. For one, their throughput is extremely low, because their characterizations are limited to fields of view (FOVs) which are micron-scale. It is not hard to imagine how slow these techniques will be in the context of the potentially square-meter areas of LNAs. Furthermore, 3-dimensional SEM measurements often require sample destruction – such as in the case of cross-sectional SEM – which makes it ineffective for quality inspection of outgoing products. Finally, because AFM involves near physical contact with features, it may be inherently destructive for device features, particularly at higher throughputs.

Optical Critical Dimension (OCD) Scatterometry, also known simply as scatterometry, is an optical metrology technique which has also been utilized extensively by the semiconductor industry that allows for non-destructive geometric characterization at relatively fast speeds and large areas compared to microscopy approaches [32]. OCD measures angle or wavelength-resolved reflectance from areas on a sample (typically ~1 mm in diameter) and infers the average local geometry of the features in this area through inverse modeling of the optical behavior of the features. Compared to microscopy, the FOV of OCD is relatively large, giving it a significant throughput advantage over microscopy. However, traditional scatterometry systems would still be very slow if applied to LNAs since they are limited to measuring individual spots on a sample sequentially, point-by-

point. It is easy to see how traditional scatterometry will be slow even for a somewhat relaxed spatial resolution characterization of an LNA…

Thought experiment: *Imagine characterization of a 1 m^2 LNA device with a scatterometer. Let us say, we want to do the characterization with a spatial resolution of 100 µm. Let's assume this scatterometer can measure an individual point in 1 second. The characterization will require 100 million individual points to be measured which would take about 3 years and 2 months to complete. In order for such a characterization to be done in a timely manner, let's say in about 100 seconds, the individual measurements would need to be done a million times faster. Optical sensing can happen on these time scales, but time spent moving between different system states like angles or spectral bands, as well as the time spent moving between each of the 10^8 individual areas on the sample must be taken into account as well. This is a tall order.*

SPECTRAL IMAGING METROLOGY FOR LNA MANUFACTURING

Clearly, traditional metrologies have fundamental issues which make their applicability to LNA manufacturing difficult. In particular, their low throughput is a major deal-breaker. Ideally, metrology systems for LNAs would be capable of assessing yield over large areas, very quickly. However, in the context of LNAs, this seems like an exceptionally difficult task based on the vast disconnect between the need for nanoscale measurement and the large macro scales that the actual devices comprise.

Fortunately, there is a saving grace – the nanophotonic properties of LNAs offer a convenient basis for metrology which bridges the gap between the macro and nano scales.

This is because the nanophotonic properties of LNAs are inherently geometry dependent, meaning that the optical effects observed from LNAs on the macroscale give direct insight into what is happening on the nanoscale. The color of nanopillar arrays, for instance, is highly structure dependent. Different shapes of nanopillars give completely different colors, and within the context of a specific shape – a cylinder, for instance – small, changes in the geometry of the arrays (i.e. height or diameter) cause visible changes in the color. For this very reason, nanopillar arrays have been extensively researched as a novel approach to color filtering [6,33], but this serves a dual purpose as a characterization approach.

Throughout our work, we have explored structural coloration using a variety of different nanopillar and nanowire arrays. In particular, one such structure – hourglass shaped nanopillar arrays – helped us acquire deep insight into the connection between nanophotonic effects and macroscale optical characteristics [8]. These nanopillars were initially fabricated by accident. During a routine plasma etch run of a crystalline Si wafer, we attempted to etch a simple array of cylindrical nanowires. To our surprise, when our first wafer emerged from the etch chamber it had a vibrant blue color, something we had not seen before. Cross-section SEM revealed that the nanopillars we etched had the hourglass shape such as the one seen in the cross-section SEM image in Figure 1a. It appeared that the etch had caused a significant amount of "necking" in the pillar due to an unexpected lateral etch component creating the hourglass profile.

Electromagnetic simulations done with an electromagnetics modelling tool Lumerical FDTD (finite difference time domain) revealed that the hourglass shape was integral to creating the vibrant color we saw on the wafer and that cylindrical nanopillars

with similar geometry aside from the neck would result in very different reflectance characteristics. The hourglass shape acted to suspend the head of the pillar above the substrate, as if it was floating, causing it to support what is called a Mie resonance [34] which causes one wavelength to be selectively reflected and others absorbed. This causes the arrays to exhibit reflectance spectra like the ones seen in Figure 1c which has a strong resonant peak. The resonant peak position and magnitude is very sensitive to the exact geometry of the nanopillars in the array and predominantly is what defines the hue and brightness of the color observed from the arrays. The color is so sensitive to the geometry that a variation in the diameter of just ~10-20 nm can change the color of a wafer from blue to green. This allowed us to estimate the geometry of the nanopillars across an entire wafer simply by looking at the wafers with our eyes.

Naturally, we took many pictures of the wafers with cameras as well for documentation some of which are shown in Figure 1. These pictures captured an enormous amount of information about the yield and defectivity that had occurred on each of these wafers. Visual analysis of the pictures could quickly tell us whether necking had occurred, and if it had, the average diameter of the head of the pillar to ± 10 nm. Naturally, patterning defects like particle contamination and scratches were plainly obvious as well.

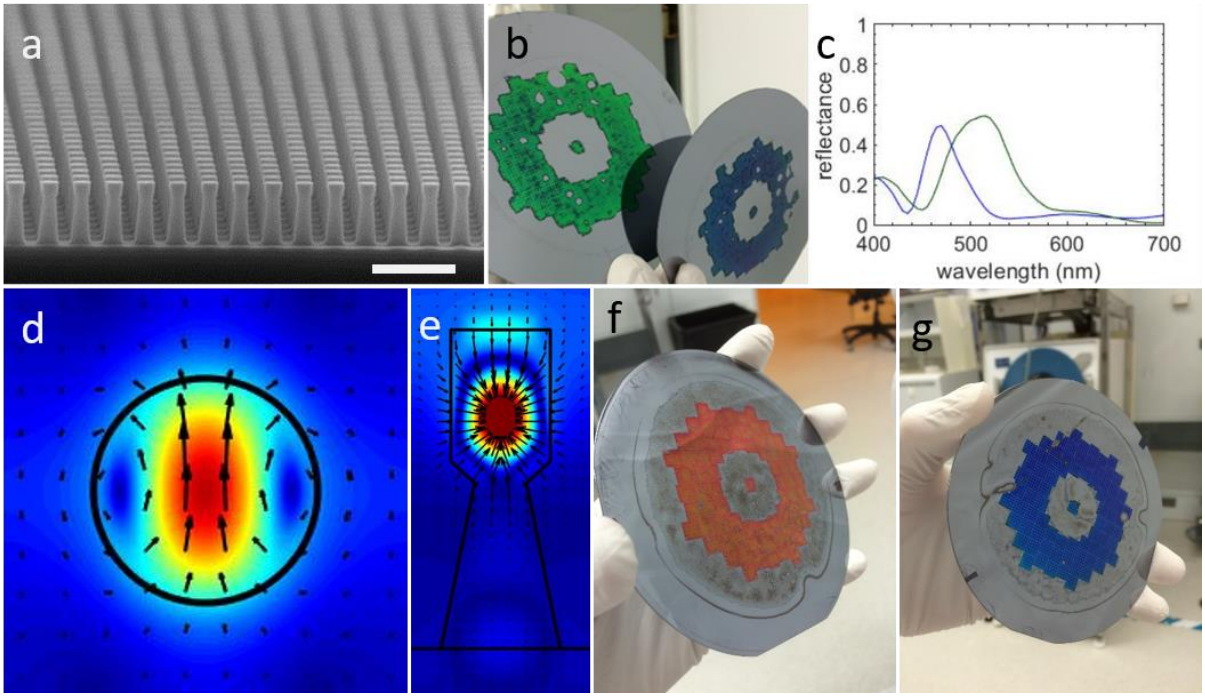

Figure 1. Hourglass shaped Si nanopillars and their spectral signatures. (a) cross-section SEM image of hourglass shaped nanopillar arrays which produce the blue color seen in (b). (b) photograph of 100 mm wafers containing hourglass shaped Si nanopillar arrays. (c) Reflectance spectra from the colored areas in the wafers in (b). (d,e) simulated magnetic field plots for the hourglass shaped nanopillar. (f,g) more photographs of wafers containing the hourglass arrays.

These images made it very clear that a formal version of this approach would be extremely powerful, revealing practically everything that we desired to know about these wafers over large areas – nanoscale geometry and patterning defects. Naturally, a formal implementation of this system would take the form of a spectral imaging system or an imaging spectrophotometer, which could take images of these wafers at specific wavelengths allowing for spectra to be recorded in an imaging fashion.

Different Types of Large Area Nanostructure Arrays and Their Optical Effects

Of course, the hourglass-shaped nanopillar arrays discussed previously are not the only structures we are interested in, but a range of LNAs exist which also exhibit nanophotonic properties. We will use these LNAs to demonstrate spectral imaging metrology solutions throughout this dissertation, so it is necessary to provide some background on these structures.

Wine glass Shaped Silicon Nanopillar Arrays

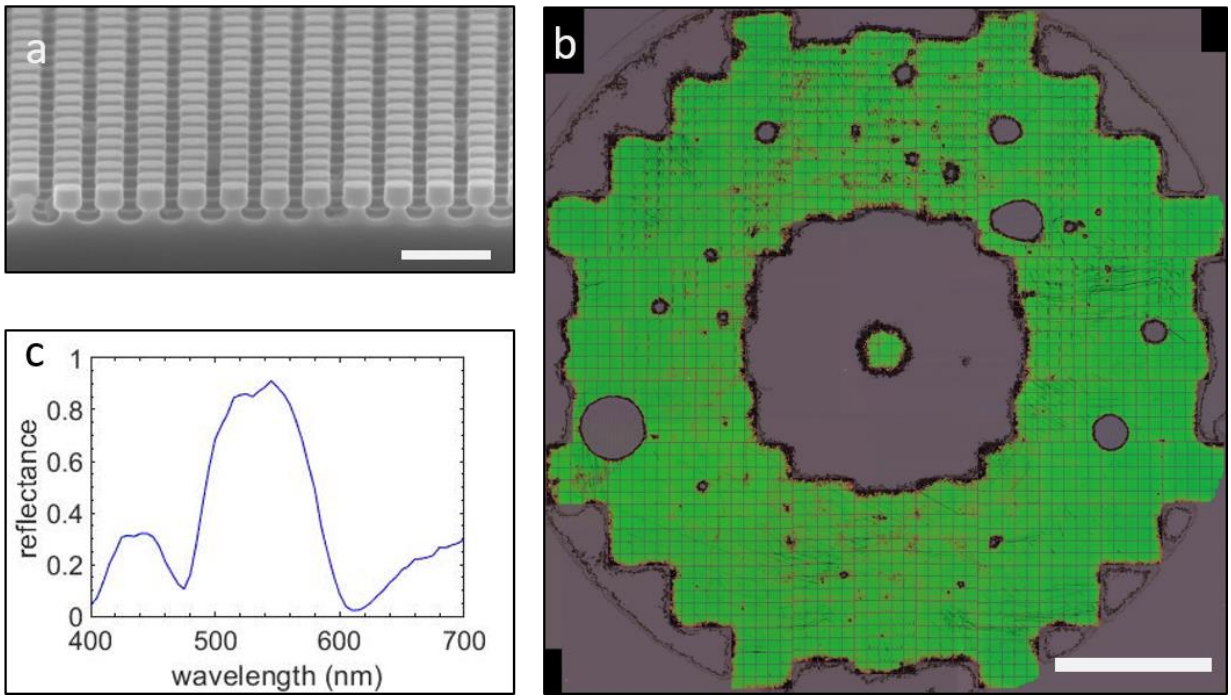

Figure 2. Wine glass Shaped Silicon Nanopillar Arrays. (a) Cross-section SEM image of wine glass nanopillars array (scale bar = 400 nm). (b) RGB image of a 100 mm wafer containing wine glass arrays (scale bar = 1 cm). (c) Characteristic reflectance spectra exhibited by the wine glass arrays.

The necking effect that happens in the hourglass nanopillars etch process unfortunately proved to be fairly unrepeatable. In an effort to formalize the creation of the

suspended Mie resonator structure, we pursued a more rigorous fabrication process. This pursuit ended with creation of a similar suspended resonator structure, but having a shape more resembling a wine glass. The cross-section SEM image in Figure 2a shows the general shape of the wine glass structure – a cylindrical head suspended on a short, stem like body. These structures are fabricated with a two-step Bosch-like etch process which we will detail in Chapter 4 before utilizing the sample for a metrology demonstration.

The wine glass arrays exhibit a very similar Mie resonance effect to the hourglass arrays, exhibiting bright, vibrant colors like the green color seen on the wafer shown in Figure 2b. Naturally, the reflectance spectra, which is shown in Figure 2c, is quite similar to that exhibited by the hourglass arrays, having a large, pronounced peak corresponding to the Mie resonance. The color and spectra exhibited by the arrays are extremely sensitive to variations in geometry, and thus can be utilized very effectively for identifying pattern defects and geometric variations. This wafer, for instance, has many visible defects including the large voids and dark edges. Other, more subtle variations exist as well. We will utilize this wafer of wine glass arrays extensively in Chapter 4 for development of detection and classification of patterning defects.

Vertical Si Nanowire Arrays Made with Metal Assisted Chemical Etching (MACE)

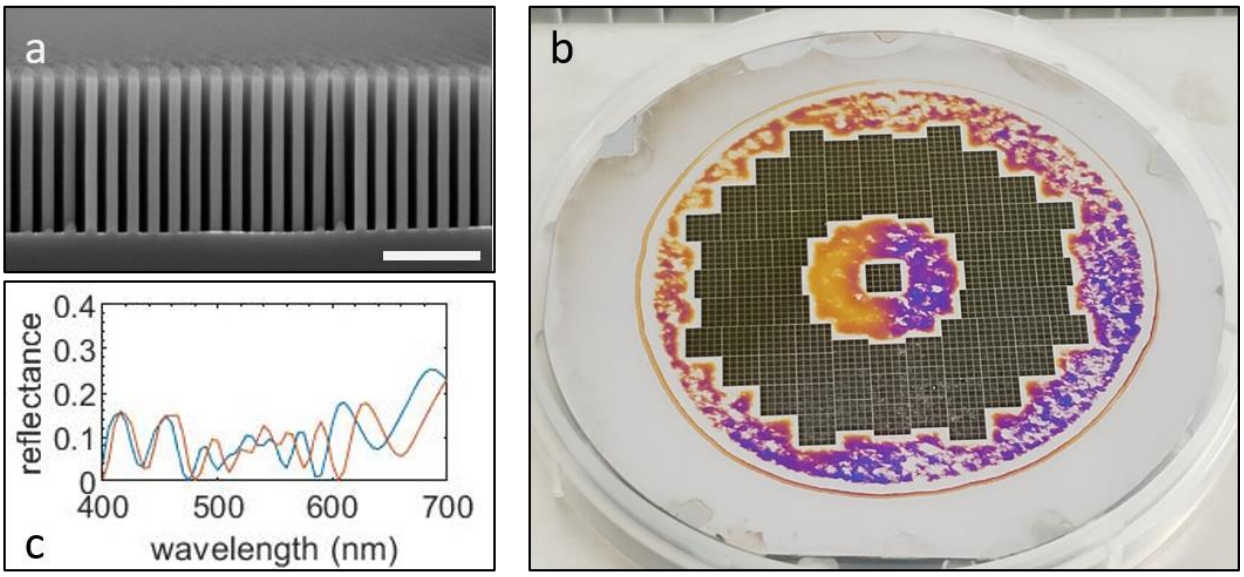

Figure 3. Vertical Si Nanowire Arrays. (a) Cross-section SEM Image of vertical nanowire arrays created with metal assisted chemical etching (MACE) (scale bar = 1 um). (b) Photograph of a 100 mm wafer of MACE-etched nanowire arrays. (c) Simulated spectra for nanowire arrays having height = 1000 nm and diameters of 100 and 105 nm.

As mentioned, Si nanowire arrays have applications in gas sensing [23–25], optical sensing [26–28], battery technology [29], ultracapacitor applications [30,31], memory [15–17], as well as imaging devices [28]. Figure 3a shows a cross-section SEM image of vertical Si nanowire arrays created using nanoimprint lithography and a wet etching process called metal assisted chemical etching (MACE). The MACE process exhibits virtually no lateral etch, and thus can etch extremely high aspect ratio structures, so high in fact, that the structures eventually collapse due to capillary forces in the etch solution [31].

Figure 3b shows a photograph of a 100 mm wafer of MACE nanowire arrays. The arrays exhibit a noticeable greenish color, although the color is somewhat “muddy”

compared to the colors exhibited by the hourglass and wine glass structures. This illustrates the profound effect the neck has in the hourglass shaped pillars. When the neck is absent, and the pillar is completely cylindrical, the spectral characteristics are completely different – instead of having a single pronounced resonant peak, the spectra are marked by many peaks and valleys. Two spectra are shown in Figure 3c for a couple of different simulated reflectance spectra for nanowire arrays with height of 1 μm and diameters of 100 and 105 nm. The spectra are similar to spectra exhibited by thin film interference implying that the arrays function as an effective medium. The subtle differences in the spectra illustrate a high level of sensitivity to the geometric properties of the wires, suggesting that hyperspectral imaging would be a highly effective tool for characterization of these silicon nanowires.

Wire Grid Polarizers

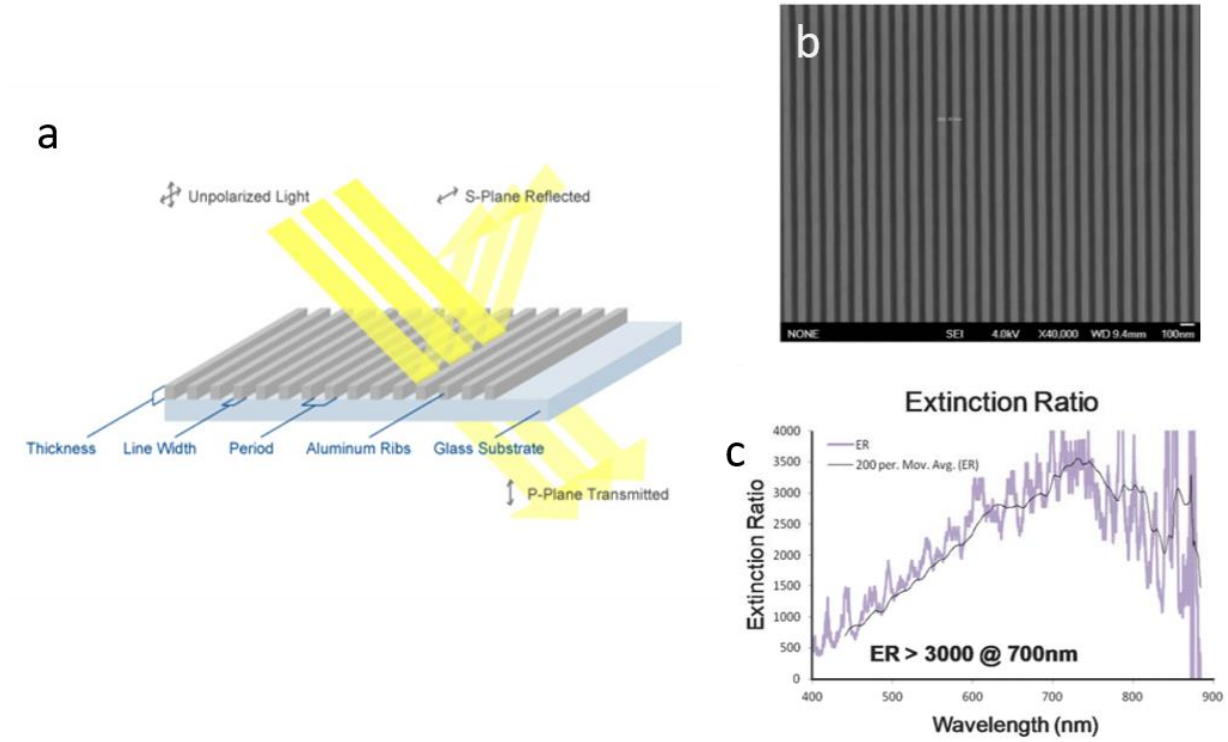

Figure 4. Wire grid polarizers. (a) Schematic of the operation of a WGP (image courtesy of MOXTEK[35]). (b) Top-down SEM image of a WGP (courtesy of Ahn et al [36]). (c) Extinction (a.k.a. contrast) ratio spectrum of a WGP (courtesy of Ahn et al [36]).

Wire-grid polarizers (WGPs) are an attractive polarization solution based on a 1D grating pattern of metallic nano-lines, typically having pitch on the order of twice the line width. The metallic line pattern acts as a polarization filter for linear polarization perpendicular to the direction of the lines (a.k.a. p-polarization). WGPs can be utilized in LCDs as back polarizing films which reflect the s-polarization rather than absorb it as typical film-based polarizers do, creating a "light recycling" effect which promises better power efficiency for the display. The polarization behavior is highly dependent on the geometry of the line/space pattern comprising the WGP.

Metal Mesh Grids

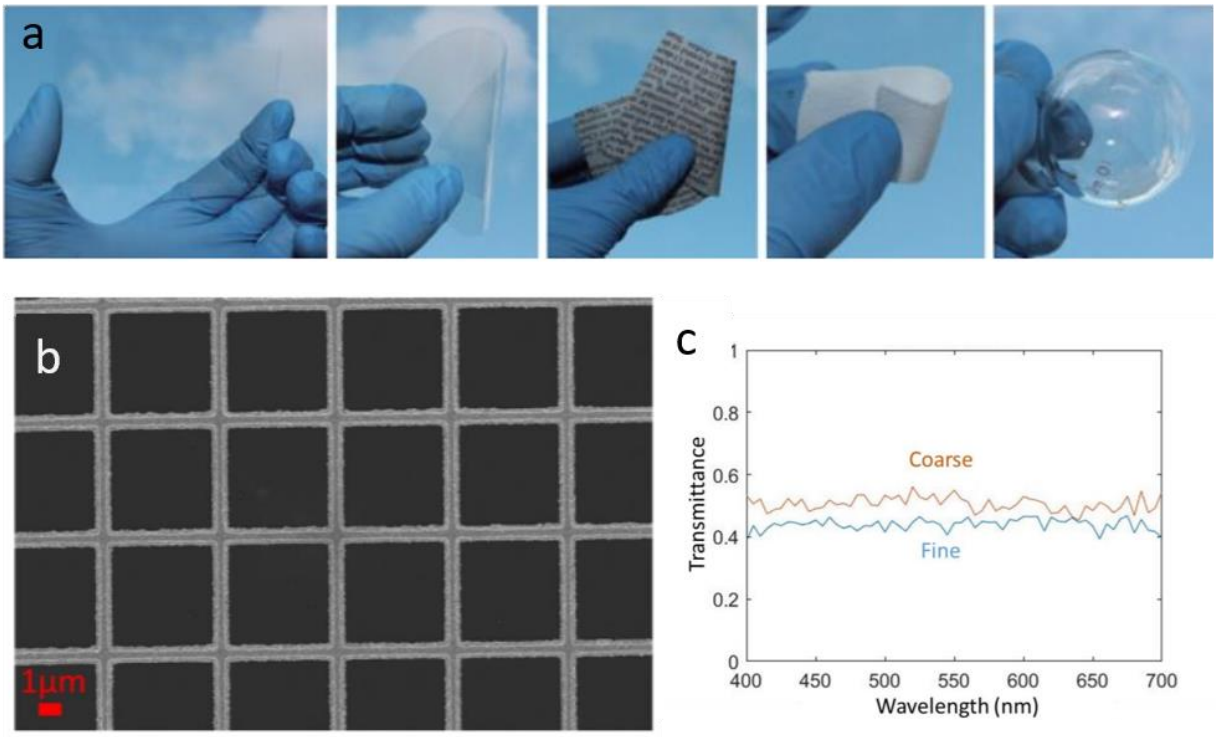

Figure 5. Metal mesh grids. (a) Photographs of metal mesh grids based on gold nanotrough networks fabricated on a variety of substrates including glass, PET plastic, paper, textile, and curved glass(left to right) (image courtesy of Wu et. al.[37]). (b) Imprinted Cu metal mesh grid [38]. (c) Transmittance spectra measured from an imprinted Cu metal mesh grid [38] for a coarse (500 nm linewidth, 5 µm pitch) and fine grid (300 nm linewidth, 3 µm pitch).

Metal mesh grids are an attractive candidate for replacing transparent conducting electrodes based on transparent conducting oxides like Indium Tin Oxide (ITO). ITO is brittle and also generally suffers from the increasing price of the element Indium which is technology critical material that is not abundantly available in nature [39]. Metal mesh grids are, as it sounds, grids of metallic nano-lines typically having µm-scale pitch. The contiguous nature of the mesh pattern allows for electrical conductivity while the majority

open area allows the film to be maintain optical transparency. The transparency of metal mesh grids depends strongly on the duty cycle and uniformity of the grid. In addition to the metrics of electrical conductivity and optical transparency, the haze – an optical scattering metric – of metal mesh grids is of high concern in displays.[1]

Chapter 2: Design of Spectral Imaging Systems

As discussed in Chapter 1, LNAs come in a variety of forms and produce a variety of different optical effects. Thus, spectral imaging systems will need to meet a range of specific characterization needs. LNAs can be reflective, like in the case of Si nanopillar arrays, or transmissive, like in the case of WGPs and MMGs. They may exhibit any number of nanophotonic effects such as polarization and coloration. They may be fabricated on wafers, sheets, or rolls depending on the application. Nonetheless, the general principle of spectral imaging remains the same: a measurement of either transmittance or reflectance needs to be made in a relevant wavelength range. Thus, the general architecture of spectral imaging systems remains consistent, with subtler variations being introduced based on the specifics of the exact LNA manufacturing scenario a system may be built for. In this section, we will discuss the general spectral imaging architecture, and for context we will show our current wafer scale spectral imaging system.

General Composition of Spectral Imaging Systems

All spectral imaging systems comprise 3 essential components:

Illumination Source(s):

One or more light sources are used to produce the light which will interact with the LNA device and then be measured. The light source(s) need to be chosen to have appropriate spectral characteristics, intensity, and form factor. Any number of different types of light sources may be used depending on what makes the most sense for the given

situation. Some examples of light sources include: Incandescent light sources, arc lamps, fluorescent lamps, LEDs (light emitting diode), and lasers.

Camera Sensor(s):

Every spectral imaging system will contain a camera sensor. Usually the camera sensor will exist inside a camera unit in which a lens is used to focus an image of the LNA onto the camera sensor. The camera sensors utilized in this work are intended for the visual spectrum of light, but camera sensors with ranges extending into the UV or the near-IR can of course be used where applicable. Also, cameras with spectral resolution can be used such as RGB cameras, multi-spectral cameras, and hyperspectral cameras. Camera form factor can be either areal or linescan. Linescan cameras are often a good choice for continuous roll-to-roll applications.

Various Other Optical Components:

Finally, in most systems there will be other optical components to guide and modulate the light as it travels from the light source, to the LNA device, and to the camera. Various optical components may be utilized to get a particular result including any of the following: polarizers, mirrors, beamsplitters, lenses, diffraction gratings, color filters, irises, slits, apertures, etc.

Figure 6 shows simple schematics of spectral imaging systems for both transmissive and reflective measurements utilizing a “single-beam” architecture. The scheme is quite simple. The light source projects light through the device (or reflects it off of the device for reflectance measurements) and the light is captured thereafter by the

camera. Note that in the reflective case, a beamsplitter is used to enable normal incidence measurements to be made.

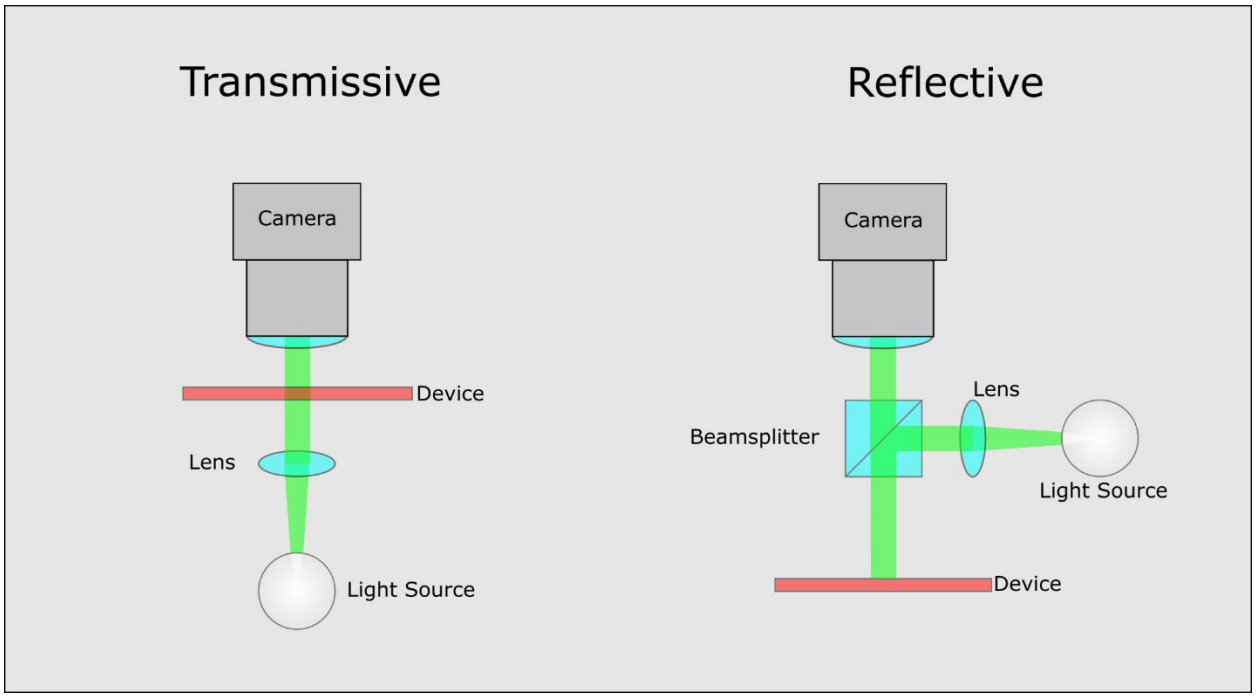

Figure 6. Schematic showing fundamental designs of single-beam spectral imaging systems for transmissive and reflective measurements.

The simplest spectral imaging systems are “single beam”. This term is derived directly from its use in traditional spectrophotometers in which a “single beam” instrument is one in which only the beam going through the sample is measured. In these systems, in order for ratiometric measurements like transmittance or reflectance to be made, the sample must be swapped with a reference object which has a well-known reflectance (like a high-quality mirror) so that the measurement is made relative to a known value. So-called “dual-beam” spectrophotometers also exist in which the beam is split into two parts and the sample and reference measurements are made simultaneously. Since it is a simultaneous

measurement, it accounts for variations in the source light intensity that can otherwise occur between the separate measurements of the sample and reference. The dual-beam architecture also saves time by eliminating the swapping event. The dual-beam architecture is achieved in spectral imaging systems by adding a second camera which images a split segment of the beam which has not interacted with the sample. This is shown in Figure 7.

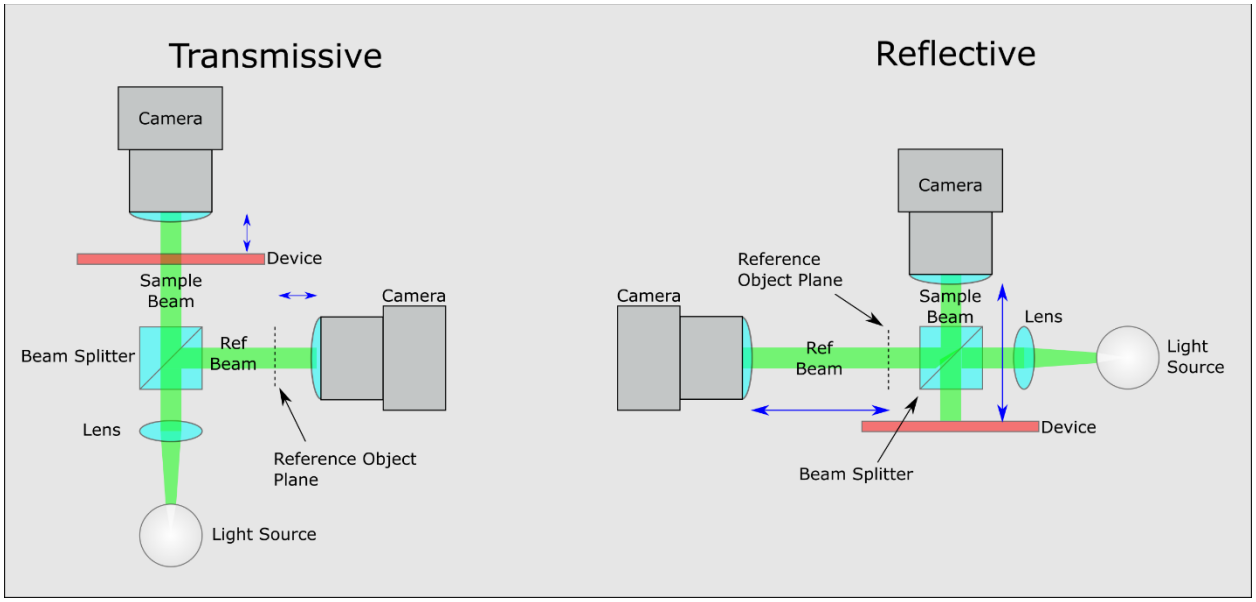

Figure 7. Schematic showing fundamental designs of dual-beam spectral imaging systems for transmissive and reflective measurements.

The following condition must be met in order for this to work: The total beam path lengths from the central point of the beamsplitter to each camera must be equal. This ensures that the camera measuring the reference beam (the reference camera) is focused on an imaginary plane (called the “reference object plane” in Figure 7) which is located at the same point along the reference beam as where the sample is placed along the sample beam. This path length is labeled by the blue double arrows in Figure 7. Thus, the reference camera is imaging the light source as it is projected onto the sample surface but having not

yet interacted with the sample. Thus, the ratio of the sample beam measurement to the reference beam measurement quantifies how much the sample is changing the beam in terms of transmittance or reflectance. Since the measurement is an image, the value is measured in every pixel in the resulting images. Care needs to be taken in aligning the two cameras such that the pixels in each camera are aligned to one another i.e. referencing the same point in space.

Our current wafer scale spectral imaging for reflective measurements is shown in Figure 8. For simplicity and cost, this system was just designed to be single-beam. The system uses a Tunable Light Source from Newport (model# TLS-300X) which runs light from a Xenon Arc Lamp through a monochromator producing a beam of light which is tunable to different spectral bands spanning the visible spectrum and beyond. The beam is collimated by an achromatic doublet lens and then split by a beamsplitter. One half of the beam is directed downwards towards reflective samples which rest on a flat stage. The beam is reflected from the sample, passes again through the beamsplitter, and enters a telecentric lens attached to a 5-megapixel monochromatic CMOS camera from Point Grey (now known as FLIR) (model# CM3-U3-50S5M). The system has a FOV of 19 x 23 mm with a pixel size on the sample of ~9.4 μm.

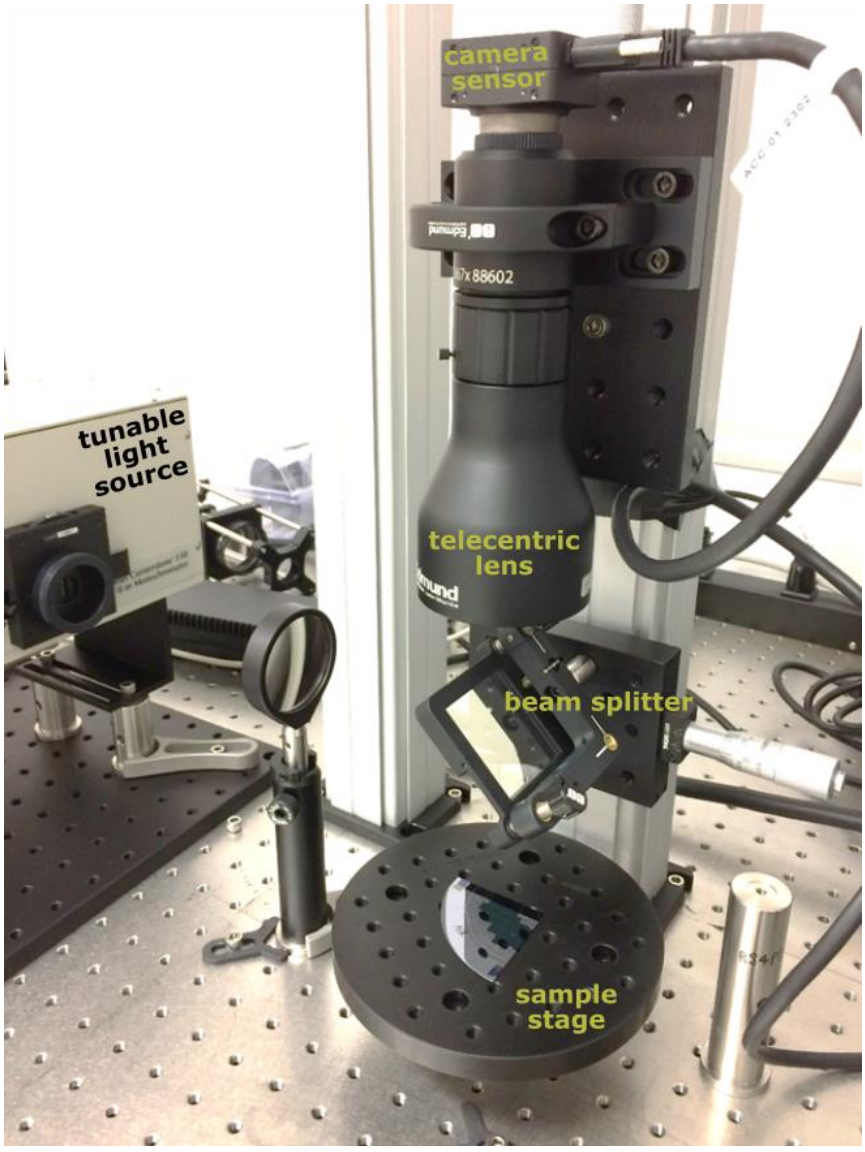

Figure 8. Our wafer scale spectral imaging system for reflective measurements.

The telecentric lens ensures that each pixel is receiving the same angular content from each part of the image. Otherwise, an imaging system using a conventional lens (known as entocentric) inherently receives different angles of rays depending on which part of the field of view is being considered. A good example of entocentric imaging is human vision. The angular content clearly varies dramatically from our central point of

vision to the peripherals. It is generally a good idea to avoid this situation in spectral imaging metrology applications, because it introduces a spatial-angular dependency into the measurement which may add considerable uncertainty to the measurement. Similarly, it is also ideal to use a telecentric illumination style, because angled rays from a light source which is simply collimated could be scattered into the acceptance cone of the telecentric imaging lens making it appear as if the un-scattered light had higher intensity than it actually did. Collimated light sources generally have considerably higher divergence angles than telecentric ones. These issues aren't completely alleviated by telecentric systems as there always exists some range of angles on both the illumination and imaging side, and thus some amount of scattering beyond 0^{th} order can occur, but use of telecentricity greatly reduces the problem especially when small numerical apertures are utilized. Nonetheless, it's possible that this effect can be accounted for, and it may be advantageous to do so, because entocentric imaging generally affords larger FOVs than telecentric imaging. Our wafer scale system uses telecentric imaging but does not use telecentric illumination.

Ideally, the illumination would be polarized to a high degree of purity so that light with well known polarization state and spectral properties interacts with the sample. In later chapters, particularly Chapter 5, we will discuss how computer simulations of LNA light interactions are used to predict geometry. The accuracy of these simulations depends on the similarity of the model to the real-world measurement, and factors like polarization ideally should be controlled. In this system, we do not usually control the polarization of the illumination, but most of the samples we have studied are not polarization sensitive,

and thus the polarization state of the illumination should not matter in these cases. In a case such as a wire-grid polarizer (WGP) measurement, the polarization of the illumination is highly important and needs to be controlled.

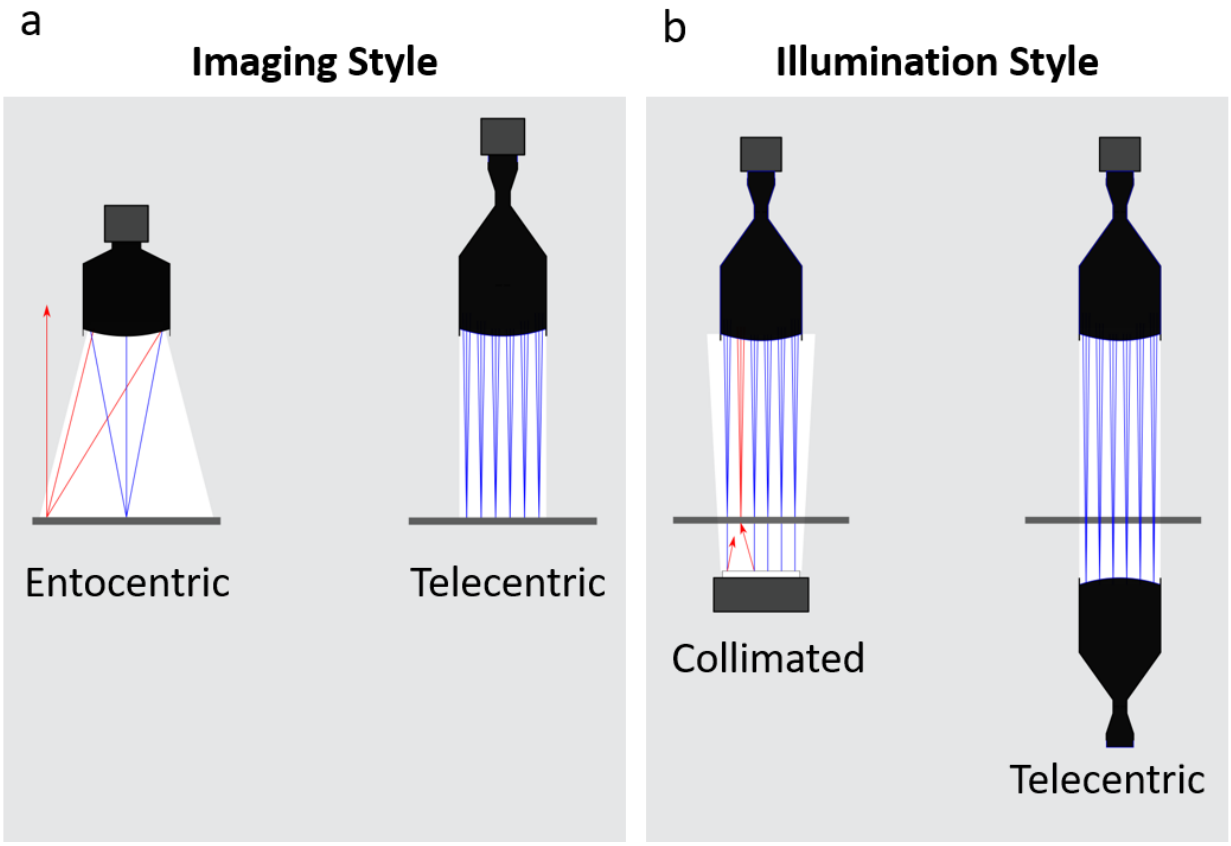

Figure 9. (a) An illustration that shows the effect of using entocentric imaging vs telecentric imaging. (b) An illustration that shows the effect of using a collimated light source vs a telecentric light source for a transmittance measurement. The same concept applies for reflectance measurements.

The system of Figure 8 allows for either hyper- or multi-spectral imaging depending on the choice of spectral bands used for a characterization. Most of our measurements make use of the hyperspectral capability, recording spectral reflectance images from 400 to 700 nm in steps of 5 nm. The bandwidth of the system (the spectral

width of the light beam outputted by the tunable light source) is adjustable down to 0.6 nm, although typically it is set to 8 nm. Note that the bandwidth (8 nm) and spectral step size (5 nm) are independent metrics.

The system has primarily been used for reflectance measurements but can be rearranged to perform transmittance measurements by placing the camera on the opposite side of the sample from the illumination source.

DESIGN CONSIDERATIONS

Care should be taken in order to design the spectral imaging system according to the needs of the LNA device(s) that it will be responsible for characterizing. As mentioned, LNA devices can be either transmissive or reflective and the spectral imaging system will have to be designed accordingly. Note that it is possible for a single spectral imaging system to measure both transmitted and reflected light simultaneously, if need be, by assigning multiple cameras to different beam paths.

Furthermore, the specific functionality of the device must be considered. WGPs for instance will need to be characterized in terms of polarization, and thus it will be necessary to have control over the polarization of the light in the system. This is achieved by using polarizers in the spectral imaging system. Structural colors, on the other hand, will need some sort of color- or wavelength-dependent characterization thus dictating the type of illumination source or the spectral resolution capabilities of the camera (i.e. RGB color or multi-spectral).

The manufacturing scheme must also be considered. Devices can be manufactured in a variety of ways, namely on wafers, rectangular glass panels/sheets, disks, or roll-to-roll substrates. The difference in these manufacturing schemes impacts the spectral imaging architecture significantly. Whereas the discrete stop-and-start motion of wafer manufacturing is well-suited to traditional area type cameras, roll-to-roll systems and panel/sheet systems are generally better handled by linescan cameras which are designed to image objects undergoing continuous single-axis translation. Our current spectral imaging system is designed for wafer-scale and thus uses an area camera.

The spatial resolution and field of view (FOV) of the system also need to be considered. Each LNA will need to be characterized on specific length scales depending on their applications. LNAs for displays like WGPs and MMGs, for instance, may need to be characterized at a spatial resolution comparable to that of the resolution of the displays they are intended for to make sure that these LNAs won't negatively impact individual display pixels. Individual defects may actually be much smaller than the spatial resolution of the spectral imaging, but as long as their cumulative effect is significant enough to affect the minimum area of interest (such as a display pixel sized area) the defect will at least be detected by the spectral imaging system. This minimum area of interest is what we refer to as the minimum "object space pixel size" (OSPS). The minimum OSPS is a key parameter which needs to be chosen based on these requirements. A camera and lens need to be selected which achieves the minimum OSPS, ideally with as large a field of view (FOV) as possible. It may be advantageous or necessary in certain situations to use multiple spectral imaging systems with different FOVs and resolutions to perform hierarchical-type

metrology in which thse multiple systems are responsible for characterization at different length scales.

PROCESSING OF SPECTRAL IMAGING DATA

Once the system is assembled and collecting data, the raw data produced by the system must be processed in order to be used effectively. Every dataset starts with two different images, one of the sample beam and one of the reference beam. The sample and reference images must be combined to calculate the ratiometric value of transmittance or reflectance, but first many factors must be taken into account to transform the raw image data from the cameras into representative data. Camera parameters like gain and exposure time, and various common noise sources must be factored in to get accurate results. The raw images from a given camera in a spectral imaging system undergo the following calculation to calculate an image of the actual intensity seen by the system. The way this intensity image (I) is calculated is shown in Equation 1.

Equation 1. Intensity image.

$$I = (DN - Noise_{read} - Noise_{dark}) * \frac{10^{Gain/10}}{t_{exp}} - I_{background}$$

Where the variables are defined as follows:

Table 1. Variables used in Equation 1.

I	Intensity
DN	Stands for digital number (a pixel value in the image) which, for 8-bt images, ranges from 0 to 255.
$Noise_{read}$	The read noise of the camera
$Noise_{dark}$	The dark noise of the camera
$I_{background}$	The background light intensity in the room as measured by the camera during a long exposure
Gain	Camera gain, in decibels (dB)
t_{exp}	Camera exposure time

Equation 2. Calculation of transmittance (or reflectance) images.

$$T\ (or\ R) = {I_{sample}}/{I_{reference}}$$

…where T is transmittance and R is reflectance.

The result is a set of images (one for each waveband) containing either reflectance or transmittance values like what is shown in Figure 10. In the case of hyperspectral imaging, the dataset is commonly referred to as a hyperspectral "cube", having three dimensions: the two spatial dimensions X and Y, as well as the wavelength dimension. Unlike with conventional images, each spatial point in the hyperspectral cube (x,y) contains an entire spectrum.

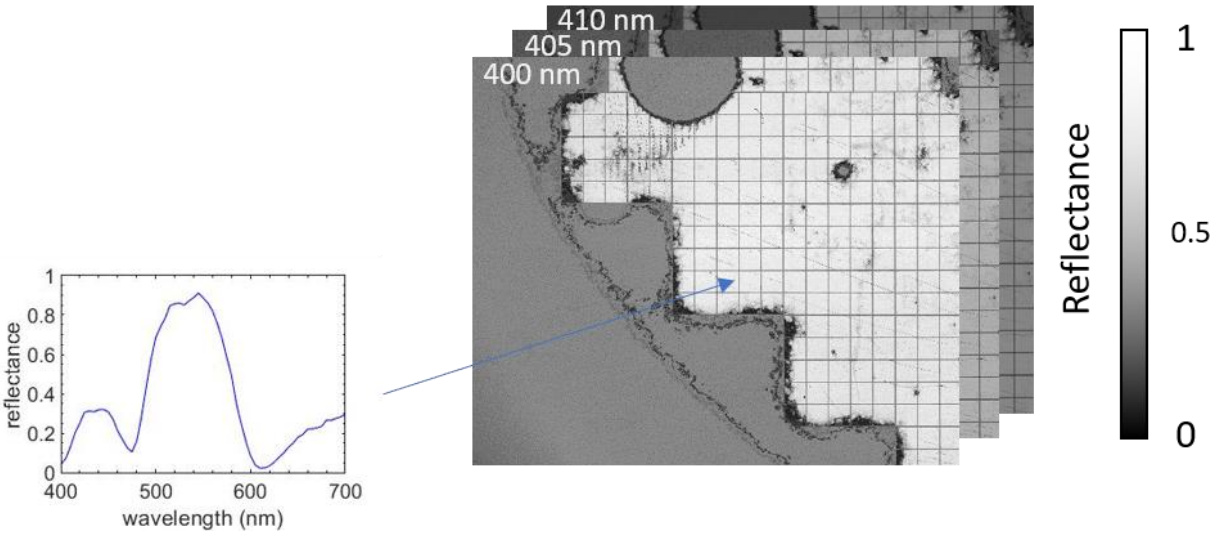

Figure 10. Spectral Imaging Data.

Our current system is primarily designed for hyperspectral imaging, but RGB color imaging can be a very effective form of spectral imaging for certain LNA manufacturing scenarios as well. As we discussed before, the colors exhibited by LNAs can provide a great deal of information and these are well-captured by RGB imaging. RGB imaging is inherently much faster than hyperspectral imaging, so when it can be effective it should be utilized. RGB imaging can be done with RGB cameras, but hyperspectral data can also be transformed into RGB according to the CIE standard [40]. First, the spectral reflectance is converted to the CIE tristimulus X, Y, Z values as follows:

Equation 3. Transformation from reflectance data to tristimulus values.

$$\mathrm{X} = \frac{1}{N}\sum_{\lambda=400}^{\lambda=700} R(\lambda) * CIE_x(\lambda)$$
$$\mathrm{Y} = \frac{1}{N}\sum_{\lambda=400}^{\lambda=700} R(\lambda) * CIE_y(\lambda)$$
$$\mathrm{Z} = \frac{1}{N}\sum_{\lambda=400}^{\lambda=700} R(\lambda) * CIE_z(\lambda)$$
$$\textit{...where } \mathrm{N} = \sum_{\lambda=400}^{\lambda=700} CIE_y(\lambda)$$

The tristimulus values CIE_x, CIE_y, and CIE_z are commonly available tabulated values corresponding to the x,y,z curves shown in Figure 11(b). The color matching functions we used were from the "CIE 1931 2-deg XYZ" color matching functions [41]. Next the tristimulus values are converted to RGB with the following common transformation:

Equation 4. Transformation between tristimulus and RGB values [42].

$$\begin{bmatrix} R \\ G \\ B \end{bmatrix} = \begin{bmatrix} 3.063 & 1.393 & -0.476 \\ -0.969 & 1.876 & 0.042 \\ 0.068 & 0.229 & 1.069 \end{bmatrix} * \begin{bmatrix} X \\ Y \\ Z \end{bmatrix}$$

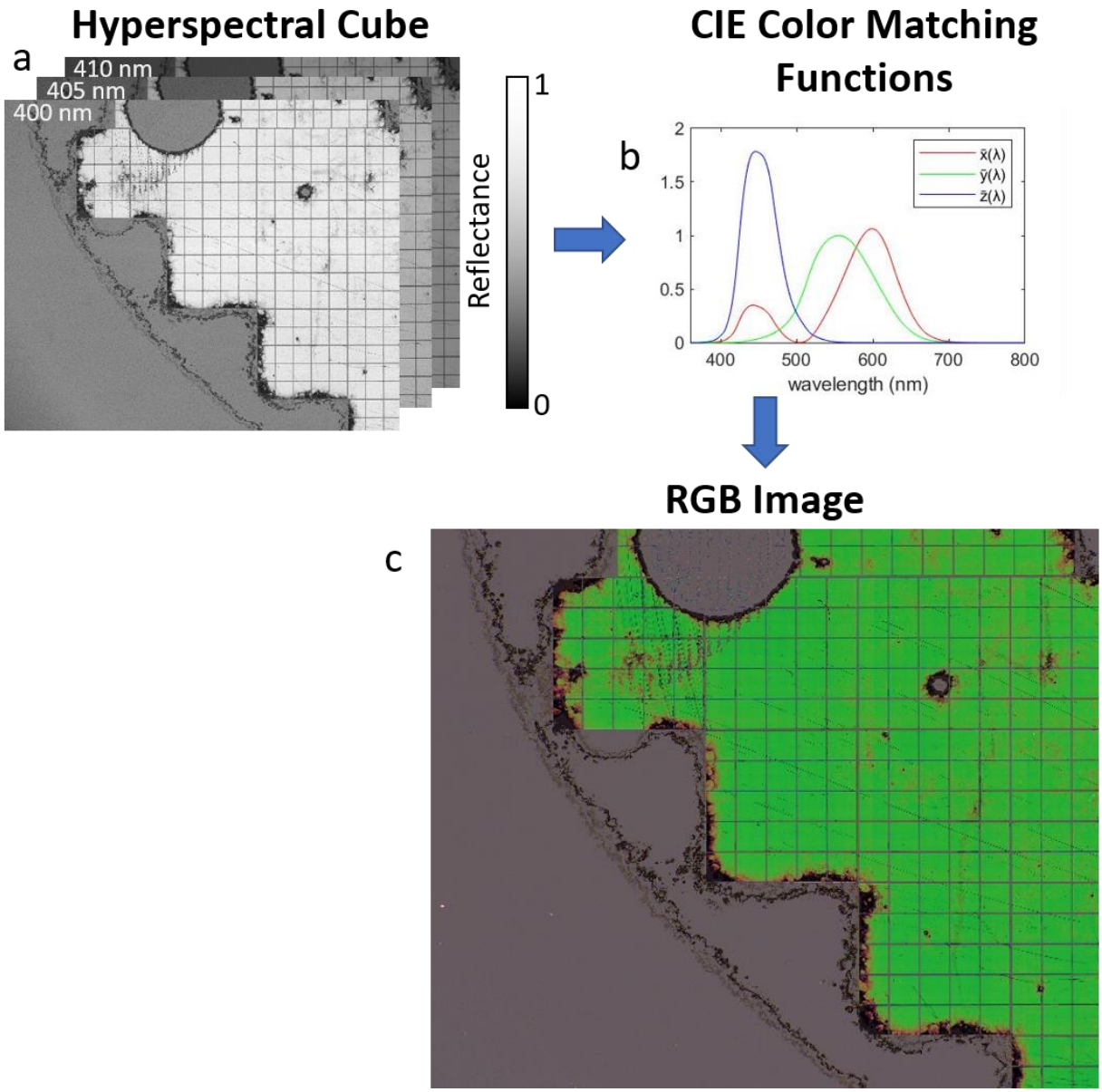

Figure 11. Conversion of hyperspectral cube to RGB image. (a) visual representation of a hyperspectral cube. The specific dataset is for arrays of wine glass shaped nanopillars with roughly 130 nm diameter and 200 nm pitch. (b) line plot of CIE color matching functions. (c) RGB image of the sample.

Multiple measurements can be taken and stitched together in order to take information over areas larger than the FOV of one camera like what is shown in Figure 12.

For 100 mm wafers, we have succeeded in stitching full wafer images from 12 individual fields (see Figure 12) using SURF feature-based stitching [43]. The stitching is generally calculated based on the RGB images or images corresponding to one of the spectral bands from the hyperspectral cube and the calculated transformation is applied to all the hyperspectral frames. The individual hyperspectral frames can then be assembled to form the hyperspectral cube for the full wafer. This approach naturally requires some spatial overlap between the individual frames, making it inherently somewhat inefficient. Precision wafer handling would offer a better solution for multiple field imaging which would essentially eliminate the need for stitching.

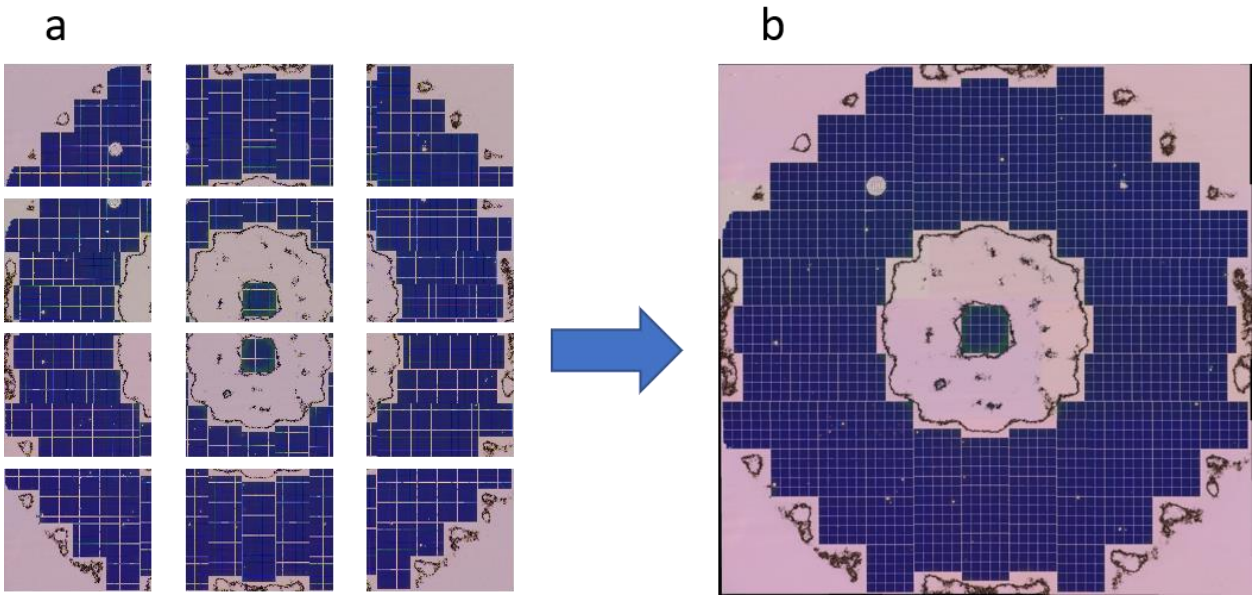

Figure 12. Image stitching. (a) collection of individual field RGB images. (b) stitched RGB image of full 100 mm wafer containing truncated cone arrays.

MANUFACTURING THROUGHPUT

Finally, let us consider the throughput of a spectral imaging system. Depending on the manufacturing scenario, anywhere from a small percentage to as much as 100% of the total device area may need to be inspected at a speed fast enough to keep pace with the manufacturing line or else it will bottleneck the entire factory. The throughput of a spectral imaging system can be calculated based on careful consideration of all the factors contributing to the time it takes to make measurement including things like camera exposure time, wavelength switching time, time spent moving between different fields, etc. Wafer throughput can be calculated according to the following equations:

First, the imaging time is calculated. This is the time it takes to acquire one image at one wavelength.

Equation 5. Imaging time.

$$t_{img} = t_{exp} + t_{read}$$

Next, the field time is calculated based on the result for imaging time and the fact that multiple spectral bands must be imaged. This also includes the time it takes for the monochromator to switch between each spectral band.

Equation 6. Field time.

$$t_{field} = [N_{\lambda} * t_{img}] \; + \; [(N_{\lambda} - 1) * t_{move\_\lambda}]$$

Then we calculate the wafer time, or the time it takes to measure a full wafer (all spectral bands at all fields). This includes the total field time for all fields as well as time spent moving between the individual fields.

Equation 7. Wafer time.

$$t_{wfr} = [N_{fields} * t_{field}] + [(N_{fields} - 1) * t_{move\_field}]$$

Finally, we calculate the areal throughput (generally in m^2/hr).

Equation 8. Areal Throughput.

$$Thru = {A_{wfr}}/{t_{wfr}}$$

The variables used in these equations are defined in Table 2. The table also includes typical values based on our current spectral imaging system as well as typical values which could be expected from an optimized system. The primary difference between the current and optimized systems would be reduction in the wavelength switching and field moving times. The wavelength switching time can essentially be reduced to 0 seconds if the diffraction grating in the monochromator spins continuously and the spectral bands are synchronously "windowed" by the camera exposure. This may require use of a camera with shorter read times to be effective, but high-speed cameras are available with framerates of 1000 fps (1 ms read time), for instance. Also, the field movement time can be reduced significantly as well with use of a more sophisticated wafer handling system. Our current system actually doesn't have any wafer handling capability at all, and the field switching is done by hand. We choose to place the current value at 5 seconds in anticipation of installing an XY stage for wafer handling in the near future. Much faster wafer handling capabilities exist which can move and settle in 100 ms.

Table 2. Variables used in throughput equations.

Term	Description	Current Value	Optimized Value
t_{exp}	Exposure time of camera	10 ms	10 ms
t_{read}	Readout time of camera	33 ms	1 ms
N_{λ}	Number of wavelengths for characterization	61	61
t_{move_λ}	Wavelength switching time	2 s	0 s
N_{fields}	Number of fields needed to cover a wafer	18 (100 mm wafer)	18 (100 mm wafer)
t_{move_field}	field switching time	5 s	0.1 s
A_{wfr}	Area of wafer	7853.98 mm^2* *(100 mm wafer)	7853.98 mm^2* *(100 mm wafer)
$Thru$	Throughput	See Figure 13	See Figure 13

When the typical values from Table 2 are placed into the equations we get the throughput curves shown in Figure 13. These curves show how the throughput changes as a function of the number of spectral bands required for the measurement. The curves are plotted for the current and optimized systems. The point at which the number of spectral bands equals 61 is highlighted by the vertical black dotted line which corresponds to the number of spectral bands needed to form a spectral image from 400-700 nm in steps of 5 nm.

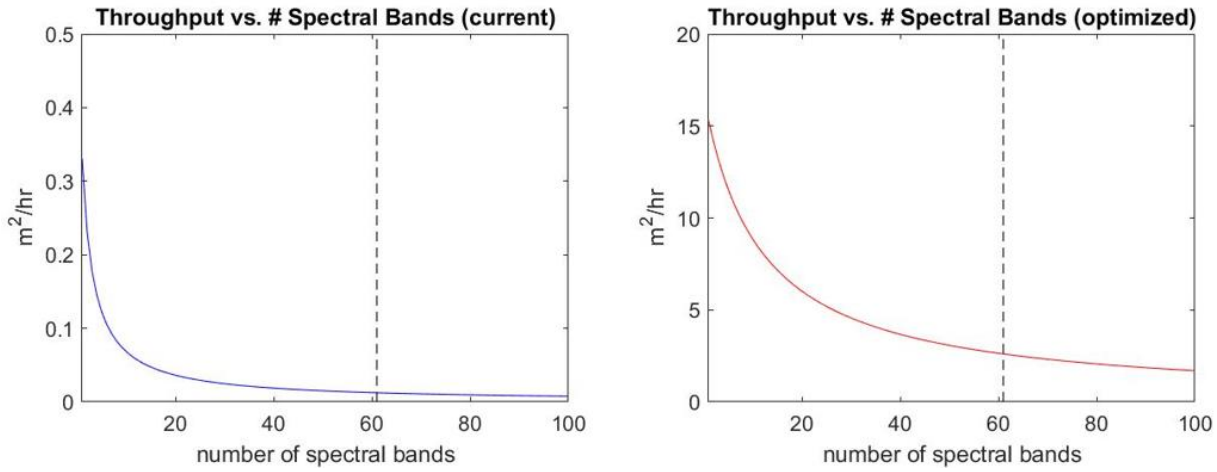

Figure 13. Line plot of throughput of spectral imaging systems for current (left) and optimized (right) systems. Note that both sets of values depend on various design parameters of our current wafer scale system.

Our current system has relatively low throughput of around 0.01 m^2/hr. This is mainly due the slow mechanical aspects of the system. When these aspects are optimized, throughput can increase to around 2.6 m^2/hr with 61 spectral bands. Note that both sets of values depend on various design parameters of our current wafer scale system. Of course, this wavelength range and step size can be adjusted depending on the requirements of the particular manufacturing scenario. If the measurement can be done with a single acquisition, as would be the case with a monochromatic measurement, broadband measurement, or RGB measurement, the throughput will be around 15.3 m^2/hr. In reality, it would probably be significantly improved due to the inherently higher light throughput when white light or wide color bands (as is the case with RGB) are measured, however the read time would probably limit the total imaging time to 1 ms, even if the exposure times were significantly less than that. Regardless, for this reason, it's highly recommended that such systems be used when they are applicable. In particular, RGB systems are a superb

choice, because they enable acquisition of 3 spectral bands in a single acquisition, at least in the case when a Beyer type sensor is used. This throughput analysis has been done considering 100% areal coverage. If sampling is introduced, the measurement time can be reduced significantly. Of course, sampling can only be justified when manufacturing reliability is high as is the case with mature processes.

Finally, it should be mentioned that the throughput calculations are for a system involving just one camera. Systems are, of course, open to parallelization using multiple cameras or even multiple separate systems.

Chapter 3: Overview of LNA Manufacturing Processes and Root-Causes of Common Defects

Before delving deeper into the application of spectral imaging metrology, it is important for us to take a step back and understand the manufacturing processes that are being used in this research to create LNAs. This is pre-requisite knowledge – a strong understanding of the fabrication processes must be established if we are to understand how and where different types of defects originate. In fact, there are many individual process steps involved in the fabrication of an LNA, each of which can fall victim to a handful of unique defect modes which can compromise device performance. In this section, we will briefly explain the general manufacturing processes used in LNA manufacturing, particularly in the context of nanoimprint lithography, and then delve into the common defect modes that can occur in each of these process steps.

MANUFACTURING PROCESS FLOW USED IN THIS WORK

In this work, the first step in a nanomanufacturing process flow is the lithographic step in which the features are defined in a masking material, typically a photo-curable resist on top of a substrate (i.e. Si or glass) or a previously deposited thin functional film (such as a semiconductor, metal or a dielectric) on a substrate. Once lithography is done, the pattern is then transferred to another material typically using an etching step. In some cases, the etch step may reveal an underlying material that can be used as a seed layer for selective growth *via* atomic layer deposition, electroplating, etc.

For the most part, this work deals with structures that have been made using Jet and Flash Imprint Lithography (JFIL) [1] and etching, especially for nanopillar/nanowire arrays,

although WGPs and MMGs can have very different post-imprint process steps including glancing angle metal deposition, electrochemical metal growth, or lift-off. Every process step has its own unique failure modes, and these must be well understood. For now, we will primarily focus on the imprint-etch process flow, a prime example for LNA manufacturing.

The JFIL process is detailed schematically in the top half of Figure 14. The process begins with the dispensing of a monomer fluid onto the substrate from an array of inkjets. The drop pattern can be programmed to dispense fluid "on-demand" so that varying pattern density in the template can be accounted for. Once the monomer is jetted onto the substrate, a fused silica template containing the pattern is brought into contact with the substrate causing the drops to spread and merge *via* capillary forces, filling up the template features. Some time is given for the spreading to occur, and then UV light is shined through the template causing the monomer to cure into a solid polymer. At this point the template is removed from the substrate, a process called "separation", leaving behind the cured polymer on the substrate with the pattern imposed by the template.

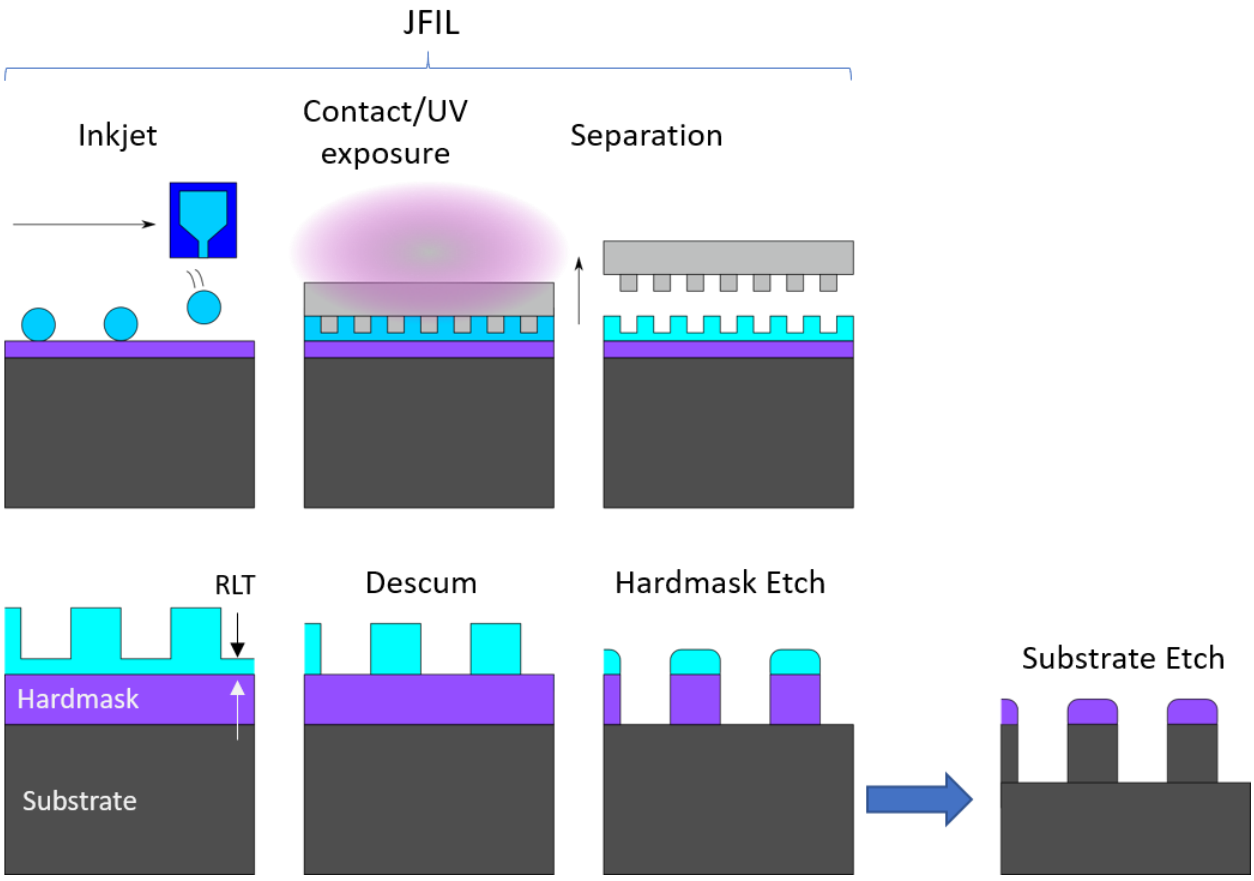

Figure 14. Exemplar nanoscale manufacturing process flow enabled by JFIL.

Once the imprint has been done, a thin layer of the cured resist, called the residual layer thickness or "RLT", remains between the features and must be removed to expose the underlying materials. This is done with an O_2/Ar plasma etch, called a "descum" etch. The descum step is highly critical, because under-etching the RLT causes subsequent etch steps to be delayed, and over-etching the RLT causes feature shrinkage. Furthermore, as we will see, variations in the RLT thickness can cause CD variations.

Oftentimes, a hardmask material such as SiO_2 is used as the actual etch mask, in which case the imprint pattern is first transferred into the hardmask before the substrate is

etched. This is not always necessary, although hardmasks generally allow for deeper etching of the substrate as well as other utilities such as lift-off. Either way, the imprint pattern is eventually transferred to the substrate material with an etch process.

IMPRINT DEFECT MODES

There are many ways that the imprint process can malfunction and create a defect in the imprinted pattern. In the inkjetting step for instance, inkjets can misfire, jetted drop volumes can vary, and drops can be misplaced spatially. In the contact step, particle contamination can get between the template and substrate causing large patterning voids. Similarly, voids can occur due to incomplete filling of features during spreading. During separation, adhesion failure can occur causing the resist mask to pull-off from the substrate and be dislodged in the template. Each of these failure modes creates a unique type of defect in the pattern which manifests in the final LNA device in a variety of ways. Let's examine a few of the most common defect modes:

RLT Variation

Usually after the imprint is done, the descum is performed to remove the RLT, exposing the underlying substrate. Variations in the RLT can occur due to drop dispense variations or incomplete drop spreading. Naturally, the descum etch must be timed for the thickest RLT so that breakthrough occurs everywhere, but the variation means that areas with thinner RLT will breakthrough earlier in the descum process, and when this occurs, a small but significant lateral etch component of the descum process attacks the bottom of the feature, shrinking the critical dimension (CD) of the pattern locally, creating CD

variations as shown in Figure 15. Oftentimes, this occurs due to incomplete drop spreading in which thicker RLT is created at the initial location of the drops which causes the drop pattern signature to appear in the final device. It can also occur in cases where the template has various abrupt pattern density variations and drop volume resolution of the inkjet is not enough to address these variations.

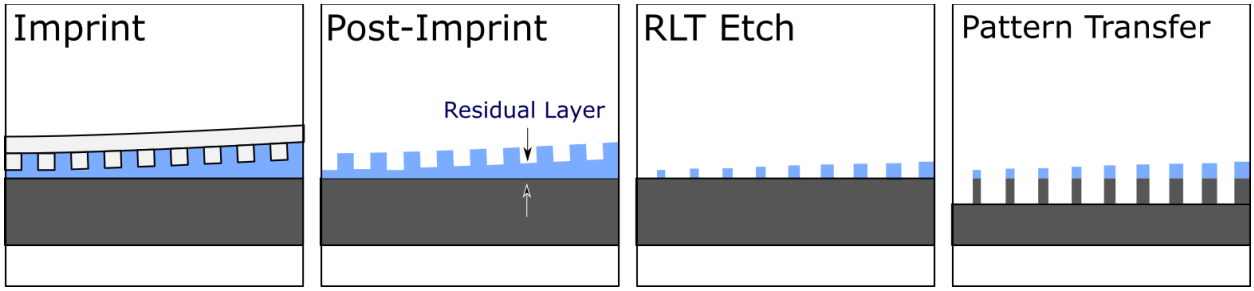

Figure 15. Schematic showing the cause and manifestation of RLT variations in a typical imprint-etch process flow for an LNA.

Figure 16 shows two examples of RLT variation due to incomplete drop spreading. Figure 16(a) shows the contrast ratio at 550 nm of a WGP in which a periodic signature runs top-to-bottom. In this case, variations in the contrast ratio exist with the same spatial arrangement of the drop pattern used during imprinting which had considerably higher periodicity in the x-direction. The likeness of the signature suggests that RLT variations existed due to incomplete drop spreading and caused linewidth variations in the final WGP device which manifests optically as variations in the contrast ratio. Figure 16(b) shows the signature of a drop pattern in a MACE-etched sample of short nanowire arrays. The incomplete drop spreading created a corresponding variation in the diameter of the pillars which is clearly visible in the RGB image of the sample as variations in the brightness of

the purple color exhibited by the sample. The periodicity of the signature has different pitch in the x- and y- directions because an anisotropic drop pattern was used.

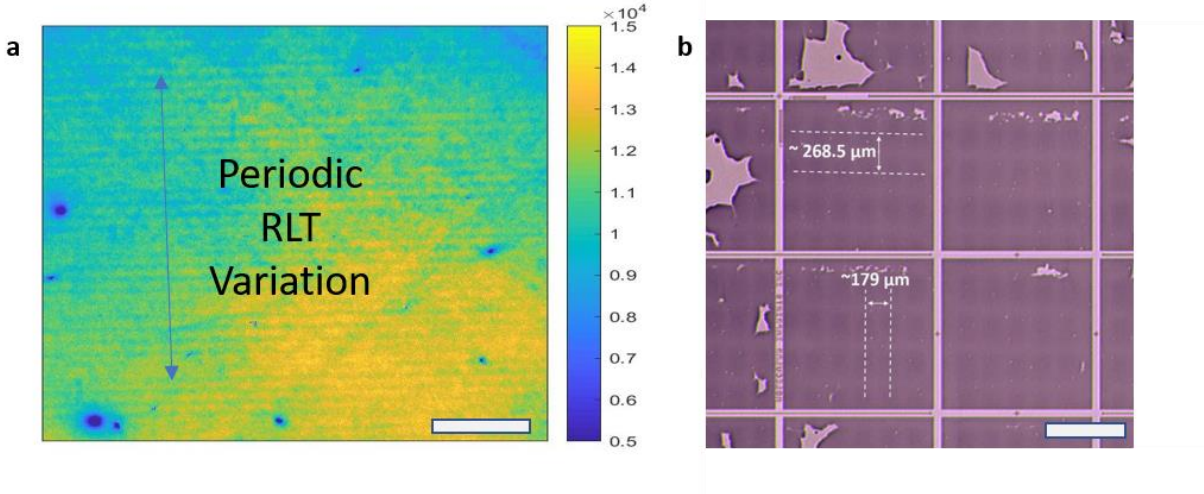

Figure 16. Examples of periodic RLT variations resulting from incomplete drop spreading during imprint. (a) A contrast ratio map at wavelength=550 nm for a WGP sample (scale bar = 5 mm). In addition to many other defects (most of them appear as blue dots), there is a noticeable periodic variation in the contrast ratio running top to bottom in the image. (b) RGB image of a sample containing short nanowires etched with MACE (scale bar = 0.5 mm). The periodic variation in the brightness of the purple color exhibited by the arrays is due to incomplete drop spreading RLT variations causing the nanowire diameter to vary accordingly. The measured x and y period of the signature as shown matches that of the drop pattern used during imprinting of this wafer. It should be noted that the light pink colored regions including the streets between the square patterned areas and the irregular closed regions are voids which do not include the imprint resist.

Particle Contamination

The nanoimprint process results shown here are from an automated commercial tool, the Imprio 1100. This tool processes wafers in a clean chamber rated at better than Class 1, and the tool is placed in a Class 100 cleanroom. Even though this is the case, extra care still must be taken to avoid getting particles on the wafer or the template during

imprint. For example, any manual handling of the wafers or templates prior to their introduction into the Imprio 1100, leads to particles during the imprint process. When this happens, particles get squeezed between the template and the wafer preventing the pattern from forming in the area surrounding the particle, as schematically illustrated in Figure 17a. The result is a large, un-patterned void on the wafer which exposes the underlying substrate. An example of a particle void on a wafer containing the hourglass-shaped vertical Si nanopillar arrays is shown in Figure 17b. Owing to the fact that the template is fairly rigid, the resulting exclusion zone caused by a particle can be on the order of one thousand times the size of the particle itself [44], so the particle that caused this specific void was probably on the order of 3 μm in size. As seen in Figure 17, particle voids are often surrounded by a circumferential region where the pattern gradually transitions back in. The SEM image in Figure 17c shows the edge of the same defect shown in Figure 17b and how the transition zone contains both patterned areas and bare Si. In this particular case, the partially patterned zone contains short, stubby nanopillar arrays exhibiting either high absorption and/or light scattering properties, causing it to appear dark as seen in the dark circle in Figure 17.

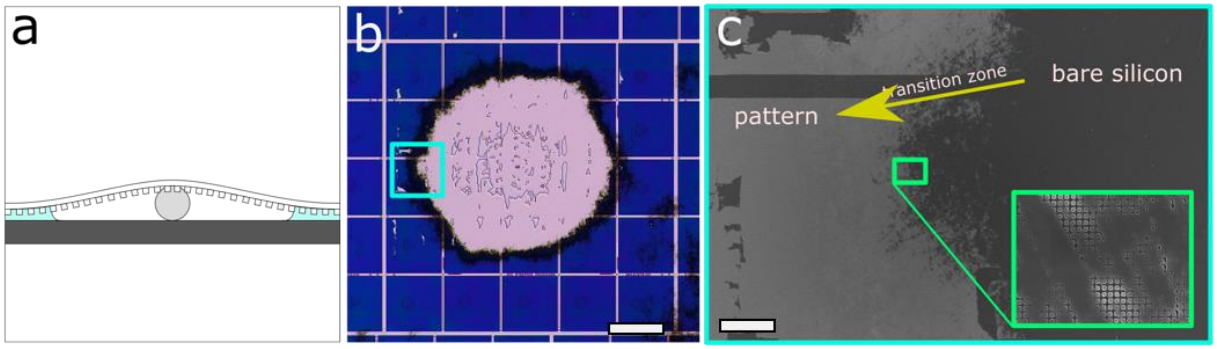

Figure 17. Imprint particle contamination. (a) schematic showing the effect of the particle event on the nanoimprint process. (b) cropped portion of the RGB image of a blue hourglass pillars sample showing the result of an imprint particle (scale bar = 1 mm). (c) Top-down SEM image of the boxed region in (b) (scale bar = 50 µm). The edge of the particle exclusion zone contains a transition region which goes from bare Si to the normal pattern.

Non-Filling

Another common defect mode is the creation of small voids caused by non-filling during the imprint process. Occasionally, bubbles of gas can get trapped inside the monomer fluid used to form the imprinted features or fluid can simply fail to spread to certain areas of the template leaving a region of the wafer un-patterned as schematically illustrated in Figure 18a. These bubbles sometimes disappear if the spread time in the imprint process is increased. In cases where the bubbles are stable over time, it may be due to a hydrophobic surface contamination on the wafer that causes a dewetted region. Although this type of defect is a void, it differs greatly from the voids caused by particles both in terms of its size and shape characteristics. Imprint non-fill voids are generally much smaller than particle voids, typically ranging from 10's to 100's of µm. Their shape is variable, but unlike the particle voids the edges are always well-defined and sharp as seen in Figure 18(b,c). The sharp edges are the result of the liquid "pinning" behavior during

imprint. The fluid mechanics of the monomer basically dictates that the fluid either fills a feature on the template or doesn't, and so the edge of the defect is an abrupt transition between patterned and un-patterned area which happens over a single period of the pattern itself. In the case of the hourglass-shaped nanopillars, the period is just 200 nm, so relative to the defect size the edge transition is basically instantaneous.

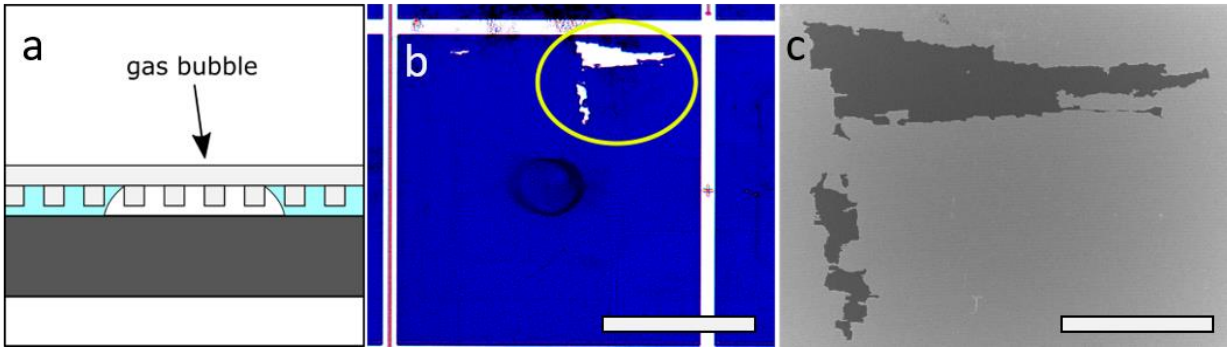

Figure 18. Imprint non-filling error. (a) schematic showing the process of non-fill. (b) cropped portion of a 3X magnification RGB image of the blue sample showing multiple non-fill defects (scale bar = 0.5 mm). The brightness/contrast of the image is increased for better visualization. (c) top-down SEM image of the non-fill defect shown in (b) (scale bar = 100 µm).

Adhesion Failure

Yet another imprint-related defect mode creates a "patchy" region containing a mixed region of patterned and un-patterned locations, like the one shown in Figure 19c. The exact root-cause of this defect mode is not fully understood and may include multiple distinct causes, although appears to be different from the imprint non-fill because of its unique morphology and the fact that it generally happens on smaller length scales (1-10's of µm). We think that this defect may be caused by the pattern being partially pulled off at the moment when the template separates from the wafer at the end of the UV exposure, and here these defects are referred to as "adhesion failure" defects. Exactly why this occurs

is not fully understood, but it may have to do with failure of the pattern's adhesion to the wafer, small gas bubbles, or some combination of the two. In the case of these adhesion failure defects, prior literature indicates that the template gets temporarily contaminated with the resist and the subsequent few imprint defects show signs of this contamination (see Figures 4 and 5 in Bailey et al. [45]). Overall, this defect is common, and its manifestation is distinct relative to defects discussed above that are caused by RLT variation, particles, or non-filling voids. Optically, this adhesion failure defect creates an area with a spectrum and color which is some combination of the signature from the normal array and that of the underlying bare substrate.

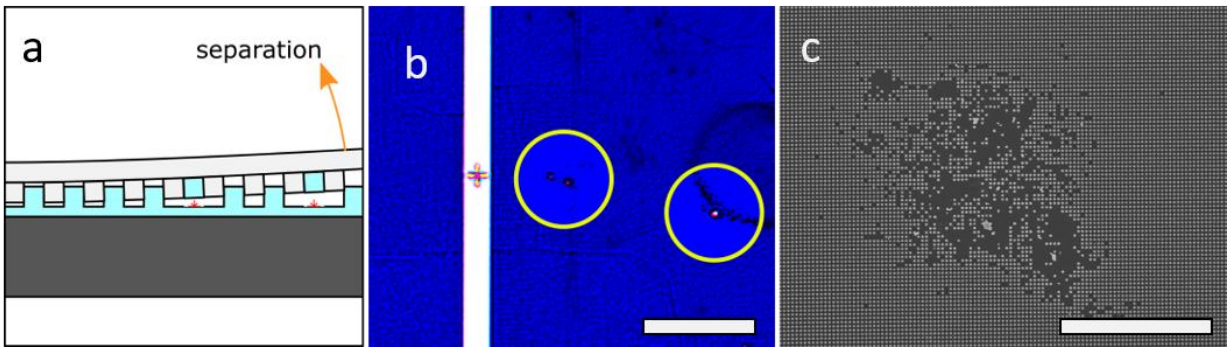

Figure 19. Adhesion failure error. (a) schematic showing the process of adhesion failure. (b) cropped portion of a 3X magnification RGB image of the blue sample showing multiple adhesion failure defects (scale bar = 100 µm). The brightness/contrast has been adjusted in the circled areas to help visually reveal the defects. They are typically very small (~10-30 um across) and difficult to see even with the high magnification measurement. (c) SEM image of a adhesion failure defect (scale bar = 10 µm).

IMPRINT TEMPLATE DEFECTS

Sometimes defects exist on the templates used for imprint that lead to what are known in the lithography literature as repeating defects or repeaters. These repeaters can either be temporary, i.e. when something is on the template that can be removed (like a

particle or the result of an adhesion failure as discussed above), or permanent if the defect is actually part of the template, i.e. a scratch or a damage, missing features, CD variations, etc. Defects that are part of the template are guaranteed to create defects in the devices every single time, whereas temporary template defects may clear up with cleaning or just through repeated use [45].

One such permanent template defect is shown in Figure 20. In this green hourglass array sample, a regular pattern of squares can be seen which are smaller than the larger 1x1 mm squares that comprise the pattern. The smaller squares are approximately 300 x 300 µm. Interestingly, this pattern is not readily visible when the data is viewed in RGB in Figure 20a. Only when individual hyperspectral frames are viewed does the pattern become evident. Figure 20b shows the 500 nm hyperspectral frame in which the square pattern is clear. Due to the size, regularity, and orthogonality of the pattern we believe this pattern's origin has to do with the electron beam writing process that made the template used to imprint this pattern. Imprio 1100 template format is a 150 mm fused silica wafer that is 0.7 mm thick. Typically, the electron beam (e-beam) writers used for photomasks are also used for fabricating imprint templates. Photomask blanks are made out of fused silica and are known to have the "6025 format" which means that they are square in shape and are 6" by 6" by 0.25" thick (152 mm by 152 mm by 6.25mm thick). Imprio 1100 templates used in this work were prepared using 6025 templates written on e-beam writers, followed by glass machining steps that convert them into a 150 mm fused silica wafer that is 0.7 mm thick. E-beam writers typically have "writing fields" that range from 100 µm by 100 µm to 1 mm by 1 mm. These writing fields are written using electrostatic deflection lenses to rapidly

scan the beam locally. Larger regions are written by moving the stage that carries the 6025 substrate and stitching the smaller write fields. E-beam write issues are known such as stitching errors caused by imperfect stage positioning, beam size variations, dose variations, and shot noise [46]. It is likely that in this case of the approximately 300 x 300 µm regions shown by the square marked with dashed lines (Figure 19b), the center-to-edge dose variations within the e-beam writing fields have caused very subtle variations in the diameters of the pillars. This defect is a repeater, and as expected, appears in the exact same way in every wafer imprinted with this template. Depending on the optical sensitivity of the structure, the defect may or may not be visible in the data. In the case of the hourglass arrays, the optical sensitivity is sensitive enough to create a visible effect.

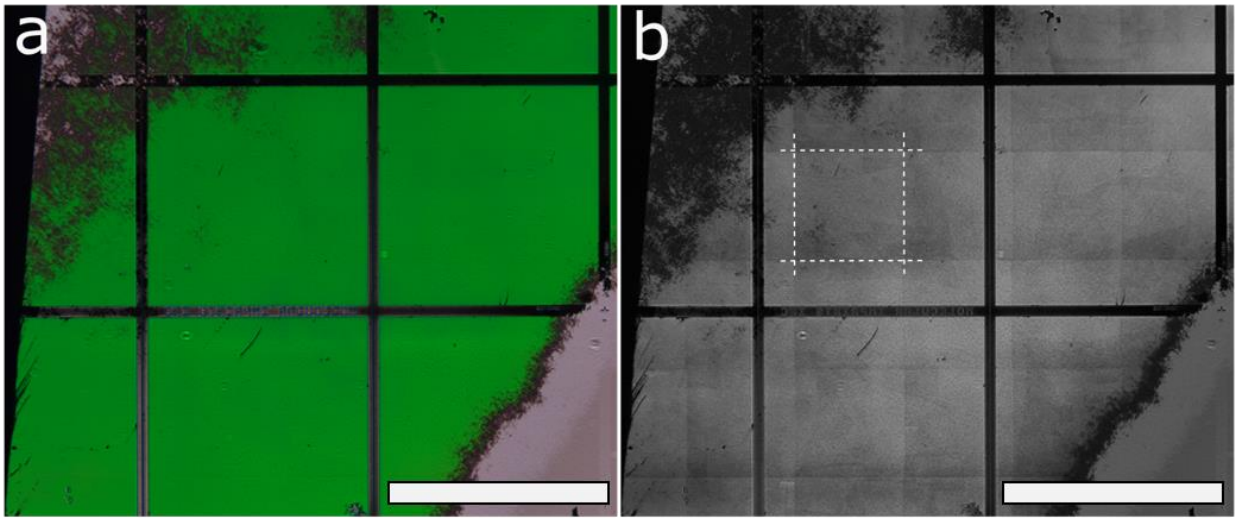

Figure 20. A portion of a green hourglass-shaped nanopillar array sample showing the pattern of squares created by the electron beam writing process that made the imprint template. (a) The RGB image. (b) The 500 nm hyperspectral frame with the dotted lines overlaid to show the square grid signature. (Scale bars = 1 mm).

ETCH RELATED DEFECT MODES

It is very common for LNAs to go to etching steps after imprinting is done. This typically begins with the descum etch process (shown in Figure 14) and then goes for a transfer etch process into the substrate material. Defect modes can arise in these various etch steps.

Delayed Etch Start and Etch Non-Start

A delay in the start of the etch – what we call a "delayed etch start" – can occur if the etch mask has not been broken through between the features prior to the etch that transfers the features into the substrate. This can occur for instance, if the descum etch does not break through the RLT in some areas. This causes the subsequent etch process to start in a delayed fashion, because the underlying material is not initially exposed to the etch process. Since etch selectivity is never infinitely high, the RLT often eventually etches away and then the substrate etch will begin, but this results in the features receiving less etch time than targeted causing shorter features. Also, this generally results in slightly larger CDs than expected, since some feature slimming is expected to occur in the areas that the RLT breaks through first.

This commonly occurs at the edges of patterned areas, particularly when a uniform drop pattern is used in conjunction with a hole-tone template (used to imprint a pillar array pattern) which has large areas of pattern adjacent to large areas of no pattern. The mechanism behind this is shown in Figure 21(a). If the drop pattern is distributed uniformly to all areas on the substrate, the fluid volume will build up in the unpatterned region beyond the pattern edge with nowhere to go other than to squeeze into the nearby patterned region

creating an increased RLT. It should be noted that JFIL allows non-uniform drop distribution and therefore the Figure 21(a) is a result of not choosing to use drop pattern variations to address pattern densities. Figure 21(b) show this effect in a wine glass array sample. In the wine glass arrays, the delayed etch start is seen to create darkening at the pattern edges and at the edges of particle voids. This darkening is due to the presence of partially broken through regions like what is shown in the SEM image in Figure 21(c). The partial breakthrough occurs where the RLT was thickest and as the RLT becomes thinner (away from the edge or away from the particle void center) the breakthrough becomes gradually more complete creating a transition type gradient like what is seen in the SEM image in Figure 21(d). In the transition region, the color of the wine glass arrays turns from dark, to reddish, and then returns to the nominal green color created by the normal wine glass arrays. The intermediate red color is likely due to the presence of larger features, the result of a strongly delayed, but complete breakthrough.

In the most extreme case of delayed etch start, the etch is delayed *so much* that it never begins at all, leaving behind an unpatterned area which takes on the characteristics of the bare substrate. In the wine glass wafer, the pattern in the central region of the template is meant to contain a 5x5 pattern of squares, but due to etch non-start only a few of the squares are successfully patterned as seen in Figure 21(b). Etch delay and non-start are typically found right next to each other as etch delay generally precedes etch non-start.

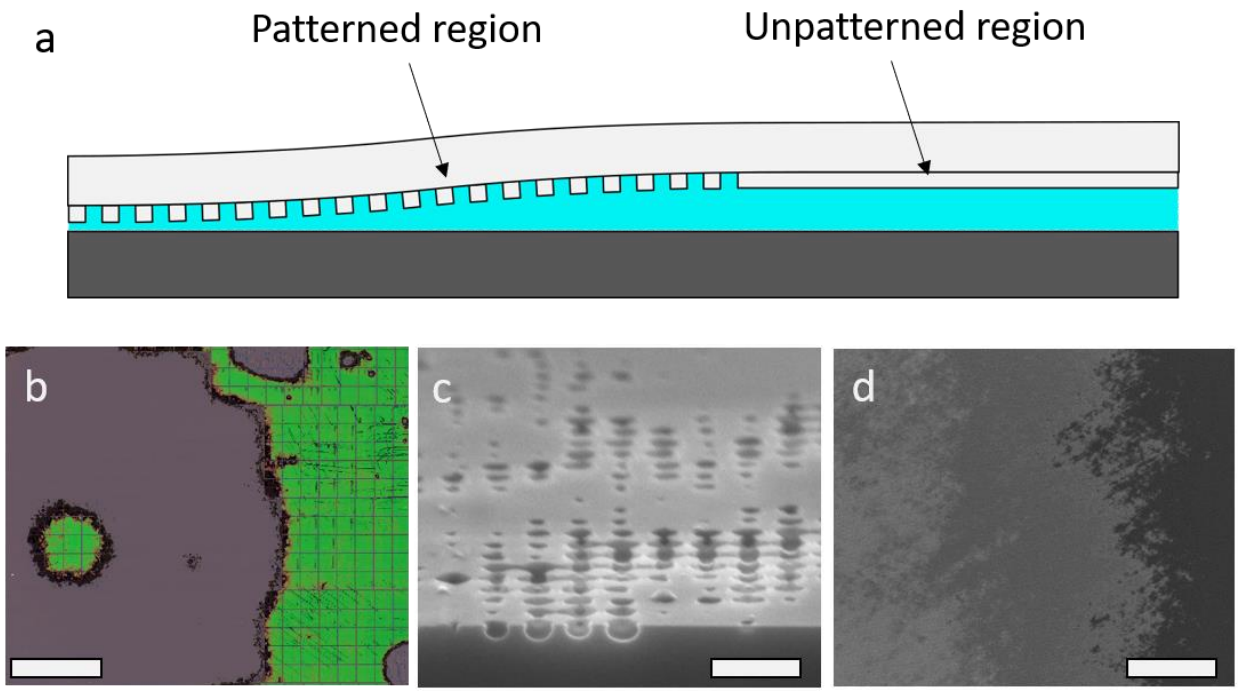

Figure 21. Etch delay and etch non-start. (a) schematic showing how the difference in pattern density results in RLT variations. (b) RGB image of a wine glass pillars sample containing pillars (green colored), a significant amount of etch delay (dark colored) and etch non-start (Si colored or gray colored region) (scale bar = 5 mm). (c) cross-section tilt SEM image showing the effect of an extreme etch delay in the fabrication of wine glass arrays (scale bar = 400 nm). The pattern is seen to be only just broken through by the end of the processing. (d) Top-down SEM image of a wine glass arrays sample showing the transition region taking place in an instance of etch delay (scale bar = 100 μm). The left of the image is where the normal pattern exists, the right side of the image is where bare Si exists due to etch non-start, and in between is a region containing some combination of the two.

Other etch defect modes

Center-to-edge variations are common in plasma etch processes in which the center of the wafer etches at a different rate than the edge. This can result in feature size variations and thus variation in the optical characteristics of the device from center to edge. Also, variations in the bulk etch rate can occur for a variety of reasons including inaccurate

chamber pressure, gas flow rates being off target, etc. These will affect the full device area resulting in either under- or over-etched features. Varying etch process parameters can also result in changes in lateral etch rates, causing effects like feature shrinking, necking, and micro-trenching. There are also known to be pattern dependent etch rate variations such as micro-loading and aspect-ratio dependent etch rates.

MACE Process Defect Modes

The metal assisted chemical etching (MACE) process has its own set of unique defect modes which make it very different than plasma etching. For instance, whereas large etch depth variations are relatively uncommon for plasma etched features (at least for relatively low aspect ratios), significant etch depth variations can occur in the MACE process which results in feature height variations if incorrectly mitigated. While MACE has been studied in the research literature for over 15 years, very limited literature on wafer-scale MACE uniformity data exists as would be needed in a manufacturing process. On the other hand, plasma etching is a highly mature process that has been used in the semiconductor industry for manufacturing integrated circuits for over 4 decades [47]. MACE etch depth variations can occur over a variety of length scales, including mm- to cm-scale as well as length scales equal to the pitch of the array itself. Figure 22(a,b) shows an instance of such etch depth variations. In Figure 22(a), we show the camera pixel size relative to the nanowire arrays. The pixel size, which is ~10 x 10 μm, covers an area equivalent to ~50 x 50 nanowires. In this case, the wires have a max height of ~1000 nm, and the depth variation is 100's of nm. The depth variations cause a relatively featureless

experimental spectra like the one seen in Figure 22(c). Spectra for nanowires having diameter of 130 nm and height of 900, 1000, and 1100 nm are simulated in Figure 22(d) and averaged to produce the spectra in Figure 22(e). The effect the averaging has on the spectra shows how the etch depth variations create the relatively featureless experimental spectra. Ongoing research has identified etching fluid flow non-uniformity as the major cause for etch depth variations and improved MACE etch depth uniformity is being developed [48].

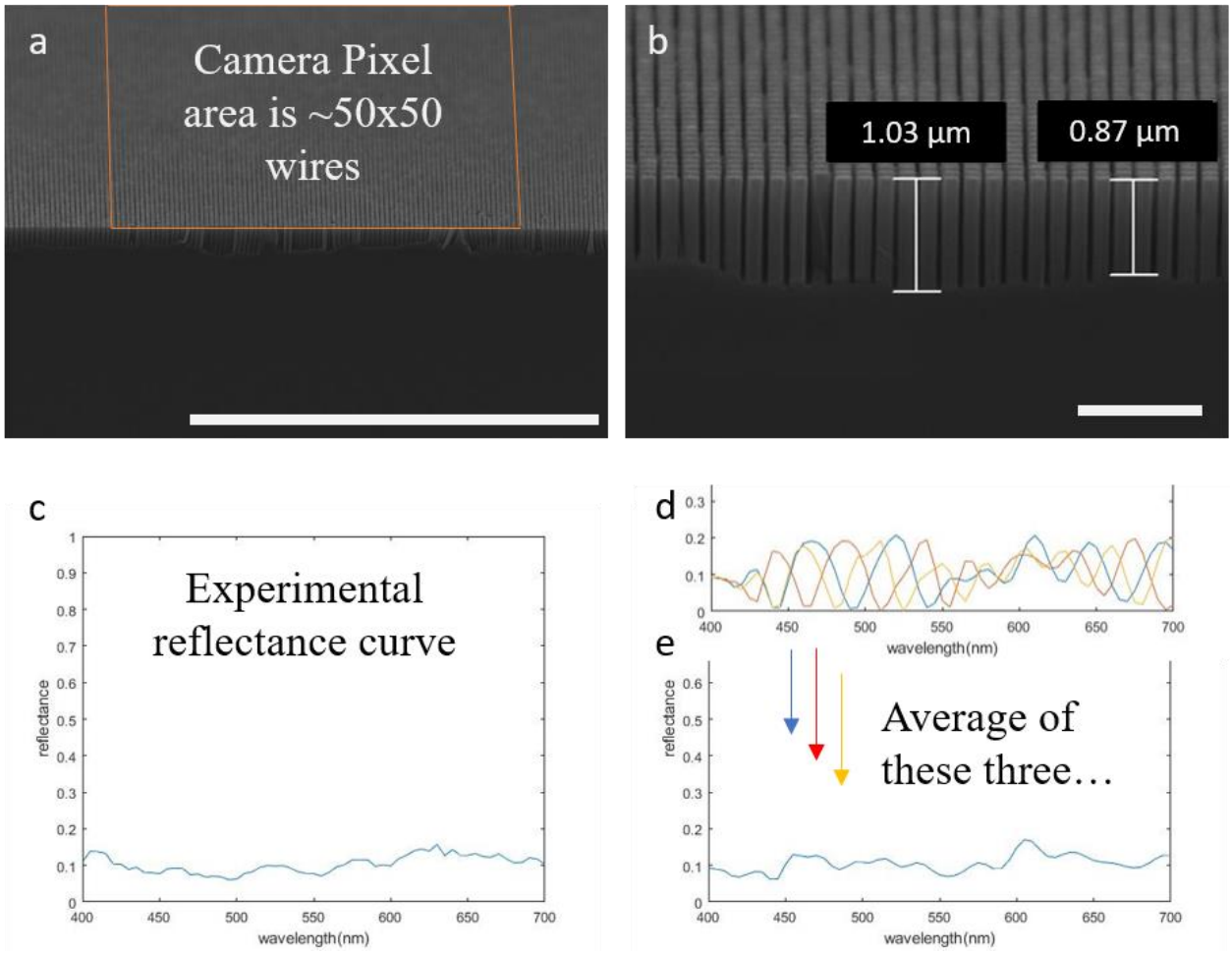

Figure 22. MACE nanowire array etch depth variation. (a) cross-section SEM image showing a MACE nanowire array with significant etch depth variations (scale bar = 10 um). The size of a single camera pixel is shown by the overlaid box in the image. (b) closeup of the cross-section SEM image in (a) showing the magnitude of the etch depth variations (scale bar = 1 um). (c) experimental reflectance spectra from the sample. (d) simulations of nanowire array spectra for wires with diameter of 130 nm and heights of 900, 1000, and 1100 nm. (e) the average of the three spectra simulated in (d). The effect the averaging has on the spectra shows how the etch depth variations create the relatively featureless experimental spectra in (d).

Feature collapse is also more relevant to the MACE process as compared to plasma etching. This is for two reasons: 1. The MACE process is typically capable of etching very high aspect ratio features due to its near-vertical etch profiles, and 2. The process happens

in a wet solution and upon drying capillary forces tend to collapse features into one another. Collapse in vertical nanowire arrays has been observed in many samples to form dark areas like what is seen in the RGB image in Figure 23(a). Using an in-situ spectral imaging system, collapse can be detected if the system is looking for areas that suddenly transition from having some color (or highly featured spectrum) to being dark (or generally low in reflectance).

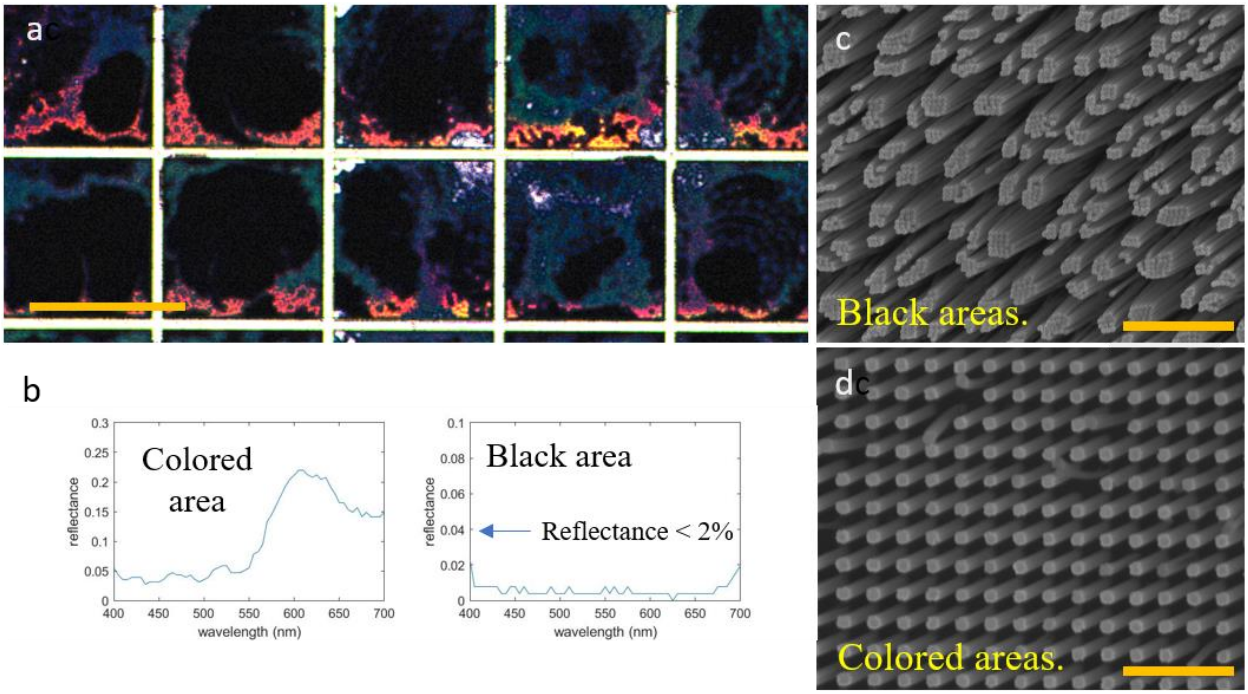

Figure 23. MACE nanowire collapse. (a) Cropped RGB image of a MACE nanowire array sample (scale bar = 1 mm). The brightness of the image has been increased to reveal the colored areas which contain normal nanowire arrays. The black areas contain nanowire arrays which have experienced collapse. (b) Reflectance plots showing spectra for the colored and black areas. (c) Top-down SEM image showing collapsed nanowires which is characteristic of the black areas in (a) (scale bar = 1 um). (d) Top-down SEM image showing collapsed nanowires which is characteristic of the colored areas in (a) (scale bar = 400 nm).

Chapter 4: Detection and Classification of Defects in LNAs using Spectral Imaging

Now that we have a good understanding of the fabrication processes behind LNA manufacturing and how these processes can create defects, we will explore how spectral imaging metrology can be employed to detect instances of these defects as well as classify them. Detection is relatively straightforward, in that excursions from desired or expected optical behavior are easily identified, but classification, that is, linking a defect to a specific root-cause, becomes a significantly more challenging problem. Further, classification (as compared to detection) is significantly more valuable in volume manufacturing as solving a defect problem requires knowing its root cause. Naturally, both of these problems are handled *via* image processing of the spectral image dataset. In this chapter, we will explore how spectral imaging systems can be used to detect and classify defects in LNAs.

DEFECT DETECTION

The problem of detecting defects is relatively straightforward. Essentially, all the pixels in the measured image sets are compared to target values and if they are not, for instance, close enough to the target values (or far enough away, above, below, etc.), those pixels are determined to be defective. For instance, we may need to inspect an MMG for having acceptably high transmittance, or we may need to inspect a nanowire array to assess whether its color suggests that its etch depth is on target... In any case, we need to choose a target range for the image sets that accurately represent the yield condition for the specific LNA being inspected, so that anything that is not in the target range can be considered a defect.

The choice of the yield condition is inherently the most difficult part about detection, because it needs to be based on a good understanding of the optical properties of the specific LNA being inspected and how defects alter those properties. Once in place, however, the actual algorithm used for the detection is relatively straightforward. To understand how a yield condition can be chosen, we have developed a demonstration based on a wafer containing wine glass shaped Si nanopillar arrays.

The fabrication process for the wine glass Si nanopillar arrays is shown in Figure 24 along with a cross-section SEM image of wine glass arrays. After imprint and descum, the wafer undergoes a short anisotropic plasma etch to define the head of the wine glass structure using a standard reactive ion etching (RIE) tool. Then the wafer is transferred to a deep Si RIE tool where a single cycle of the Bosch process is applied. First, a Teflon sidewall protection layer is deposited which is then broken through with an anisotropic etch, and finally, an isotropic etch is performed on the exposed silicon creating the stem-like feature of the wine glass structures. The fabrication process has several steps, and there are correspondingly many ways in which the fabrication can go wrong, creating a variety of defects that we'll see exhibit interesting optical characteristics.

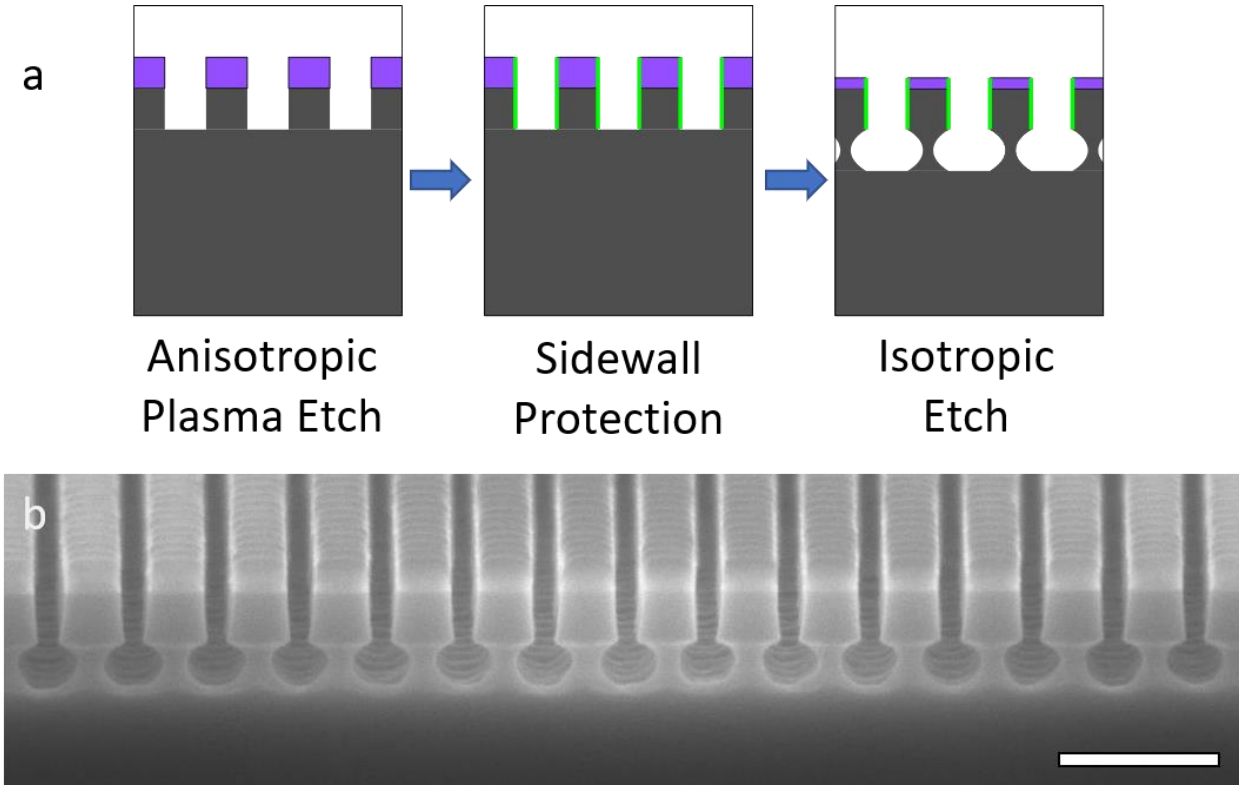

Figure 24. (a) Etch fabrication process for creating wine glass shaped Si nanopillar arrays. (b) Cross-section SEM image of a wine glass Si nanopillar array (scale bar = 400 nm).

Figure 25 shows an RGB image of a wafer containing wine glass-shaped nanopillar arrays. Most of the patterned area on the wafer is a bright green color. This is due to the Mie resonance effect exhibited by the pillars in the array which, for this particular size of pillar, happens at about 530 nm, a green wavelength. Variations from this nominal geometry cause differences in the spectra and colors exhibited by the arrays. There are some splotches of a reddish color, for instance, the result of a slight redshift in the Mie resonance suggesting that the heads of the pillars in these areas are slightly larger than the nominal ones that are green, probably the result of locally thicker RLT. The wafer has also been affected by a variety of patterning defects such as imprint particles and etch delay

causing regions like the ones labelled in Figure 25 which consist of dramatically different colors like black and gray, as well as different sizes, shapes, and location. We will use this information to help *classify* these defects later, but for now we simply aim to detect the presence of defects in general.

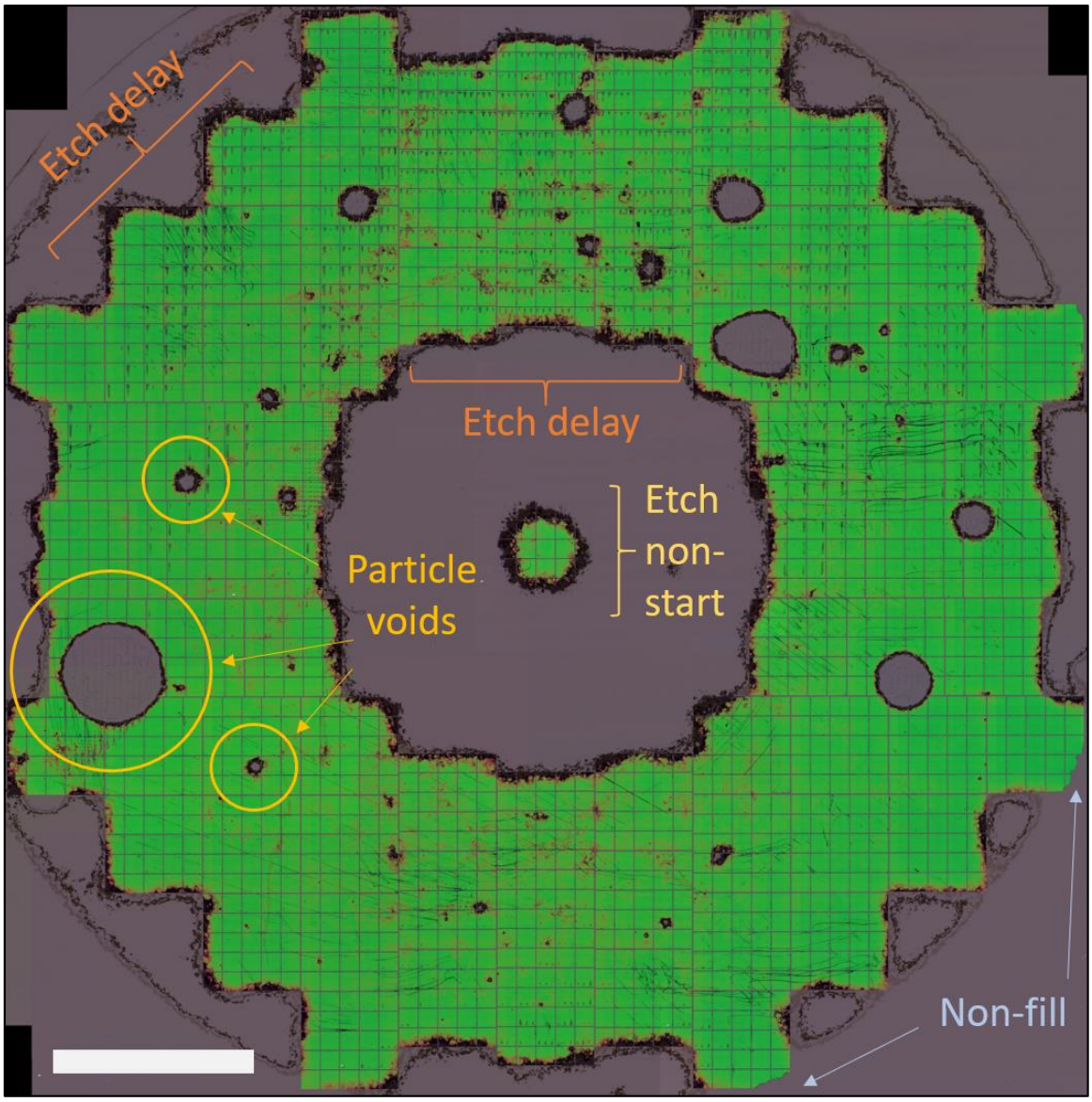

Figure 25. Stitched RGB image of wafer of wine glass-shaped nanopillar arrays with different types of defects labelled (scale bar = 1 cm).

Defects like these need to be detected so that the manufacturing line can manage its yield, and detection must be done in an automated fashion. One way to detect these defects is simply by screening the colors in the RGB image and finding pixels that have

colors that are sufficiently different from the color that is produced by structures with the correct geometry, in this case the bright green color. The first thing that needs to be done is establish a quantitative definition for the yield condition. This is done by setting a range of acceptable values for the pixels comprising the image.

Each pixel in an RGB color image consists of 3 different values: Red (R), Green (G), and Blue (B). Different combinations of these values produce different colors with varying levels of brightness and saturation. A different color space called HSV (Hue-Saturation-Value), offers a great advantage over the RGB color space visualized in that color attributes like hue, color purity (saturation), and brightness are separated into discrete channels. For instance, the hue of a color, or the "shade" (i.e. red, green, yellow, turquoise), is completely captured by the first value H (Hue) in HSV. In RGB space, on the other hand, the hue is entangled amongst the three-color values. The two different color spaces are visualized in Figure 26.

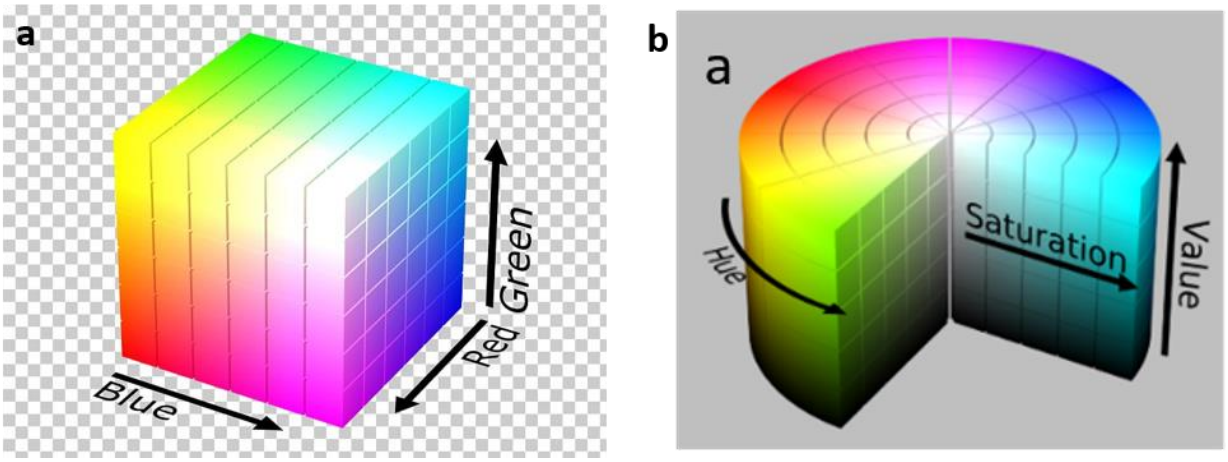

Figure 26. (a) Schematic visualization of the RGB color space (courtesy imgbin.com). (b) Schematic illustration of the HSV color space (image by wikipedia user SharkD, distributed under a CC BY-SA 3.0 license.).

The HSV color space offers a great deal of intuition which is helpful for defining the yield condition. The green color on the wine glass sample in HSV, for instance, is [92, 202, 167] (here we use 3 8-bit values ranging from [1, 1, 1] to [255, 255, 255]). The hue value of 92 means that we have a greenish color. The high S and V values indicate that the color is also very saturated and bright. This same color in RGB is [35, 167, 57]. The RGB values must be looked at relative to one another to make sense of them, hence the entanglement.

To perform successful defect detection on the wine glass wafer we have found the following constraints on the yield condition to be effective: **115>H>60, S>140, V>140.** These constraints as applied to the HSV color space are visualized in Figure 27.

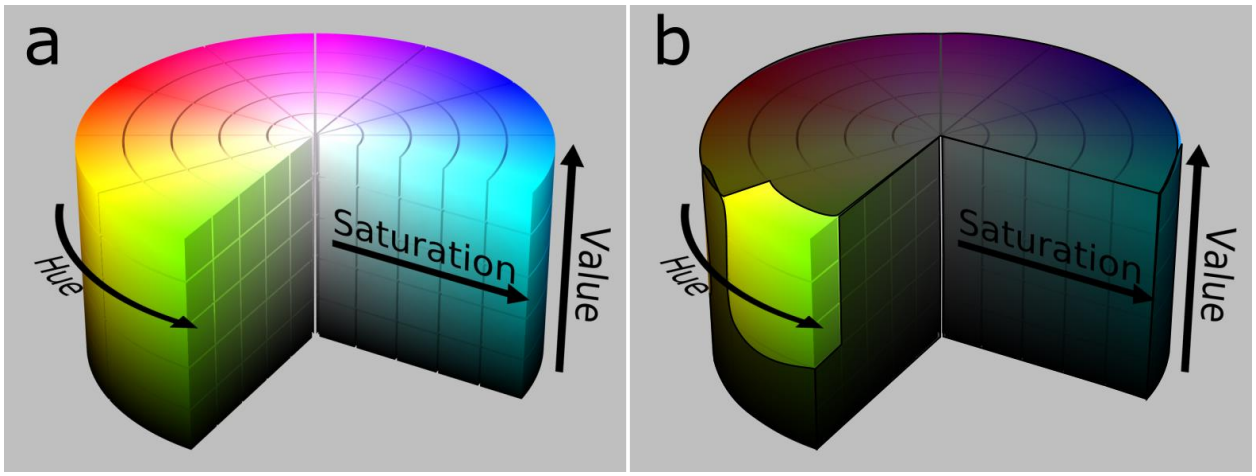

Figure 27. (a) Visualization of the HSV color space (image by wikipedia user SharkD, distributed under a CC BY-SA 3.0 license.). (b) Visualization of the yield constraint as applied to the HSV color space. Only bright, saturated green colors remain after the space is constrained.

The yield condition is applied to the HSV image of the wafer by applying image binarization to the individual image layers H, S, and V. The layers for the full wafer and a

closeup of one of the particle exclusion zones are shown in Figure 28. The individual image layers are visualized in grayscale with black corresponding to a value of 0 and white corresponding to 255. Dramatic differences exist in the HSV values between the various defects, such as the particle zone, and the yielded areas of the wafer. Notice how the different regions of the wafer affect the various HSV values. The void regions, where we have bare Si, for instance, has a very low saturation value, appearing almost black in the S layer. This is because these regions are gray, and gray is the most unsaturated of all colors. Also notice how the etch delay regions on the edges of the wafer are very dark in the Value channel, but not in the Saturation channel. This implies that there is in fact some prominent coloration to the etch delay regions, but the color is very dark. There are features in the etch delay regions exhibiting nanophotonic activity, but they are highly absorbing.

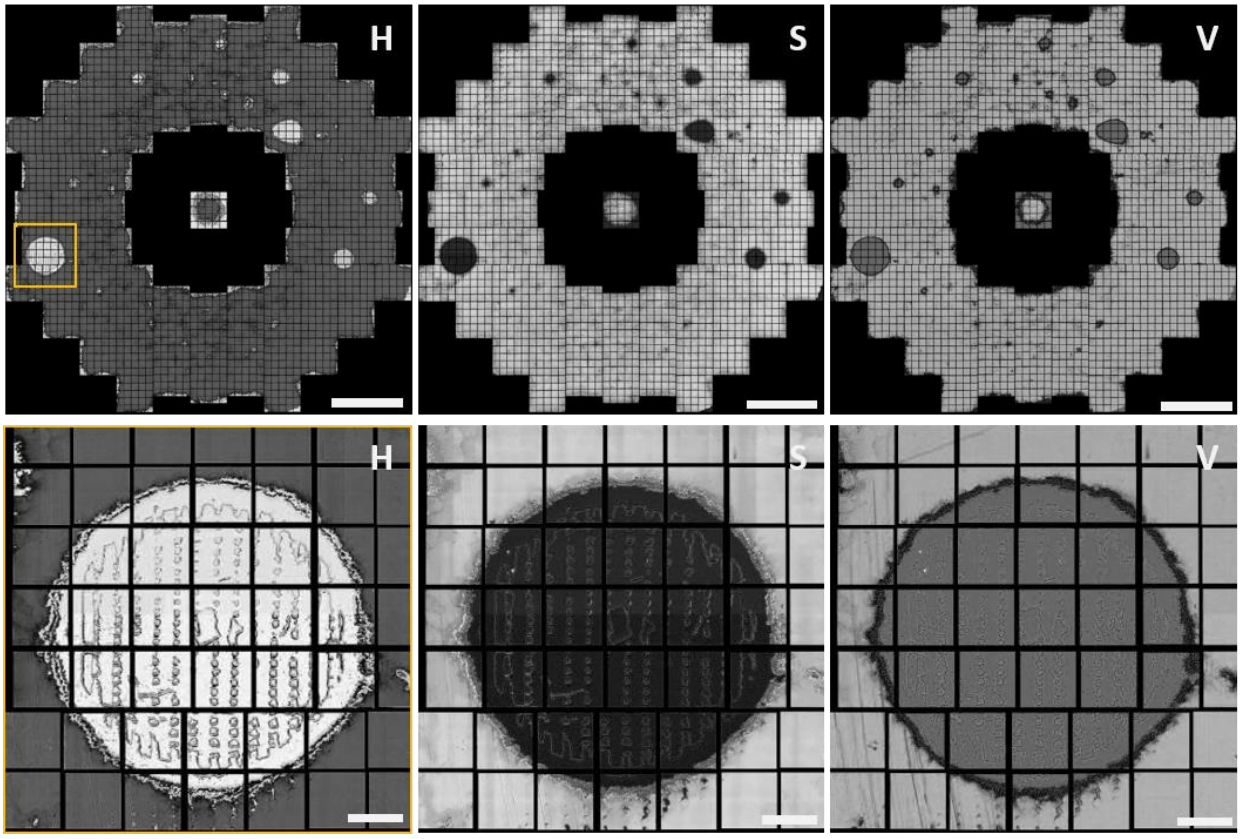

Figure 28. Top row) HSV Image layers for the full wafer image (scale bars = 1 cm). Bottom row) HSV image layers for one of the particle exclusion zones (scale bars = 1 mm). The cropped region is shown in the top left image. The individual image layers are visualized in grayscale with black corresponding to a value of 0 and white corresponding to 255.

When we apply the yield condition, we get the result shown in Figure 29(a) in which the green pixels have been identified as yielded and red pixels have been identified as defective. The scheme does a good job at detecting most of the noticeable defects. As an example, we can go further and treat each of the squares as individual device areas and then determine the "device yield" based on an acceptable threshold for yield fraction within the individual device areas. If we desired that the device areas have greater than 90% of

pixels in the dataset be yielded, for instance, we would get the device yield map shown in Figure 29(b).

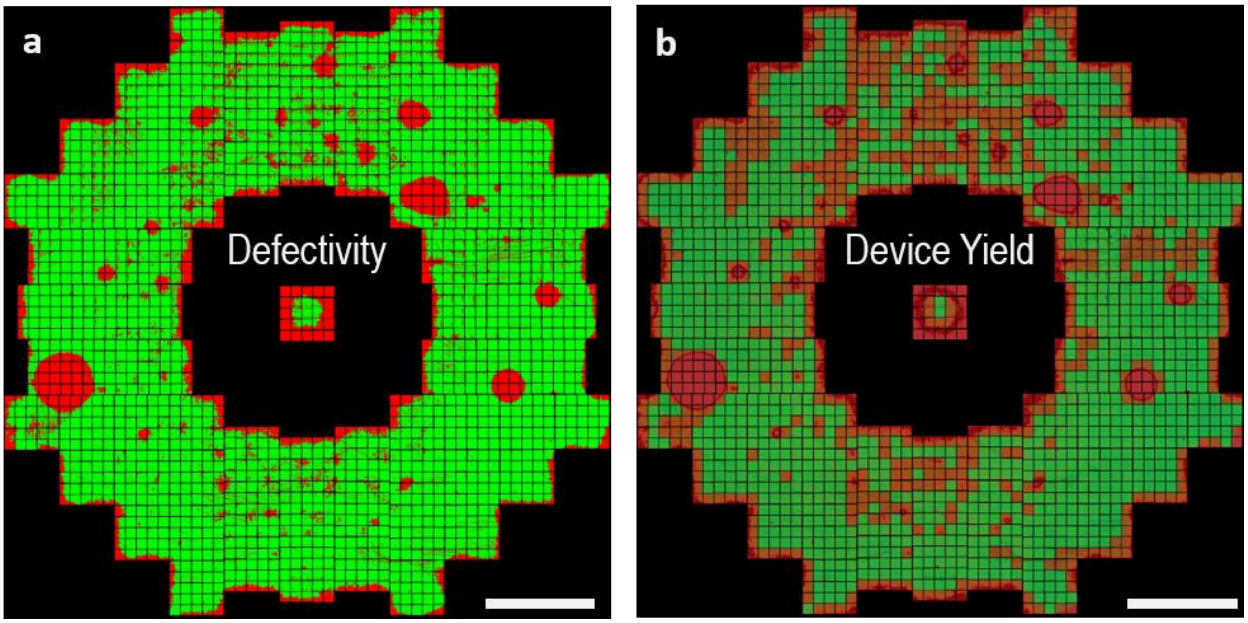

Figure 29. (a) defectivity image for a wafer of wine glass arrays (scale bar = 1 cm). (b) device yield image corresponding to (a) (scale bar = 1 cm).

In the case of this particular wafer, many of the defects affecting the arrays were quite obvious, and thus readily detectable from the RGB image, and the yield condition we defined does a good job of detecting these types of defects. However, more subtle variations in geometry exist within the nominally green areas that could be considered to be defective depending on the requirements of the final device. To achieve this, the constraints on the HSV values could be more tightly specified.

Instead of having the yield condition based on color values, a target *spectrum* can be utilized, putting the full hyperspectral image set to work. This inherently provides finer grain information and is also useful for quality control in the situation where a particular

spectral behavior is the intended function of the end device i.e. for image sensors, display pixels, color printing, etc. Figure 30 shows an RGB image and various hyperspectral frames from the upper right section of the wine glass wafer. The hyperspectral frames reveal how the spectra capture a great deal of information that isn't readily visible in RGB image. In particular, the hyperspectral frames near the resonance reveal the e-beam write pattern signature on the wafer. The 450, 500, and 550 nm hyperspectral frames show the e-beam signature very clearly. Now, having seen the e-beam signature in the hyperspectral frames, it is easier to see the e-beam pattern in the RGB images, nonetheless it is still quite difficult to see.

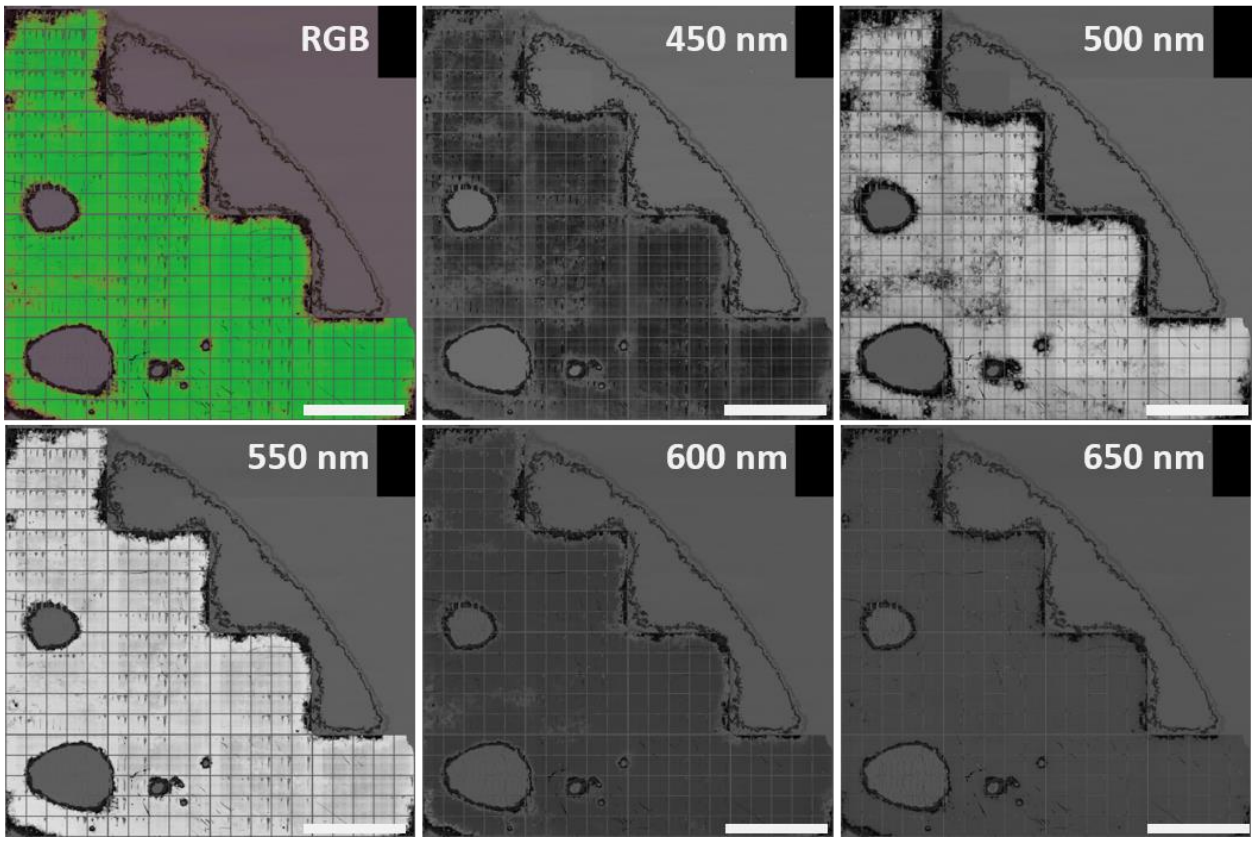

Figure 30. RGB image of upper left portion of the wafer of wine glass arrays and five hyperspectral image layers for the same area taken at 450 nm through 650 nm (scale bars = 5 mm).

To illustrate how spectra can be used for defect detection, a spectrum is taken from one of the green areas and is used as a "target" spectrum. Then, an RMSE (root mean square error) is calculated between this target spectrum and every spectrum on the sample. We choose to set the defectivity threshold to RMSE ≥ 0.05. The choice of RMSE ≥ 0.05 is arbitrary but does a good job of detecting subtle color variations caused by the e-beam write defect. This result is shown in Figure 31.

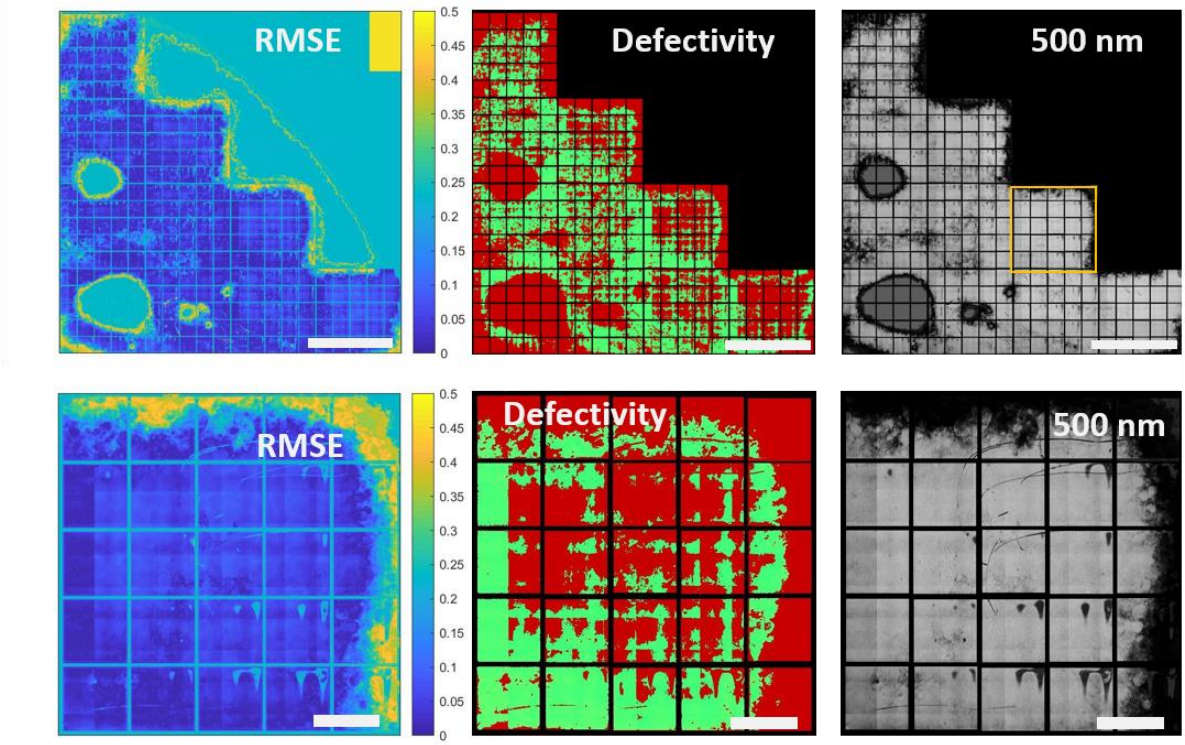

Figure 31. Defectivity analysis on section of the wine glass arrays wafer based on target spectrum yield condition. (Top row) RMSE, Defectivity, and 500 nm hyperspectral frame images for the upper-left portion of the wafer containing wine glass arrays. (Bottom row) RMSE, Defectivity, and 500 nm hyperspectral frame images for a closeup view.

To get a feel for how large RMSE = 0.05 is, we show the yield condition spectra and a spectrum with RMSE = 0.05 in Figure 32. The difference in the spectra is very subtle. Actually, such a difference can be captured in color space coordinates as well despite being almost imperceptible to the eye. The RGB color values, which are listed in Figure 32(c), are actually significantly different, primarily in the red channel. The R value at point 2 is about 25% smaller than at point 1. This is because the spectra at point 2 is blue-shifted slightly from the target spectra taken from point 1 making it slightly less red. Knowing the

resonant behavior of the wine glasses and the effect of the e-beam write defect to cause CD variations, this is likely due to the wine glass heads having slightly lower diameter at point 2 than they do at point 1.

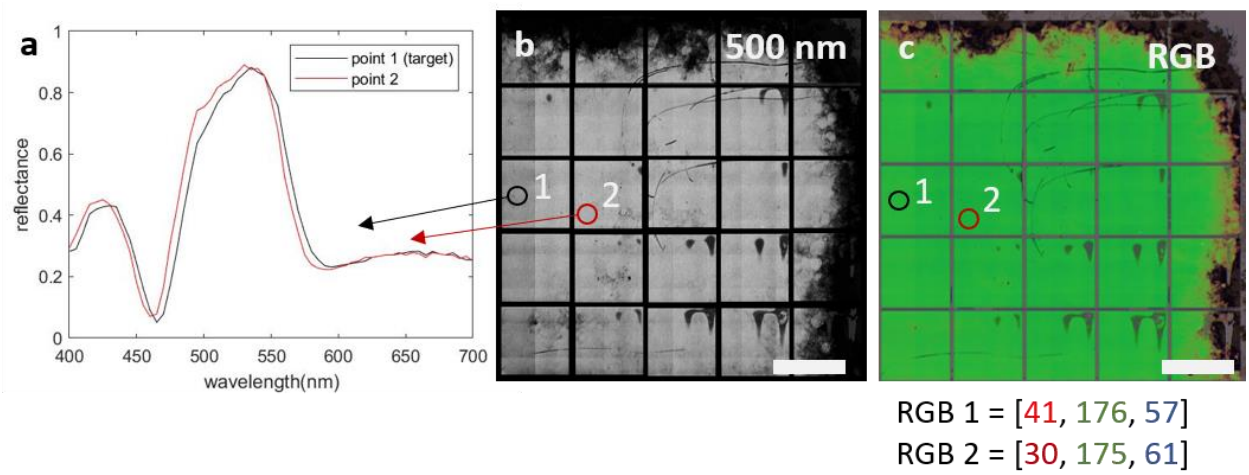

Figure 32. (a) Reflectance spectra from two different areas in the sample. (b) 500 nm hyperspectral frame with the two areas the spectra were taken from labelled (scale bar = 1 mm). (c) RGB image of the same region of the sample shown in (b) along with the RGB values taken from the two areas labelled in (b) (scale bar = 1 mm).

Color data, such as RGB and HSV, can be extremely sensitive to slight variations. In fact, color variations such as the one shown in Figure 32 could be detected by an RGB camera. Where an RGB camera really falls short, compared to a multi- or hyperspectral system, is the potential for different spectra to produce the *same* RGB values. After all, the Red, Green, and Blue channels integrate over relatively large ranges of wavelengths, and within these ranges, variations (even fairly large ones) could be present which just happen to produce the same overall intensity. Thus, there is some inherent level of convolution to using the higher-level spectral imaging technologies like RGB and broadband that

ultimately limits their effectiveness. Nonetheless, broadband and RGB systems are inherently much faster, and can be effective for detection up until a certain point when this convolution becomes important. This point must be considered based on a thorough understanding of the LNA optical behavior.

Other Examples

Wire Grid Polarizer

Wire grid polarizers (WGPs) are characterized primarily by their contrast ratio, which is the ratio of the transmittance of p- to s-polarized light. The contrast ratio image at 550 nm for a WGP sample measured by our spectral imaging system is shown in Figure 33(a). The contrast ratio goes as high as ~15,000. If we perform a defectivity analysis with desired CR>11,000 we get the defectivity image shown in Figure 33(b). In both images a 1D periodic variation is seen to run top to bottom in the image. This is due to CD variations in the WGP lines caused by RLT variations due to incomplete drop spreading, as discussed in Chapter 3. These variations are large enough to cause certain areas to be defective independent of the other patterning defects such as the ones indicated by the large round splotches.

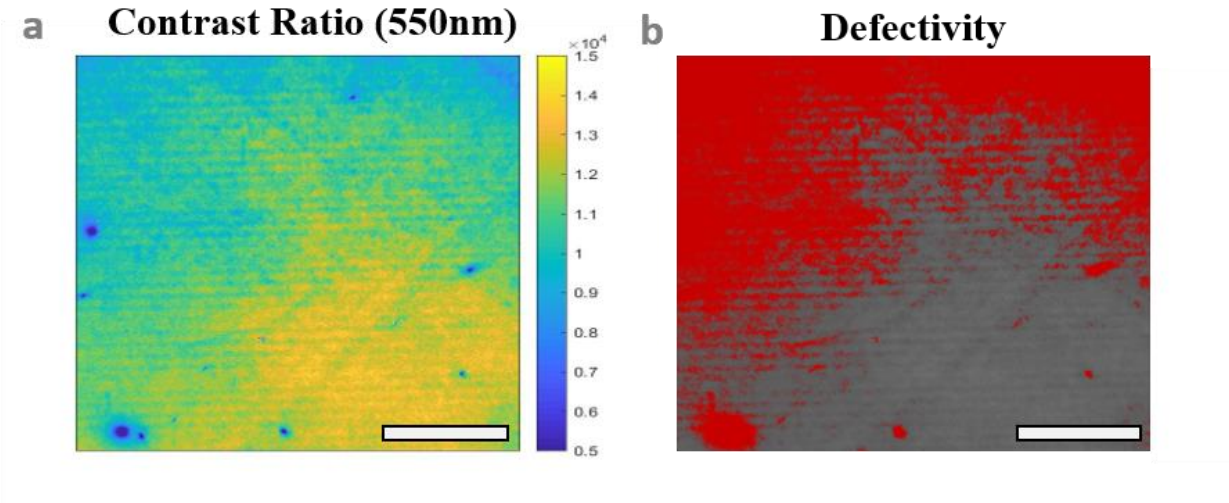

Figure 33. WGP defectivity analysis. a) Contrast ratio image at 550 nm for a wire grid polarizer sample (scale bar = 5 mm). b) defectivity analysis on the WGP, in the defectivity map the red regions are assumed to be defective (scale bar = 5 mm).

Metal Mesh Grids

Figure 34 shows a defect detection scheme for detecting various defects in an MMG (metal mesh grid) fabricated on a polycarbonate substrate. In this detection scheme, we take the blue channel image, B, from the RGB data and set the yield condition to be $0.3<B<0.5$. This range captures areas that are both low in transmittance (undesirable for transparent conductors) and also areas that are too high in transmittance, which is generally due to defects such as delamination which expose the underlying substrate.

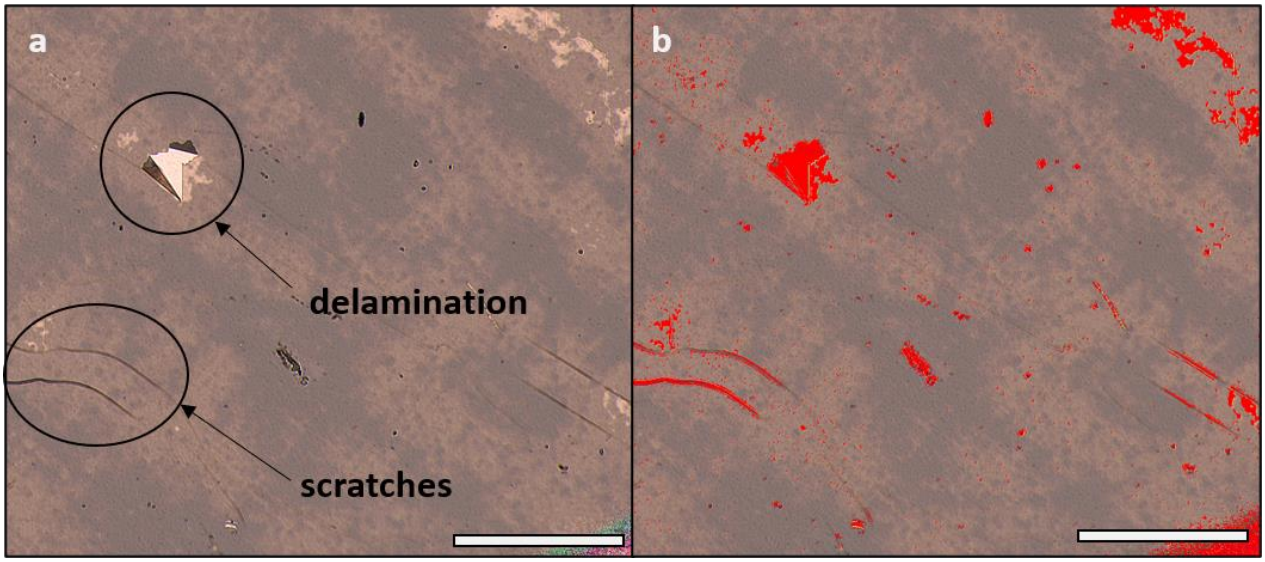

Figure 34. (a) Metal mesh grid on polycarbonate substrate (scale bar = 5 mm). (b) Defectivity map showing defect regions in red (scale bar = 5 mm).

Figure 35 shows a defect detection scheme for a different MMG fabricated on a fused silica substrate. The fused silica substrate produces noticeably better results than the polycarbonate (PC) substrate in terms of uniformity and delamination. This is believed to be a consequence of the fact that fused silica is generally a higher quality substrate with low surface roughness, and lower surface and bulk defects as compared to PC substrates. From the RGB image in Figure 35(a), it looks as if uniformity is superb. However, if we take the blue channel from the image and perform contrast enhancement, we get the image shown in Figure 35(b), which reveals a great deal of variation. These variations in transmittance are likely to be due to linewidth variations in the mesh lines, and it is very likely that these variations originate in RLT variations. The splotchy pattern resembles what was seen in the WGP contrast ratio image which was determined to be the result of the drop pattern signature, and thus it's highly likely that is the case here as well.

The defect detection follows as it did before with PC substrates, but this time with 0.395<B<0.7. Note that the contrast enhanced image is not used for the defect detection. It's simply meant to be a visual aid. Contrast enhancement can't actually add information to the dataset.

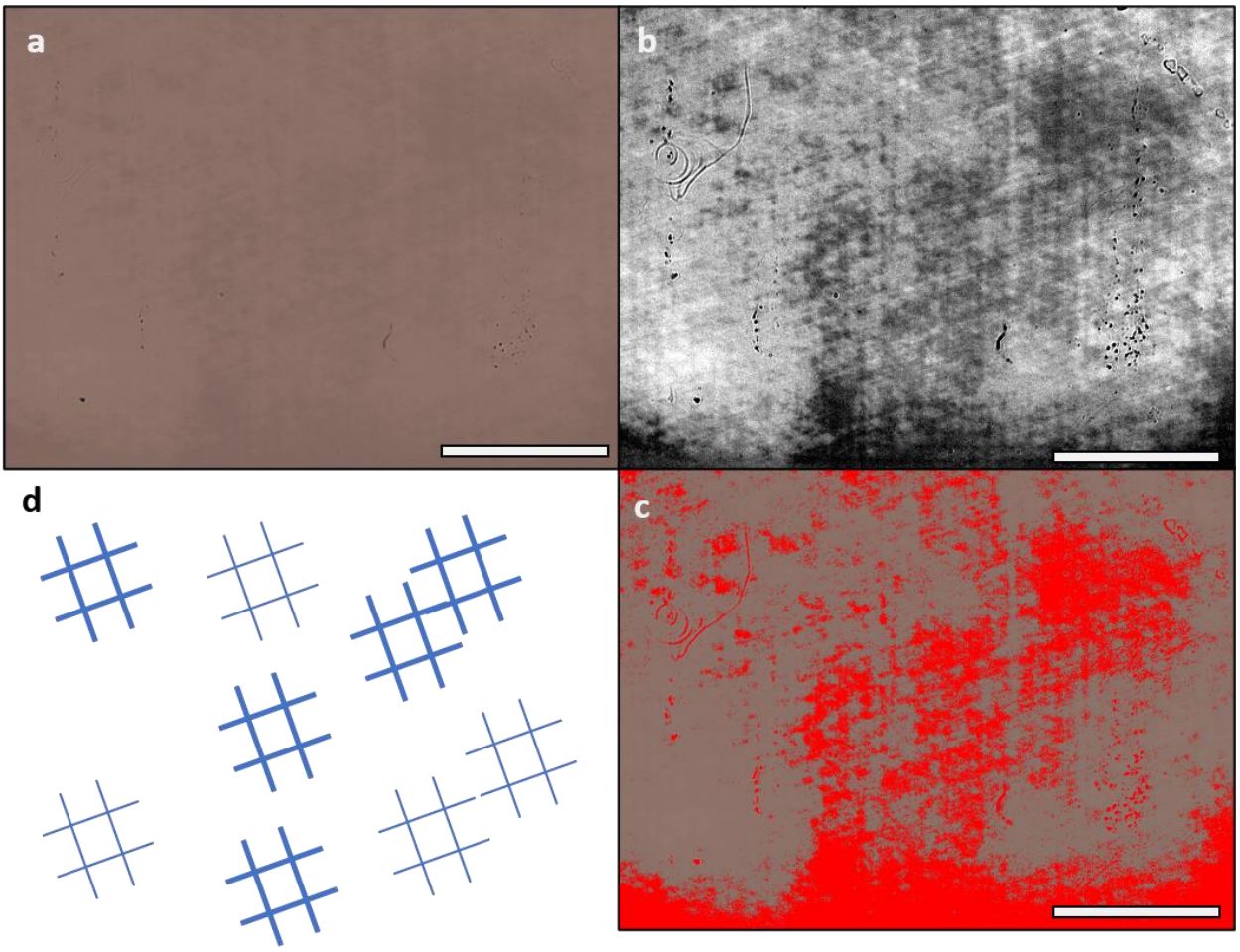

Figure 35. Metal mesh grid on glass substrate. (a) RBG image of metal mesh grid sample on glass substrate (scale bar = 5 mm). (b) Contrast -enhanced blue channel of the image in (a) (scale bar = 5 mm). (c) Defectivity image of the image in (a) with red regions being defective (scale bar = 5 mm). (d) illustration of duty cycle variations in metal mesh grids.

DEFECT CLASSIFICATION

Now, with the ability to detect defects, we must go further and classify the defects so that their root cause can be determined. Root-cause determination is invaluable, because it enables the manufacturing facility to pursue solutions to the specific problems in the manufacturing processes which are affecting yield. Otherwise, simply knowing un-classified defects exist is not incredibly helpful.

For this demonstration, we will return to the wafer of wine glass nanopillar arrays discussed previously, a large image of which is shown in Figure 25. Based on our knowledge of the manufacturing process, and the optical behavior of the wine glass structures, we can, from just a brief observation of the RGB image, tell that the wafer contains many imprint particle voids as well as a great deal of etch delay at the edges of the pattern, including some instances of etch non-start, as well as non-filling occurring at the pattern edges (please refer back to the qualitative discussion of these defects in Chapter 3). Our speedy classification of these various defect modes might make the classification process seem easy, but really this is just a testament to the highly effective image processing capabilities of the human brain. On the other hand, getting a computer to classify defects can actually be quite challenging. Nonetheless, this must be done for the sake of automating the process of defect classification. To demonstrate this, we have developed image segmentation-based schemes for classification of particle void defects as well as the edge-related defects like etch delay, etch non-start, and edge non-filling.

The classification process begins by pre-processing the data to simplify the subsequent analysis. We start by taking our detected defects (the defectivity image from

Figure 29(a)) and then perform color indexing on the defective pixels, a process which quantizes the pixels to a reduced set of colors. Color indexing is useful, because it locates areas with different colors. Color can be a very useful basis for defect classification. We start by finding black and gray pixels which generally correspond to the areas affected by etch delay and areas of bare Si, respectively. The image is thresholded based on the values in Table 3.

Table 3. HSV threshold values for indexing of black and gray pixels.

	H	**S**	**V**
Black	-	-	V < 75
Gray	-	S < 50	V > 75

The remaining pixels are then indexed to one of two colors, red and faded green, as detailed in Table 4 based on whichever they are closest to in the HSV color space. This is done with a Euclidean distance calculation in the three-dimensional HSV color space.

Table 4. HSV threshold values for indexing of red and faded green pixels.

	H	**S**	**V**
Red	120	119	55
Faded green	50	90	50

Once the image has been color-indexed, the process of segmenting the image is greatly simplified, and we can proceed with the classification schemes. Two different schemes have been developed: One for classification of the imprint particle voids and another for classification of the edge-related defects.

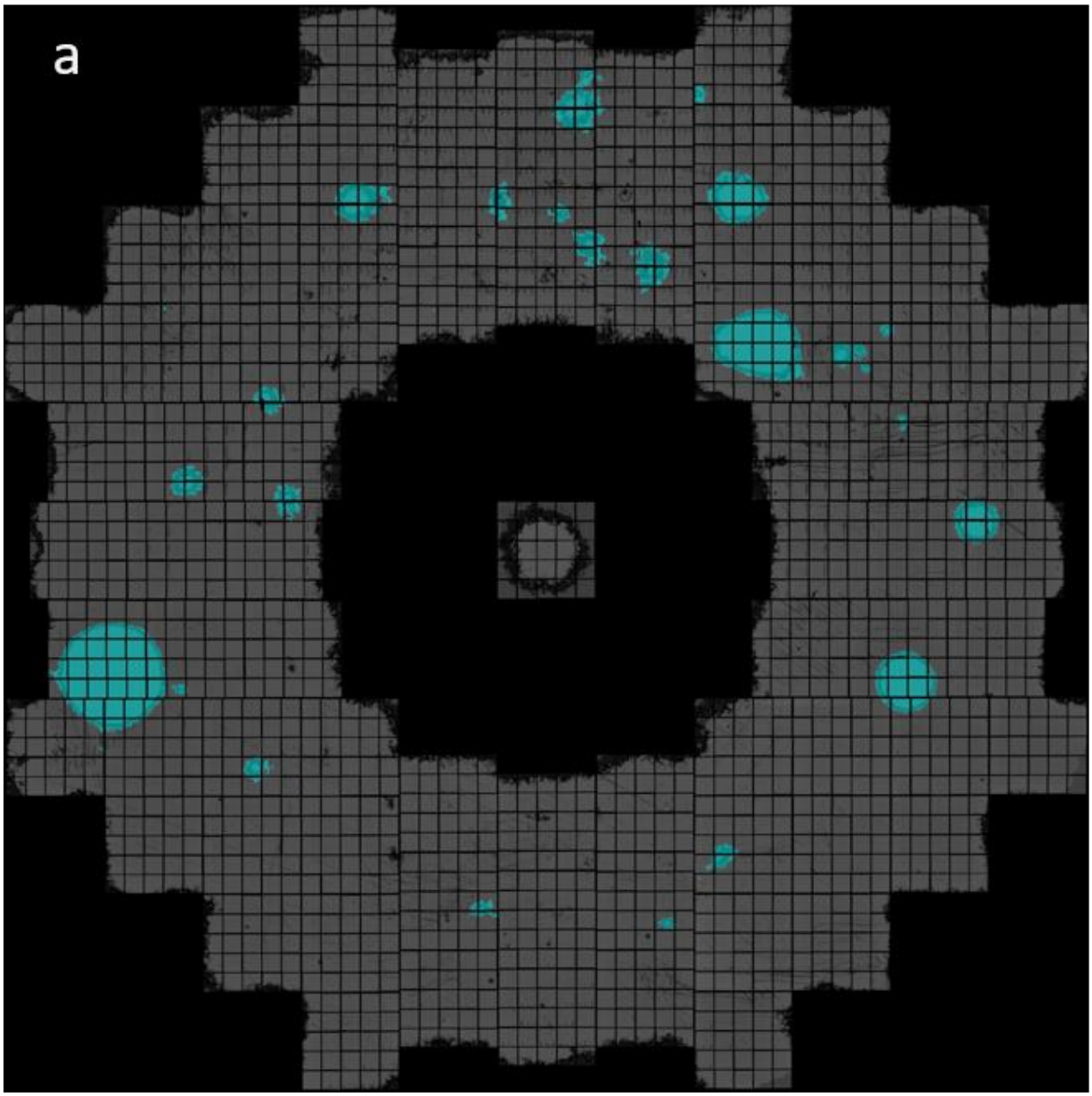

Figure 36. Defect classification results showing classified imprint particle defects in turquoise.

The scheme for classification of imprint particle voids makes use of the presence of the black ring surrounding the particle exclusion zones. First, the scheme goes square by square through the color-indexed image and looks for regions of gray. The scheme then

determines the fraction of the region's perimeter which is occupied by each of the 5 different indexed colors. If the fraction of black pixels surrounding the region is the highest, the region is assumed to be an imprint particle defect. In certain squares, only the ring region of the particle is present and thus would be missed by the algorithm, so squares that are immediately adjacent to the squares containing previously classified particle defects are assessed for containing a black or red region that is immediately adjacent to the previously classified region across the street between the squares, or in other words, that appears to be a continuation of the previously classified region.

Originally, we tried a different classification scheme for particle voids which hinged on their apparent roundness, or circularity. The circularity term, $C = P^2/(4\pi A)$, was applied but was not effective at differentiating between smaller particle voids and non-filling voids. There is clearly a difference in the apparent roundness between these types of defects – non-filling voids notoriously have very sharp straight edges – so perhaps a more effective quantitative description of this roundness could be utilized effectively. Regardless, the perimeter approach works reasonably well, although does have its own shortcomings. In particular, this approach is vulnerable to making incorrect classifications on smaller scales when the image resolution becomes poor. At this point, pixels start blurring together and fringes form around small features, causing the image accuracy to be compromised. In some cases, this causes the edges of small non-fill voids to be quantized to the color black, striking a false positive for the particle scheme. Furthermore, very small particle voids, < 100 μm, blur enough to obscure the gray region in the center, meaning this scheme would not classify them. It's possible that particle defects of this size could be

differentiated, and a separate scheme could be developed for them, or a higher resolution imaging system could be utilized.

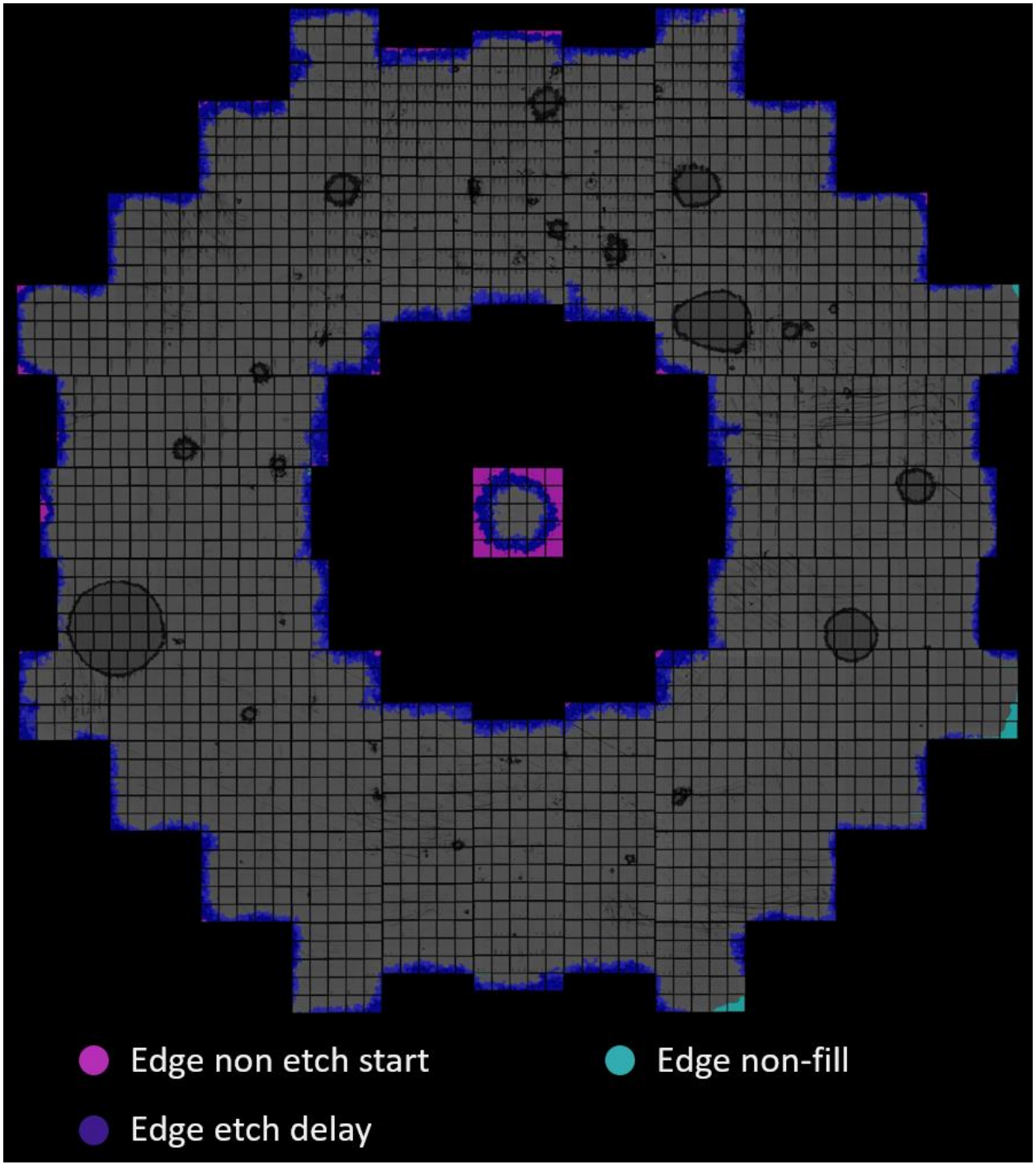

Figure 37. Image showing classified edge-type defects.

The classification scheme for edge-related defects looks at all the edge squares in the print area and determines whether there is a defect with the color gray, black, or red overlapping with the edge of the square corresponding to the respective edge of the print area (i.e. the west edges of the west-most squares). If there is a gray blob meeting this condition, the blob is dilated* and the colors of its perimeter pixels are analyzed. If the perimeter contains mostly black pixels it is deemed an edge non-etch start because this means its perimeter is shared with an occurrence of etch delay. If its perimeter is mostly green pixels it is classified as an edge non-fill, because this means its perimeter is shared with normally patterned pillars which is characteristic of non-filling.

**dilation is a common morphological operation performed in image processing which enlarges segmented regions of an image. The inverse operation, erosion, acts to shrink segmented regions.*

Then, of the remaining blobs, if the blob is black or red it is deemed an edge etch delay. Finally, the classified defects are propagated to the adjacent neighboring squares based on continuity across the streets as was done before with the imprint particles.

Collapse Classification in MACE Nanowire Arrays

As was discussed in Chapter 3, the MACE process has many relevant defect modes, and these must be detected and classified. One such defect mode is feature collapse, which occurs during MACE etching of high aspect ratio structures, such as tall vertical Si nanowire arrays. Collapse is easy to spot during MACE etching of nanowire arrays, because the color exhibited by the array turns very dark, nearly black. This is because the

overall reflectance, as shown in Figure 23(b), decreases dramatically, which we suspect is due to a graded index effect caused by the disordered forest of nanowires left behind after collapse has occurred.

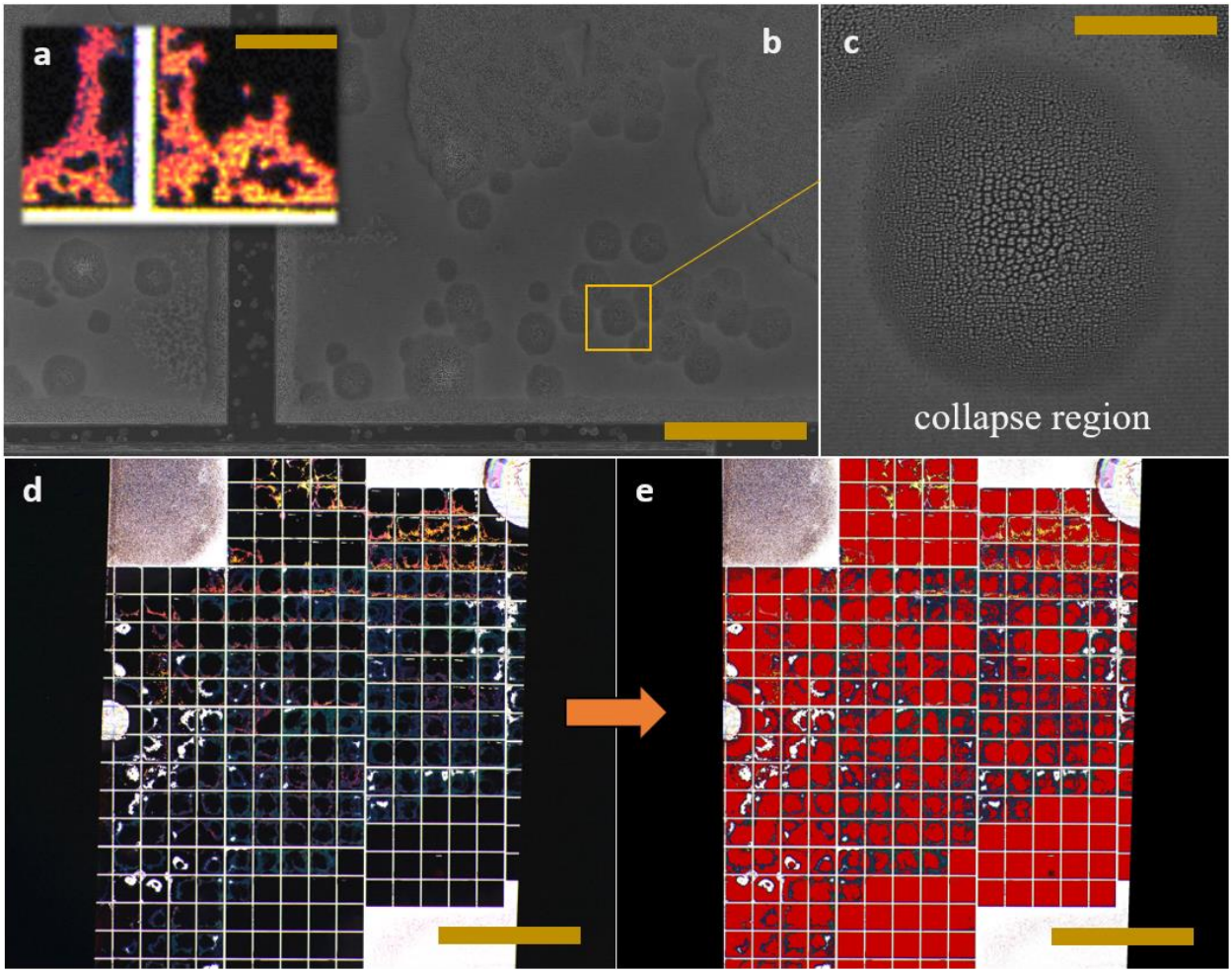

Figure 38. MACE nanowire collapse classification. (a) Closeup RGB image corresponding to the region shown in (b) (scale bar = 0.5 mm). (b) Top-down SEM image (scale bar = 150 µm). (c) Close up SEM image showing a small region of collapsed nanowires (scale bar = ~30 µm). (d) RGB image of a sample of MACE nanowire arrays containing collapsed nanowires (scale bar = 5 mm). (e) result of collapse detection performed on the sample in (d) and defective areas are labelled in red (scale bar = 5 mm).

Figure 38(a) shows a closeup of an RGB image of a MACE sample containing collapse. The black regions have experienced collapse and the regions with color have not collapsed. Note that the brightness in this image has been increased by 10X to provide visual aid. The collapse in this region was confirmed with top-down SEM measurements shown in Figure 38(b,c). The contiguous region, which looks as if it is sticking out of the image, corresponds to the orange area in Figure 38(a) which contains the un-collapsed arrays. Notice how this region is surrounded by collapse regions and also contains smaller, circular pockets of collapse within it, like the one shown in the closeup in Figure 38(c).

Collapse classification can be performed simply by looking for the dark areas in the sample. To our knowledge, there isn't another other defect mode which occurs in this MACE nanowire process which creates such a dramatically low reflectance. Thus, our scheme simply looks for dark areas. The RGB image shown in Figure 38(d) is first converted to HSV, and then the Value (V) image layer is constrained to V<4, producing the defectivity image shown in Figure 38(e).

In this chapter, we demonstrated how spectral imaging can be used to perform defect detection and classification in LNAs. It was demonstrated how excursions from expected optical behavior of an LNA can signal the presence of defects. It was shown how defects can be detected with a variety of spectral imaging technologies such as RGB imaging as well as hyperspectral imaging. In both cases, a yield condition is defined based on the expected RGB or spectral properties of the LNAs, and measurements falling outside an acceptable range are considered to be defective. Next, we went further to classify the

defects using imaging processing techniques which were able to differentiate between the unique characteristics of different types of defects. The detection and classification process has the potential to happen very quickly, especially when the process is to be done using RGB imaging systems because of their inherent high imaging speed compared to hyperspectral imaging systems.

In general, the detection and classification schemes we developed proved to be quite useful, however they do have limitations. Spatial resolution, in particular, seems to limit the ability of the spectral imaging system to classify certain types of defects. Small particle voids, for instance, were not effectively classified, and small non-fill voids were seen to be confused with small particle voids. The image processing schemes developed here were rather straightforward, and it's likely that this can be improved upon with more sophisticated algorithms. If the point at which algorithmic complexity cannot help is reached, the system resolution can always be increased, either by utilizing more sophisticated camera systems or by increasing the magnification of the system.

One area we could have gone deeper into in this chapter was selection of the yield condition. The yield condition was generally found here through trial and error, in a rather ad hoc approach. It was chosen relatively arbitrarily, although the main goal was to provide a demonstration of the effectiveness of using the detection once the yield condition has been defined. In the future, the yield condition needs to be determined based on deeper analysis of empirical observations and simulation work. For instance, acceptable ranges on spectral/color variations and how this relates to corresponding geometric variations can be

determined through simulation of a neighborhood of geometries in the vicinity of the desired geometry.

Chapter 5: Optical Critical Dimension Scatterometry with Hyperspectral Imaging

In the previous chapter, we showed how image processing techniques can be applied to spectral imaging data to detect and classify defects in LNAs. This technique is very useful for identifying large, macro-scale patterning defects as well as nanoscale geometric variations. It is amazing that nanoscale variations can be classified from macroscopic optical differences and in general, just based on color variations, transmittance variations, etc., the identification can go as far as to say what *types* of geometric variations have occurred i.e. diameter increase, linewidth under-target, presence of etch depth variations, etc. However, the image processing approach by itself cannot precisely quantify the geometric variations that have occurred, and many times, this information is highly desirable.

In order to do this, an inverse modelling approach which relates the spectral imaging data to feature geometry must be created. Such an inverse model can be constructed for any type of spectral imaging data (broadband, color, multi-spectral, hyperspectral) depending on the physics behind the specific LNA in question and its interactions with light. However, this kind of inverse modelling has traditionally been done using hyperspectral data with a technique called optical critical dimension (OCD) scatterometry. This method, also known as spectroscopic, or ellipsometric, scatterometry [32], makes use of the fact that the spectra are highly sensitive to feature geometry.

Figure 39 shows how different geometries of hourglass-shaped nanopillars, for instance, create very different reflectance spectra and colors. The difference in average

pillar diameter between the blue/purple and orange arrays is only ~40 nm, but the difference clearly has a profound effect on both the color and spectra exhibited by the arrays.

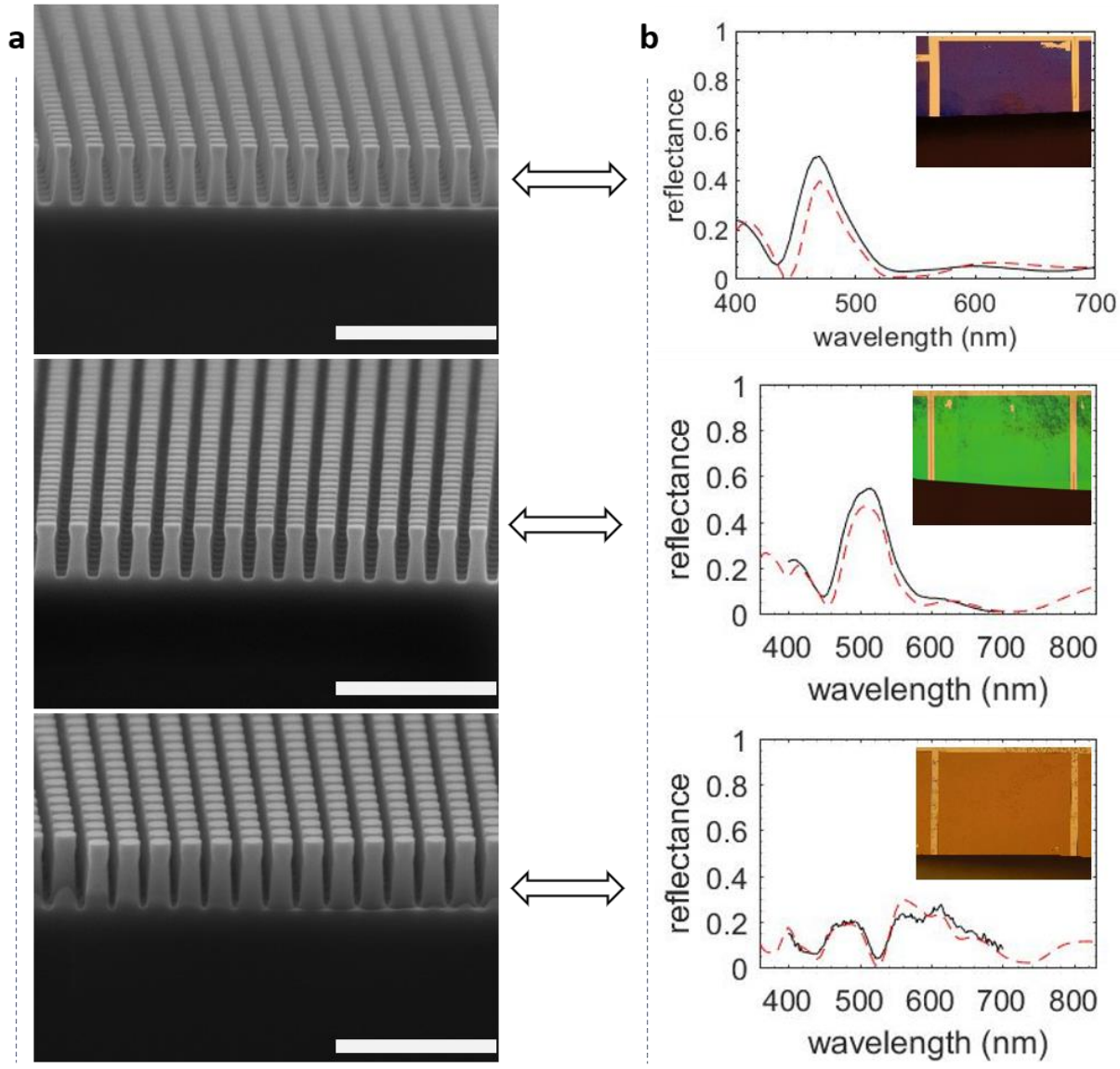

Figure 39. Hourglass nanopillar geometry vs color and spectra. (a) cross-section SEM images of various hourglass nanopillar arrays (scale bars = 1 μm). (b) reflectance spectra and color exhibited by the various arrays in (a) (correspondence by row). The spectra plots each contain the experimentally measured reflectance (black line) and simulated reflectance (dashed red line). In the top right of each spectra plot is a microscope image of the sample showing the color exhibited by the sample. The squares are 1 x 1 mm.

The first step in developing an OCD model is to develop a forward model for a given LNA using one of many available electromagnetic simulation methods such as finite element modelling (FEM), finite difference time domain (FDTD), or rigorous coupled wave analysis (RCWA). In this work, we utilize FDTD. Once the forward model is developed and validated, a large number of simulations can be run for a range of geometries building a so-called "library" of simulated spectra for various feature geometries. Experimental spectra from samples can then be compared against the library (usually with a fitting parameter such as root-mean-square-error) to find the simulated spectrum which matches best. The geometric parameters used for that simulation are then assumed to exist in the region of the sample having generated that experimental spectrum. This procedure is illustrated in Figure 40.

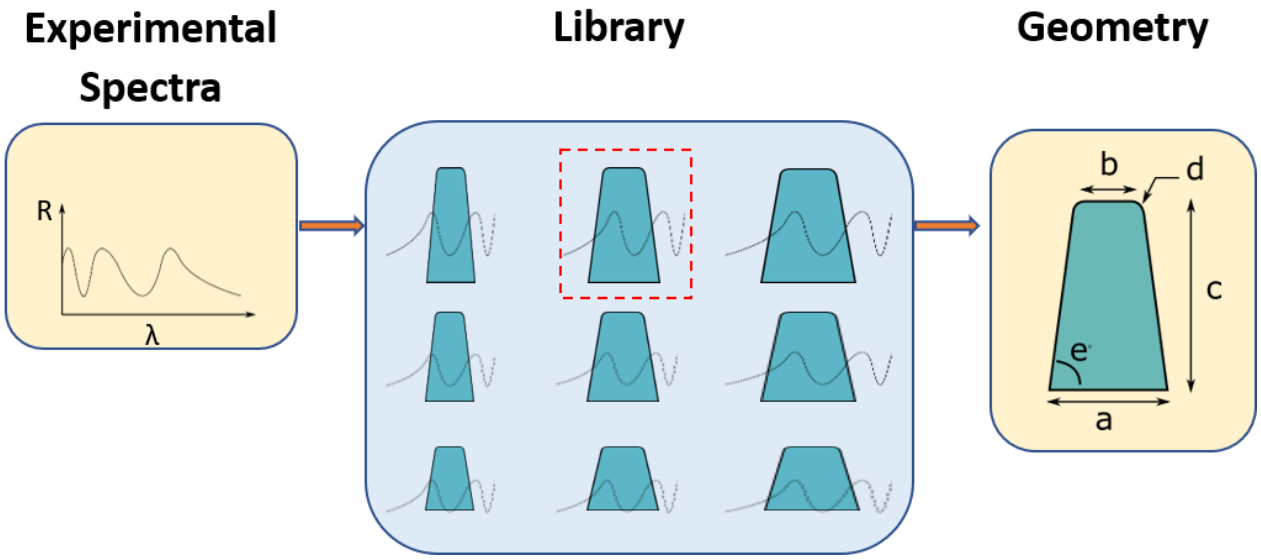

Figure 40. Schematic of OCD enabled by the inverse modelling procedure.

OCD modelling has been applied for decades, particularly in the semiconductor industry, but only a small amount of literature exists on augmenting the technique with imaging methods [49]. Naturally however, extending the technique to imaging is highly valuable in that there is a potential to dramatically increase the throughput with the highly parallel nature of image sensors. Where traditional OCD has been done with point to point measurement systems, which measure a single area at a time, hyperspectral imaging can measure millions of points simultaneously, allowing for OCD modelling on full wafer and large area webs created using R2R nanofabrication processes.

To demonstrate this, we use our hyperspectral imaging system to perform OCD modelling for nanopillar arrays. In order to make this demonstration computationally tractable, we do these demonstrations using some of the simplest structures available to us. This is mainly because the library generation procedure involves computation on the order of 10^n individual simulations, where n is the number of geometric parameters used to describe a structure. A single FDTD forward simulation of an hourglass nanopillar for the 400-700 nm wavelength range typically takes ~5-10 seconds on the computer available for this project, so reducing feature complexity for this demonstration is paramount.

In order to demonstrate OCD for nanopillar arrays, we have fabricated arrays of truncated cone shaped pillars using plasma etching. This is essentially the simplest shape achievable with plasma etching since most etch processes naturally impart a non-vertical sidewall to the features. The truncated cone structure can be seen in the cross-section SEM images in Figure 41(a). This structure can be described fairly effectively with three of the parameters shown in Figure 41b: Top diameter (D), height (H), and sidewall angle (θ). In

actuality, the structure appears to be slightly more complex due to the varying sidewall angle seen in the SEM images, but we wish to keep the model as simple as possible for the reasons discussed. For forward model validation, an additional fourth parameter (N.O.) is added based on the observation that simulated spectra based on cross-section SEM measurements of the dimensions D, H, and θ yield spectra that are consistently red-shifted (see Figure 41c) from the experimental spectra as measured by the spectral imaging system. This same phenomenon occurred in our previous work related to the hourglass-shaped nanopillars [8] so the red-shift was no surprise to us. Based on our previous experience, we understood that the red-shift was due to the presence of a low index layer comprised of native oxide and/or surface roughness caused by etch damage on the outside of the pillars creating a core-shell structure. The core/shell structure is not directly observable in the SEM, and only the *total* diameter can be measured. Thus, the measured diameter is misleading. To account for this, we add a native oxide layer to the simulation, which effectively subtracts from the measured SEM diameter. A native oxide thickness of 5 nm is found to produce a good match between simulation and experimental spectra on the sample shown in Figure 41(a) based on the two points (1 and 2). The experimental and modelled spectra are shown in Figure 41(d) for the two points.

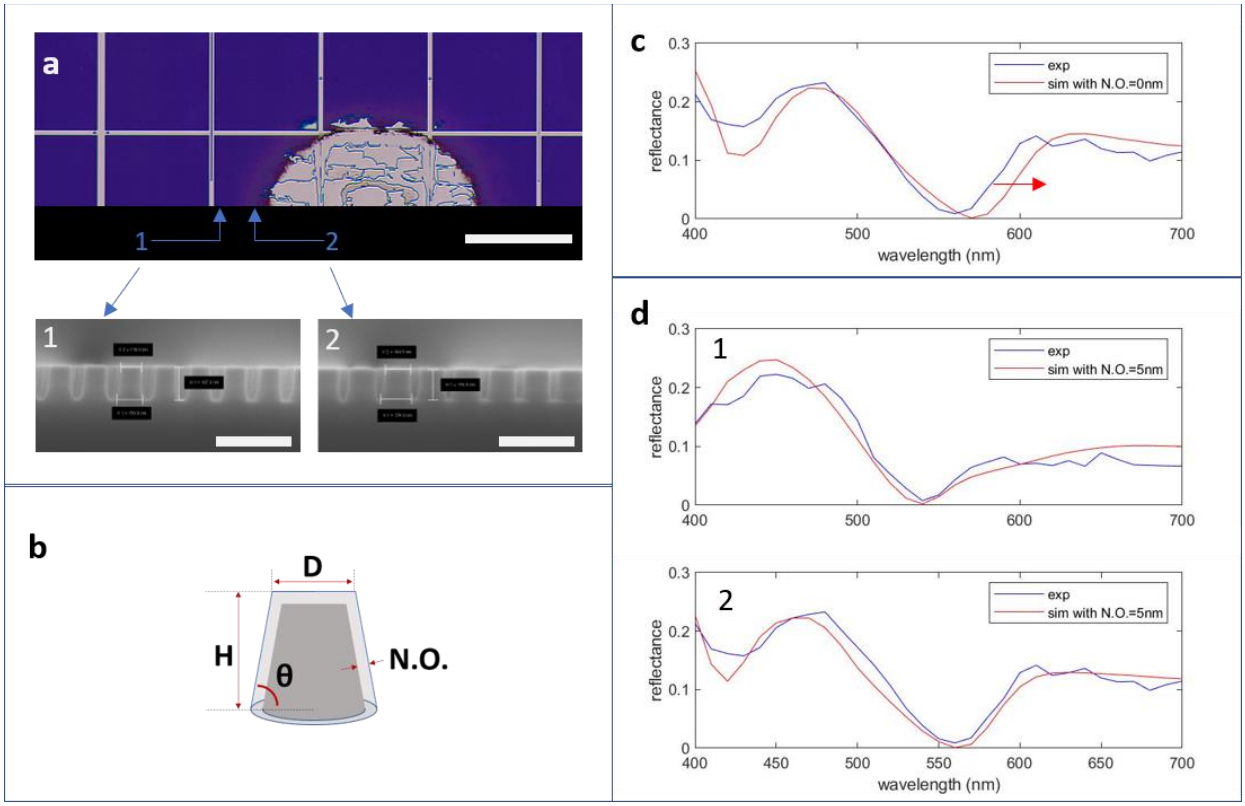

Figure 41. Truncated cone forward model and validation. (a) RGB image of a truncated cone array sample showing where two points "1" and "2" were measured by cross-section SEM (scale bar for RGB image = 1 mm) (scale bar for SEMs = 400 nm). Note that the photo is not of the cleaved sample itself but is just cropped to show where the cleave was. (b) Schematic of the truncated cone model showing the various geometric parameters. (c) Plot of spectra showing how the simulated spectra based on the SEM measurements are red-shifted from the experimental spectra. (d) Plots of spectra taken at the points "1" and "2" from (a) showing good match between experimental spectra and simulated spectra based on the SEM measurements with a native oxide thickness of 5 nm.

With the forward model working, we then generate the library of simulated spectra. In order to keep the library size manageable, the model is simplified by removing the low index layer from the simulation. This removes the ability to determine the thickness of the low index shell but remains effective for determining the dimensions of the Si core of the

structure. The Si core dominates the light interaction, such that for a given Si core geometry, adding a low index layer on top of it has little effect. Our library is generated based on the following parameter ranges: D: 100-190 nm in steps of 3 nm, H: 150-230 nm in steps of 5 nm, and θ: 80-89^{o} in steps of 1^{o} resulting in a library of size 5270.

The library search procedure is carried out by minimizing the root-mean-square-error (RMSE) between each experimentally measured spectrum (each hyperspectral image pixel) and all spectra in the library. The search is applied to the full sample shown in Figure 41(a) (before it was cleaved) and the results of the OCD metrology are shown in Figure 42. The colormaps show some interesting results. In the diameter colormap, we see that the diameter increases significantly as the pattern edges are approached. This diameter increase occurs because of increased RLT near the edges of the pattern, causing feature diameter to be smaller everywhere else. As expected, we also see this diameter increase around the perimeter of the particle exclusion zones, in particular, the one in the upper right of the sample.

Interestingly, we also observe that the sidewall angle seems to increase in tandem with the top diameter near the edges of the patterned area and the edges of the particle zones. We theorize that this could be a natural characteristic of the plasma etch process to etch straighter sidewalls for larger features. In some instances, near the top of the pattern, the height appears to increase in tandem with the diameter as well, which is unexpected behavior, although in most areas of the sample the height seems uncorrelated with the diameter variations. This is expected, since diameter variations usually occur due to lithographic issues like RLT variations, which don't affect etch depth except for in the case

of etch delay, but this sample does not appear to have experienced much etch delay except for at the edge of the particle zones. From the RGB image it is clear that the black etch delay line exists entirely outside of the pattern, whereas in the wine glass wafer (see Figure 25) this black line intersects the edges pattern almost everywhere. The reason for the height variations across the sample is unclear, because, for the most part, they don't appear to follow any recognizable signatures. This could be the result of relatively unpredictable variations in etch rate across the sample.

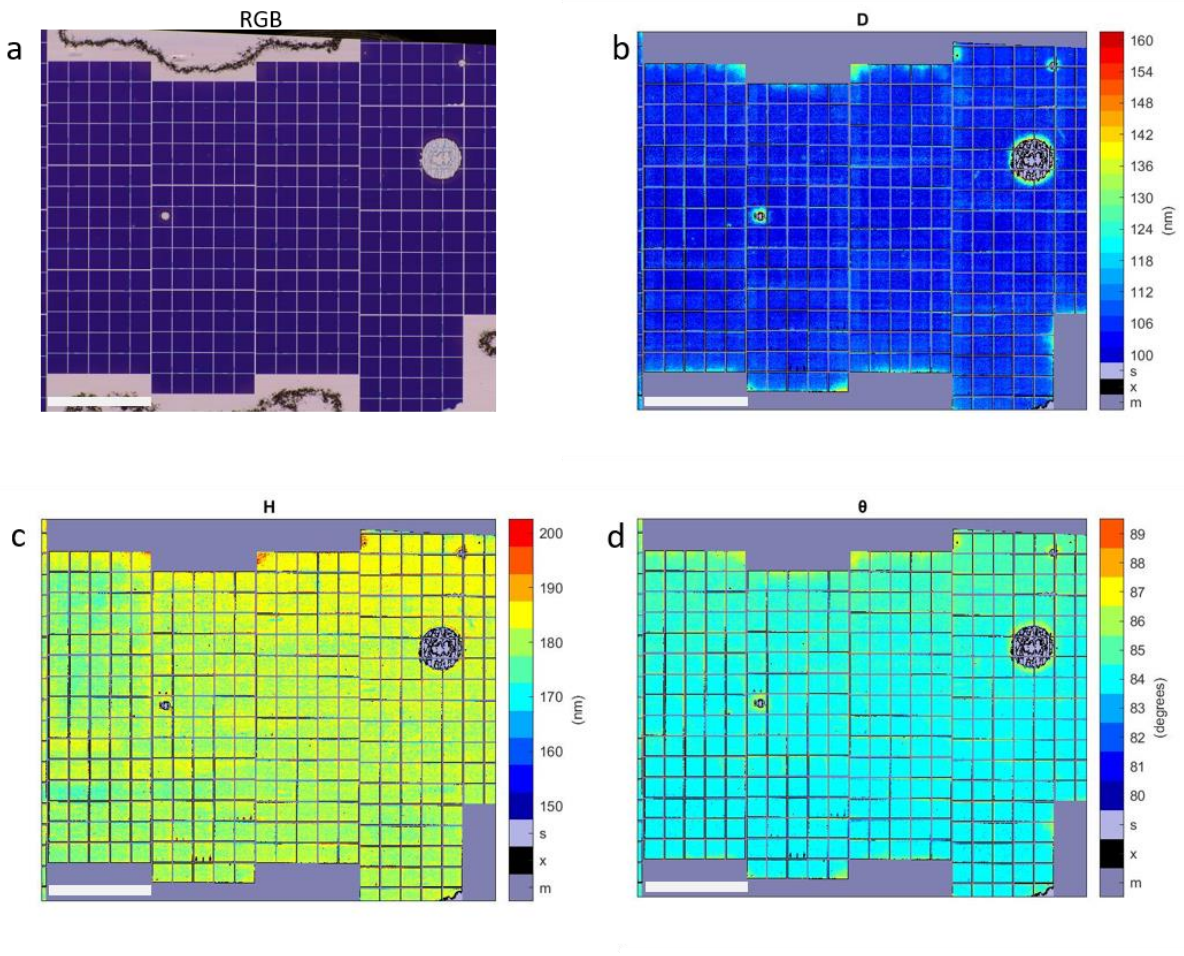

Figure 42. Scatterometry results for full wafer of truncated cone arrays. (a) RGB image of a full wafer of truncated cone arrays. (b) Colormap of OCD measured top diameter (scale bar = 5 mm). (c) Colormap of OCD measured height (scale bar = 5 mm). (d) Colormap of OCD measured sidewall angle (θ) (scale bar = 5 mm). Each of the colormaps has 3 colors dedicated to results that belong to areas that were masked out of the analysis ("m"), areas that did not produce an acceptable match ("x"), and areas that were determined to be bare Si ("s").

To provide further validation for the OCD results, we return to the cleaved portion of the sample (see Figure 43(a)) and take more cross-section SEM measurements near the edge of the particle exclusion zone. For this experiment, we take SEM measurements starting at the left edge of the square to the left of the zone and proceed in 50 μm increments

towards the right, approaching the particle exclusion zone. In total, 11 measurements were taken for a distance of 500 µm covering the area shown by the yellow bracket in Figure 43(b). A comparison of the SEM measurements and the OCD results are shown in Figure 43(c).

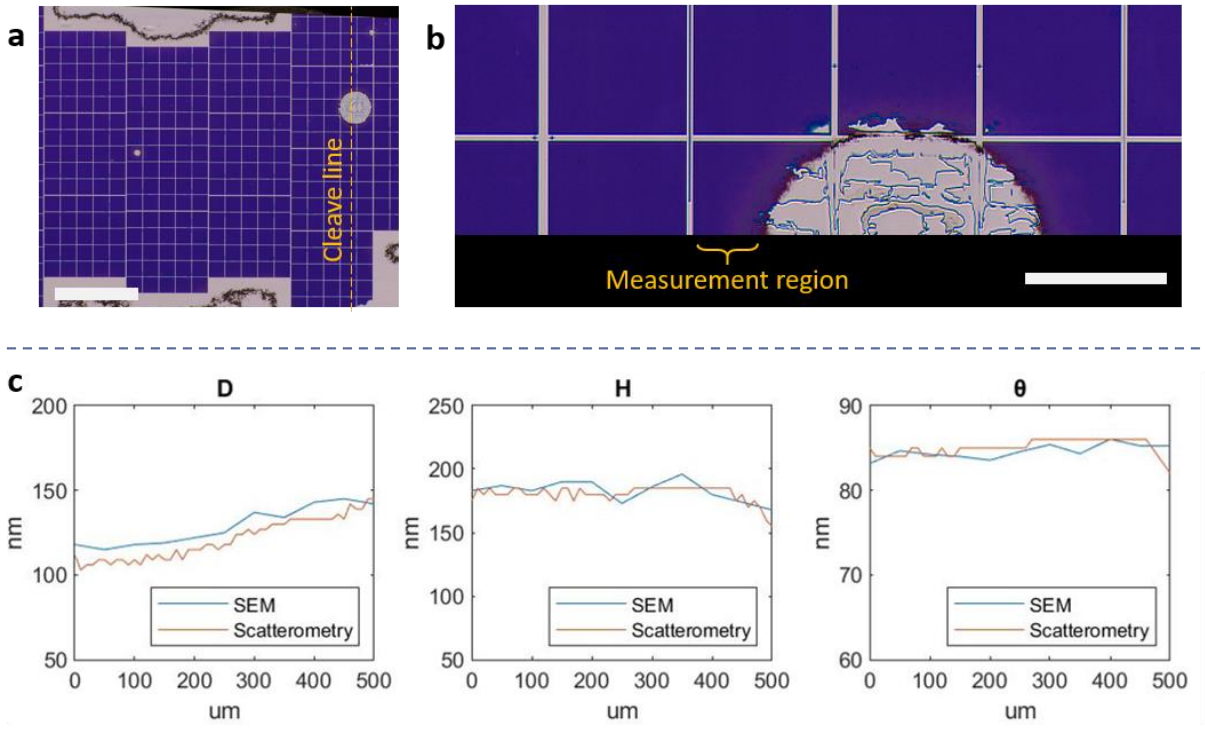

Figure 43. Comparison of OCD to SEM results. (a) RGB image of truncated cone array sample showing the line at which it was cleaved for cross-section SEM (scale bar = 5 mm). (b) RGB image showing the cleaved portion of the sample and the measurement region dictated by the yellow bracket for cross-section SEM measurements which were taken along the edge (scale bar = 1 mm). Note that the photo is not of the cleaved sample itself but is just cropped to show where the cleave was. (c) Plots comparing the results of the cross-section SEM measurements and OCD measurements for the three geometric parameters D, H, and θ.

At the edge of the particle exclusion zone, the diameters of both the SEM and OCD measurements increase in tandem as the zone is approached. The SEM diameter is slightly

larger than the OCD value at all points. The difference between the two datasets is ~10 nm in diameter which corresponds to the native oxide of 5 nm (radius) that produces a good match to the experimental spectra demonstrating that the 5 nm native oxide assumption works well across a range of D values. The height and sidewall angle values are very similar between SEM and OCD. Unlike the diameter, the height should be the same for SEM and OCD, because the low index layer should exist equally on the trench floor between the features and on the tops of the features leaving the magnitude of the SEM height measurement unaffected. The sidewall angle measurements should also be unaffected by the low index layer. Interestingly, both systems measure a slight increase in the sidewall angle as the particle zone is approached. Again, it's possible that the etch naturally produces a directly proportional relationship between diameter and sidewall angle, at least for this range of diameter values.

A higher magnification spectral image was taken of another sample and OCD was run producing the colormaps shown in Figure 44. Here, the pixel size is about 1 x 1 μm. The most interesting aspect of this result is the emergence of the e-beam write pattern signature that we discussed in Chapter 3. It is known that feature size variations can occur over the e-beam "write field", causing CD variations, in this case diameter variations, and naturally the height should be left unaffected. Indeed, the signature seems to be isolated to the diameter parameter. The height does appear to vary, but when given close inspection, it does not appear to follow the same signature.

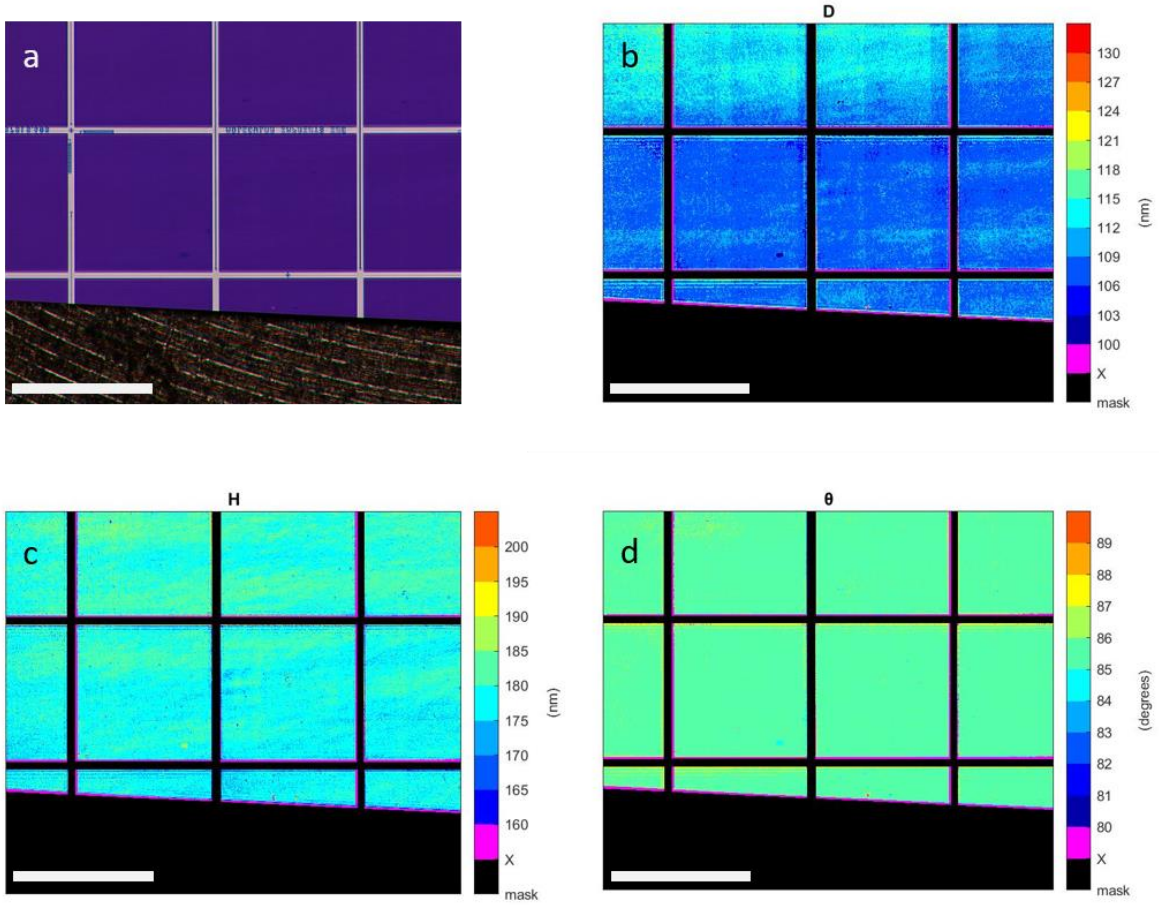

Figure 44. OCD Results for a sample containing truncated cone arrays at high magnification. A) RGB image of a sample of truncated cone arrays taken with a 3X magnification hyperspectral imaging system. B) Colormap of OCD measured diameter (scale bar = 1 mm). C) Colormap of OCD measured height (scale bar = 1 mm). D) Colormap of OCD measured sidewall angle (scale bar = 1 mm). Each of color bar has 2 colors dedicated to results that belong to areas that were masked out of the analysis ("mask") and areas that did not produce an acceptable match ("x"). The sample is cut off at the bottom at an angle due to the way it was cleaved.

The results of the OCD modelling show the power of hyperspectral imaging as a geometric metrology method for nanopillar arrays. The results revealed defects that would be impractical to identify using small field of view methods such as SEM. The e-beam

write field signature, for instance, would require probably thousands of individual CD-SEM measurements to be stitched together. Just the time it takes to pump down an SEM to vacuum would bottleneck the manufacturing line let alone the measurement time.

Naturally however, this approach has all of the usual limitations of OCD modelling. For instance, the accuracy of the geometric determination is only as good as the forward model being used. In this case, a simplified 3-parameter model was used to limit the computational complexity, but the actual truncated cone structure appears to have at least 5 geometric parameters. This inherently means that the results are inaccurate to some extent, although the accuracy ultimately depends on the requirements of the manufacturing tolerances, and this was simply meant to be a demonstration. Also, in OCD modelling there is an assumption of uniformity within local groups of pillars existing within a single pixel area that may not in fact exist. In fact, the results contain a significant number of "no match" values, particularly at the edges of particle voids where there exists partial breakthrough caused by extreme etch delay. In these areas there is not a uniform array, but rather something that might resemble what is seen in Figure 21(c) in Chapter 3. Also, immature processes like MACE can produce significant etch depth variations over just a few periods of the array which we have observed to compromise the OCD modelling procedure. Non-uniform arrays can technically be captured by increasing the complexity of the OCD forward model, but the potential complexity of such a model would increase computational expense dramatically.

It's possible that OCD metrology can be done with multispectral and even RGB as well. Back when we first began fabricating the hourglass arrays, for instance, we would use the color frequently to make assumptions about what geometry had been fabricated on a particular wafer, and this was reasonably effective. Formalization of the approach can be done by transforming the library of spectra to a library of RGB color values using the CIE transformation discussed in Chapter 2. The main issue here is that different geometries, which might produce unique spectra could produce the same RGB color values, and thus the library would have ambiguity which is quite undesirable. However, it's possible that even in the case when multiple matches are found, context clues such as neighboring geometries could be used to uniquely specify the geometry.[2]

This chapter includes significant discussion of hourglass shaped Si nanopillar arrays which were discussed extensively in our publication Gawlik et. al [8]. In this work Gawlik conceived the idea, did most of the experimental and simulation work, and wrote most of the paper. Cossio and Kwon did most of the work in the sections regarding the angular dependence. Kwon also ran simulations to further angular dependence discussion in the appendix. Jurado and Palacios helped with fabrication of samples. Singhal offered help and guidance as well as editing help. Alu, Yu, and Sreenivasan helped with mentorship, editing, and direction.

Chapter 6: Spectral Imaging Metrology for Roll-to-Roll Manufacturing of Large Area Nanostructure Arrays

So far, we have discussed spectral imaging metrology for wafer scale manufacturing of LNAs. While this is relevant for many LNAs – those based on Si, in particular – LNAs will also be manufactured on roll-to-roll (R2R) nano-manufacturing systems in the near future. R2R nano-manufacturing is attractive, in general, because it allows for very high throughput fabrication on inexpensive, flexible substrates such as polycarbonate and metal foil. R2R manufacturing seems particularly viable for manufacturing of display components based on LNAs such as MMGs (metal mesh grids) and WGPs (wire grid polarizers). In anticipation of this new market, we have collaborated with Emerson & Renwick (U.K.) to design R2R nano-manufacturing solutions. Amongst these solutions is metrology, and thus we have designed a spectral imaging metrology system for R2R.

The system we have designed is shown in Figure 45. The system includes a white LED light source, various linescan cameras, and other optical components like mirrors and beamsplitters which are mounted onto a frame. In the middle of the frame there is a slot for the web to thread through. As the web rolls through, the linescan cameras image the web line by line, such that a continuous 2-dimensional image is formed from the linear web movement. The web speed must be tracked precisely in order to trigger the camera line acquisitions synchronously with the web motion. This can be achieved, for instance, by placing a rotary encoder on one of the rollers in the web roller system, ideally an idler roller. There are four linescan cameras in total which are responsible for different

measurements. The first camera above the web, for instance, is responsible for taking measurements of light reflected off of the web. The two cameras below the web slot are responsible for measurements of light transmitted through the web. There are two transmittance cameras so that multiple transmission metrics such as multiple polarization states can be measured simultaneously. Finally, the fourth camera, the source monitor, images the beam directly from the illumination source which can be used as a reference measurement. The system is to be mounted onto a sliding rail, such that it can moved back and forth width-wise along the web with a linear stage. This is necessary, because the system FOV is smaller than a typical web width (300+ mm).

The spectral imaging system is being designed alongside a scanning 2-theta scatterometry system being designed at University of New Mexico [50]. The two systems will exist on the same rail system which allows both systems to access different parts of the web. The 2-theta scatterometry system will not be discussed here, but the design includes a footprint for the system which is necessary to show because the overall frame for the combined system contributes to the structural stability of the spectral imaging system.

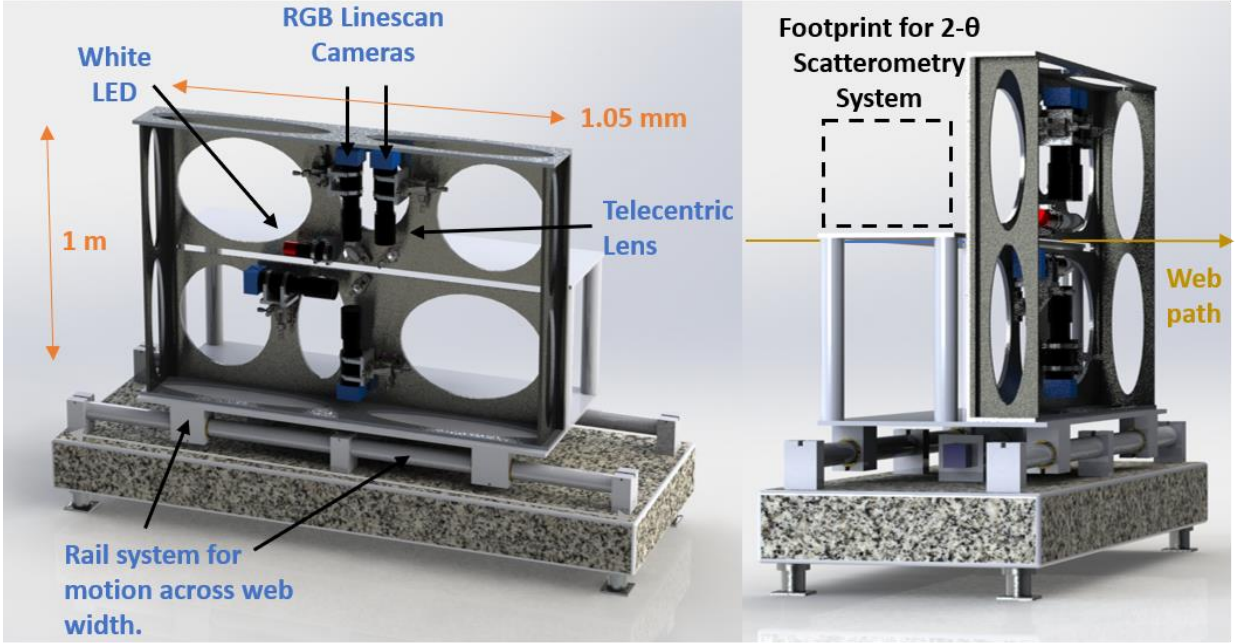

Figure 45. R2R optical metrology system being designed in collaboration with Emerson and Renwick including the spectral imaging system being discussed in this section as well as a 2-theta scatterometry system being developed at University of New Mexico.

The system specifications are shown in Table 5. The system will use a white light source and RGB linescan cameras. RGB is chosen over hyperspectral for this system, because the main LNAs this system will characterize, WGPs and MMGs, are not particularly sensitive to spectral effects, yet will be used in RGB display devices, so the RGB measurement provides good quality control. We have chosen to use Teledyne DALSA Piranha 4K trilinear linescan cameras (#P4-CC-04K07T-00-R) along with a 2X magnification telecentric lens from Sill Optics (#P4-CC-04K07T-00-R). This sensor/lens combination gives us a FOV of 21.65 mm and a pixel on web size of ~6 um. Based on research we conducted on modern smart phone resolution, the most likely end application for WGPs and MMGs, we determined that the pixel on web size should be at least 2 times

less than a cutting-edge smart phone pixel size in order to be able to spatially resolve individual pixels, and thus provide the ability to inspect individual pixels for yield. The LG G4 smart phone, for instance, has a screen resolution of 538 PPI (pixel per inch) which corresponds to a pixel size of 47.2 um. Human retinal resolution, on the other hand, is only 477 PPI at a viewing distance of 12 inches [51,52]. Regardless, most modern smart phones generally fall around 50 um pixel size. A pixel on web size of 6 um gives a comfortable margin for resolving individual pixel sized areas and also leaves room for higher PPI applications such as near eye display components in the future.

The depth of field (DoF) of the telecentric lens puts constraints on how much web displacement can be tolerated in the z-direction due to web wobbling, slight non-circularity of the web rollers (eccentricity), etc., before the image is significantly blurred. The DoF value for the Sill Optics lens is 0.2 mm, so the web displacement ideally should be kept less than ± 100 μm.

Also listed in the table is a specification for ratiometric resolution, which is the system's ability to discern between different values of ratiometric quantities like transmittance and reflectance. The DALSA cameras have the ability to take images in 8-bit, 10-bit, or 12-bit which at best produce the ratiometric resolutions shown in the table. The best resolution is calculated based on calculating the percentage difference between the highest value for a given bit depth (2^n) and the second highest value for that bit depth (2^n-1) where n is the bit depth.

A specification for linescan camera line rate range is shown in the table as well to be 1-1412 Hz. This range is based on the web speed range given to us by Emerson and

Renwick. Finally, the scatter angle range is 0.5-7^{o} half angle. This is based on the numerical aperture (NA) of the Sill Optics lens.

Table 5. R2R Spectral Imaging System Specifications.

Light Source	White light (LED)	
Camera Type	RGB (trilinear)	
Pixel Size on Web	~6 µm	*based on requirements of human spatial resolution and modern smartphone PPI
Field of View (FOV)	21.65 mm x 6 um	
# camera pixels, Lens Mag	4096, 2X	
Depth of Field (DoF)	0.2 mm	*based on telecentric lens specs for 2X magnification
Best Ratiometric Resolution	0.391% (8 bit camera) 0.098% (10 bit camera) 0.024% (12 bit camera)	
Line Rate	1 - 1412 Hz	*based on web speed range and line width
Scatter Angle Range (half angle)	0.5-7^{o}	*for pseudo haze measurements (see text)

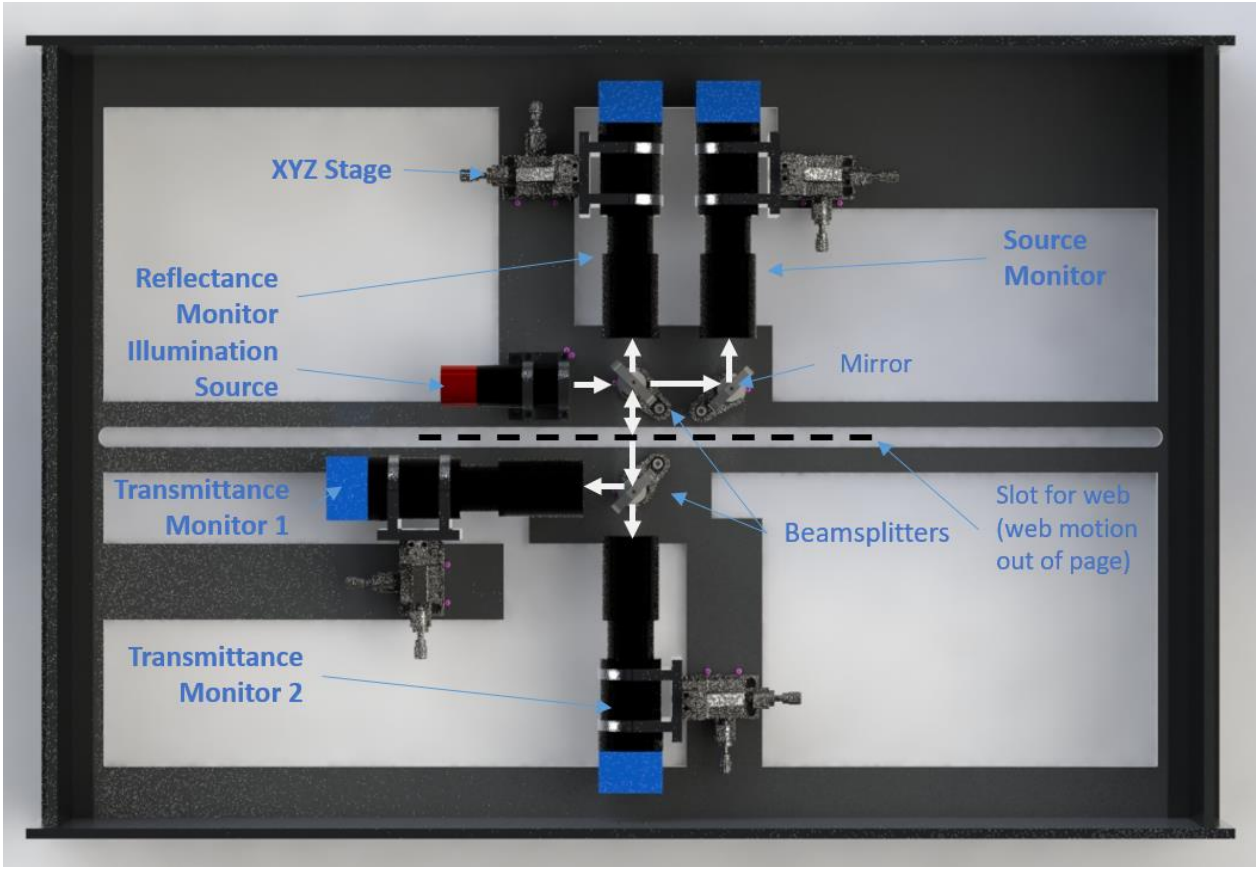

Figure 46. R2R spectral imaging system components. The beam path is shown by the white arrows.

The primary difference between this design and the design of our wafer scale spectral imaging system is the fact that it uses linescan cameras. R2R manufacturing is inherently very different from wafer scale manufacturing, because the manufacturing is done on long, continuously moving web-like substrates rather than discrete, motionless substrates like wafers. This inherently makes the manufacturing more continuous, rather than stop and start as in traditional wafer processing. This difference in manufacturing style demands serious overhauls of both fabrication technologies (i.e. lithography, etch, film deposition) as well as metrology systems. In our case, the wafer scale spectral imaging tool

can't be applied to R2R metrology in its current form. Since the samples are now moving constantly, the amount of time the camera has to do its acquisition is heavily constrained, which makes it difficult to do a large number of sequential acquisitions at different spectral bands as we have done before.

Our solution to this problem embraces linescan style imaging which can image a sample at multiple spectral bands simultaneously. Traditional area cameras can do this as well, but imaging multiple spectral bands with an area sensor inherently results in a loss of resolution, because individual pixels must be divided up between the spectral bands as its shown in Figure 47. In linescan imaging, only one line of the sample is imaged at a time, so multiple rows on a linescan sensor can be utilized to measure different spectral bands with no inherent resolution loss.

This principle can even be extended to hyperspectral imaging. Hyperspectral solutions exist for linescan cameras in one of two forms: 1. The "push broom" style and 2. Linear variable filters. Push broom style hyperspectral cameras are essentially an extension of the traditional monochromator technology, such as what is used in the tunable light source in our wafer scale hyperspectral imaging system. The monochromator inherently accepts light in through a slit, and then splits the light into a linear band of different wavelengths using a diffraction grating. If the light input to the monochromator is a line image from a sample, the line image can be split into spectral bands across an area sensor in which each row of the sensor then corresponds to a particular spectral band. Linear variable filters, on the other hand, achieve hyperspectral line imaging by covering an area sensor with a linearly varying color filter. The color filter itself can be based on a variety

of technologies including dyes and variable thickness etalons [53,54] which are pictured in Figure 47.

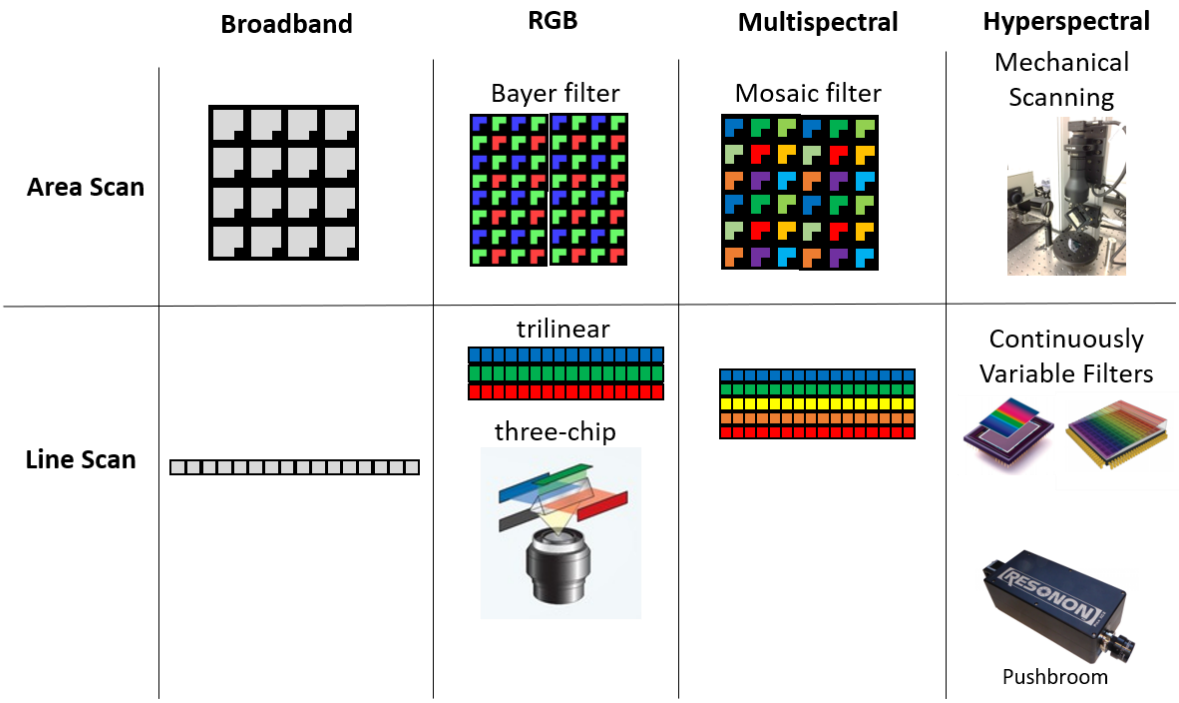

Figure 47. Area vs line scan sensors for broadband, RGB, multispectral, and hyperspectral imaging. Image sources: Continuously variable filters [53,54], push broom [55].

The two independent transmittance monitors allow for simultaneous measurement of two different transmittance states. This is useful for both WGPs and MMGs. For WGPs, this will be utilized to measured different polarization states simultaneously. Polarizers can be placed in front of the two cameras in different alignments such that the cameras will measure light at different polarizations. Similarly, for MMGs, "pseudo-haze" and transmittance can be measured simultaneously. Haze, as defined according to the ASME standard (D4039), is impossible to measure in an imaging fashion. The ASME standard

approach utilizes an integrating sphere which is effective at capturing a large range of scattering angles, but inherently destroys spatial information that is necessary for imaging. However, by increasing the numerical aperture of the telecentric lens, a larger range of ray angles from the sample can be measured, which will be effective for measuring scattered light into small/medium angles. This system allows for a maximum angular collection half angle of 7^{o}. It's yet to be determine how effective this pseudo-haze measurement will be, but the thinking is that most scattered light is scattered into small angles. This is the case for Lambertian type reflectors and the MMG is expected to act more like a specular surface. Modeling will undoubtedly provide useful for understanding the relationship between small/medium angle scatter and large angle scatter, both of which contribute to the overall haze.

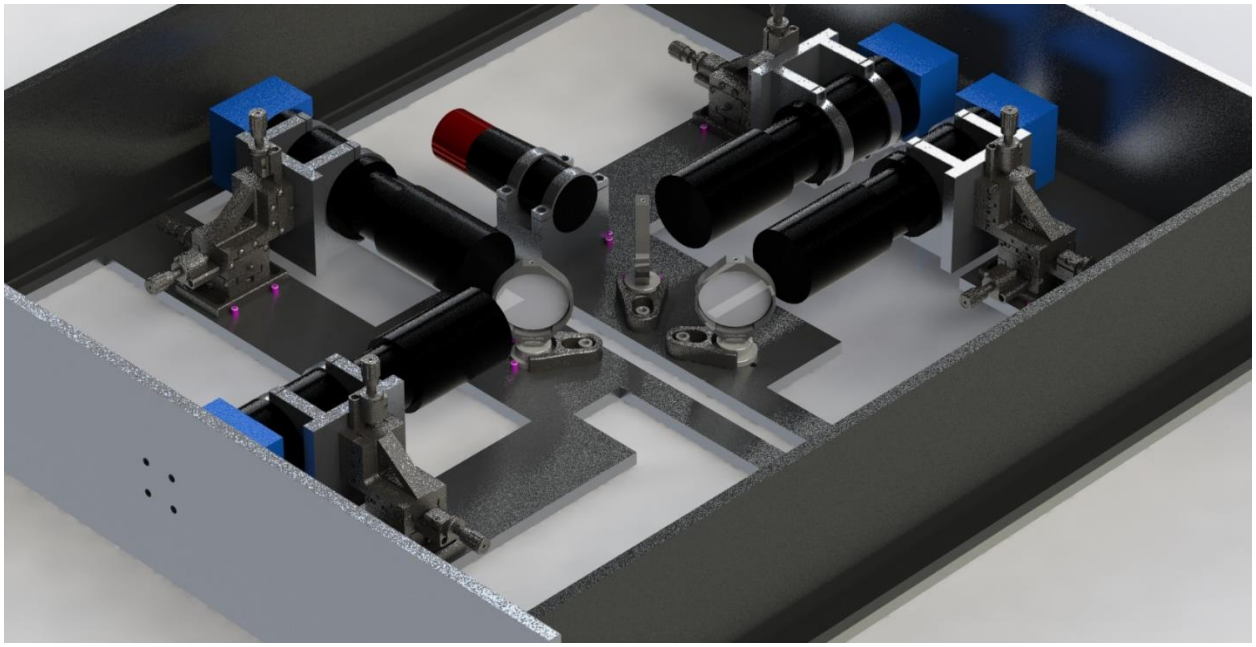

Figure 48. Closeup of R2R spectral imaging system.

Construction of this R2R spectral imaging system is to begin soon after the time of writing this dissertation. In parallel, also in collaboration with Emerson & Renwick, will be ongoing development of fabrication processes for WGPs and MMGs on R2R using R2R nanoimprint, film growth, and etch systems. The metrology will undoubtedly provide great insight into fabrication problems as the process development phase is carried out, and also into the manufacturing phase in which actual devices are being made.

Conclusions and Future Work

In Chapter 1, we provided an introduction to large area nanostructure arrays (LNAs) and motivated the need for high throughput metrology systems to aid in LNA manufacturing. We showed that LNAs exhibit unique optical properties, such as structural coloration and polarization contrast, and that for this reason spectral imaging can provide an insightful characterization for LNAs, including defect detection as well as geometric measurement. Spectral imaging, which includes RGB color imaging, multi-spectral imaging, and hyperspectral imaging, is naturally a very high throughput metrology compared to traditional nanometrology approaches like scanning electronic microscopy (SEM) as well as traditional scatterometry approaches. This is because imaging methods are inherently highly parallel, have relatively large field of view (FOV), and have high spatial resolution. Thus, spectral imaging makes for an attractive solution for LNA manufacturing.

In Chapter 2, we discussed the general design principles behind spectral imaging systems and discussed the specific design of a wafer scale hyperspectral imaging system which was used throughout this dissertation to provide large area characterization of a variety of LNA samples. We discussed aspects of system design such as resolution, field of view (FOV), and telecentricity, and also discussed how system raw data is processed. We also delved into throughput considerations and showed that, if optimized, the wafer scale hyperspectral system can achieve throughput of around 2.6 m^2/hr with 61 spectral bands. If the measurement can be done with a single acquisition, as would be the case with

a monochromatic measurement, broadband measurement, or RGB measurement, the throughput can be as high as 15.3 m^2/hr.

In Chapter 3, we provided background on an exemplar manufacturing process that was used to fabricate a variety of LNA samples discussed in this dissertation. This exemplar process utilizes JFIL nanoimprint lithography as well as etching techniques like plasma etching and metal assisted chemical etching (MACE). We delved into these manufacturing processes and detailed how various defect modes can occur, also showing the result of these defects and discussing how the optical signature of LNAs change in the presence of these defects. This provided necessary understanding for the work we did in Chapter 4.

In Chapter 4, we demonstrated how spectral imaging can be used to perform defect detection and classification in LNAs. It was demonstrated how excursions from expected optical behavior of an LNA can signal the presence of defects. It was shown how defects can be detected with a variety of spectral imaging technologies such as RGB imaging as well as hyperspectral imaging. In both cases, a yield condition is defined based on the expected RGB or spectral properties of the LNAs, and measurements falling outside an acceptable range are considered to be defective. Next, we went further to classify the defects using image processing techniques, namely image segmentation, which were able to differentiate between the unique characteristics of different types of defects. In particular, this was applied to detect and classify imprint particle void defects as well as a handful of edge-related defects including edge etch delay, etch non-start, and non-filling. The defect detection and classification processes have the potential to happen very quickly,

especially when the process is to be done using RGB imaging systems because of their inherently high throughput.

In Chapter 5, we demonstrated how spectral imaging can be coupled with optical critical dimension (OCD) scatterometry to measure geometry in LNAs. The OCD principle involves creation of a large library of simulated spectra for a particular LNA and then using the library in an inverse modelling procedure to find best matches with experimental spectra. We demonstrated the OCD procedure using our hyperspectral imaging system on a sample of Si truncated cone arrays. We showed that doing this with hyperspectral imaging can provide geometric measurement over inch-scale areas with small pixel size, in this case 10 x 10 μm as well as a higher resolution result with pixels of ~1 x 1 um. In both cases, the OCD results revealed a variety of interesting defect signatures that would be difficult, or nearly impossible to observe using other metrology approaches. OCD has been thoroughly explored before in the literature, but the extension to the imaging approach that we've presented here is valuable based on its considerable throughput advantage. We suggest that the OCD procedure can potentially be done fast enough to be in-situ, for example in MACE nanowire etching, if the inverse model is based on RGB values instead of spectra, although we point out that this would likely introduce limitations.

Finally, in Chapter 6, we detailed a design for a roll-to-roll (R2R) spectral imaging system. This system, which is built with a continuously moving web substrate in mind, utilizes RGB linescan cameras. Linescan is great option for the R2R format, because it allows for scaling to simultaneous multi- or hyper-spectral measurements. This is crucial for continuous R2R manufacturing, because the motion of the web greatly reduces the

allowable acquisition time for individual images to be taken, and thus the approach we used in the wafer scale tool, with sequential acquisitions of different spectral bands, was not practical. The system is currently under construction at the time of this dissertation being written, but it is expected that it will be operational soon. The R2R spectral imaging system will primarily target application to R2R wire grid polarizers (WGPs) and metal mesh grids (MMGs). The system is designed to allow for measurement of different polarization states as well as a "pseudo haze" measurement which measures small-to-medium angle scatter for characterization of MMGs.

This dissertation has provided the foundational infrastructure for spectral imaging metrology as applied to LNA manufacturing. Many of the examples presented throughout the dissertation were primarily meant to serve as demonstrations. Wine glass and hourglass shaped nanopillar arrays, for instance, may not be especially applicable to high demand markets. In the future, the spectral imaging metrology that we have developed in this dissertation will likely be applied to other LNAs that have more direct applications in areas such as displays and photovoltaics. MACE nanowires, for instance, have many high impact applications and spectral imaging metrology can be of great aid during the manufacturing process for characterizing yield, identifying defects, measuring geometry, etc. Some demonstrations were provided on MACE nanowire metrology, namely collapse detection, but already, at the time of writing this dissertation, we have begun applying spectral imaging metrology for other tasks within MACE nanowire manufacturing. For instance, OCD metrology seems particularly applicable to MACE nanowire fabrication, because the nanowires that are formed by MACE can actually have a truly cylindrical shape,

simplifying the OCD process tremendously. This is in direct contrast to the truncated cone structures that we were able to produce using plasma etching which have non-vertical sidewalls. The main reason we had not demonstrated OCD for MACE nanowires at the time of this dissertation was because the process had been producing high-spatial-frequency etch depth variations that resulted in significant height differences between groups of wires within individual spectral imaging pixel areas. This was throwing off the inverse modelling procedure. Already however, our MACE process has seen significant improvements in this regard, and it is expected that these local etch depth variations can be eliminated in the near future allowing OCD metrology. We are planning to apply the OCD metrology to wafers post-etch, but also in-situ during the MACE process. It seems likely that an RGB imaging system can conduct effective geometric measurements just based on the color exhibited by the nanowire arrays. This will allow for tracking of etch depth in real time during the actual etching process. Also, the scheme we have developed for collapse detection will be applied here.

Furthermore, the R2R spectral imaging system is set to be constructed in the months following the publication of this dissertation. With this system constructed, R2R spectral imaging can be applied to R2R fabrication of WGPs and MMGs. This system will produce an incredible amount of data on rolls of these devices that are many meters long providing crucial information about defectivity and yield which will undoubtedly aid in the improvement of the fabrication processes used to make these devices. The unique defect modes that will appear in these devices will need to be understood. The R2R manufacturing process is unique, and thus will behave differently than wafer scale fabrication systems,

but nonetheless the defects should be detectable/classifiable using the general approaches that we have developed.

The spectral imaging metrology we have developed is ready to be applied to any LNA manufacturing situation in which the LNA exhibits optical effects that give insight into nanoscale geometry, yield, defectivity, etc. Wherever spectral imaging can be utilized, it should be, because the amount of insight it can provide into the manufacturing process and the throughput at which it can do so are truly unmatched by other metrology approaches.

There are several areas of future research that are outlined next. A detailed study must be done prior to manufacturing to assess the applicability of spectral imaging as a metrology approach for any LNA. The general approach for doing this study would be to run simulations and/or fabricate the LNA and observe the sensitivity of the optical signature (i.e. the color, or spectra) as a function of the various geometric parameters. If the structure exhibits a high enough level of sensitivity, then the spectral imaging approach can be applied. The sensitivity can be quantified by calculating the change in RMSE, for instance, as a function of various parameter changes away from some nominal geometry. The sensitivity of the measurement apparatus can be taken into account and a minimum necessary sensitivity for the LNA's optical behavior can be determined accordingly to be able to detect changes of certain amounts in the various geometric parameters, i.e. 1 nm changes in diameter. Sensitivity alone is not enough, however. The optical signature needs to vary *uniquely* for specific geometric variations, although in the case of multi- and hyper-spectral measurements, which are high-dimensional, this is usually expected. Different

wavelength regimes (i.e. UV, visible, IR) should be looked to understand where optical sensitivity may exist. The visible regime is the most convenient to utilize for spectral imaging, because visible light source and sensor technology is ubiquitous, but if optical sensitivity does not exist in the visible, then other regimes can be looked to. For example, if the pitch and critical dimensions of LNAs go below 100 nm and 50 nm respectively, shorter wavelengths in the UV and DUV regimes may be needed.

Most of the work in this dissertation dealt with Si LNAs, but spectral imaging metrology can potentially apply to other materials as well. Spectral imaging metrology may have applicability to resist structures, for instance, despite resist having relatively low index. At small height values (100's of nm), which are common to imprinted and photo resist films, thin film interference effects are predominant. Assuming pitch is also nanoscale, this produces optical signatures that are highly sensitive to geometry, and based on effective medium approximations, it may be possible to recover the geometric parameters of the resist features using the OCD approach.

The general process for bringing up a spectral imaging metrology application may be to first run a sensitivity analysis and asses general applicability. In the case where it is determined to be applicable, a combination of empirical and simulation study can be pursued to understand defectivity in the LNA. A forward model needs to be developed so that the optical behavior can be simulated, and once this is done, a library can be formed for OCD. In the future, more work could be done to determine a systematic approach for validating the forward models that are used to generate libraries for OCD. In order to do this well, the model should be validated against experimentally obtained results over a

range of geometries for a given structure. With our limited number of samples, we did our best to find such an acceptable range by strategically obtaining the experimental results from areas we knew would contain a range of geometries – near certain types of defects, for instance – but ideally a suitable geometric range can be determined and then fabricated, maybe using a combinatorial approach, so that the model validation can be done for many relevant points. The approach for determining an acceptable range for model validation can be determined based on an understanding of the manufacturing process and what kind of geometric variations are expected to be produced by the manufacturing process itself. This can be done, for instance, through process constraints such as how pitch limits upper values for critical dimensions, as well as empirical observation of the geometric range naturally produced by the process through SEM measurements.

The defect detection and classification work that was done in this dissertation was not fully automated in the sense that the bounds for the various schemes that we used were selected manually, rather than automatically. The manual selection route was pursued mainly in leu of having a large-scale manufacturing production run and was primarily meant to serve as a demonstration of how the bounds can be applied once selected and to show the high-speed result of doing so. In the case of a manufacturing production run however, the bounds can be selected based off of careful empirical and simulation work to understand the range of acceptable optical signatures based on ranges of acceptable geometric variations. These may be defined by the end product. In WGPs, for instance, simulations can be run to determine the geometric range that produces suitably high

contrast ratios. Alternatively, the bounds can be selected based on statistical process control methods.

References

(1) Sreenivasan, S. V. Nanoimprint Lithography Steppers for Volume Fabrication of Leading-Edge Semiconductor Integrated Circuits. *Microsyst. Nanoeng.* **2017**, *3* (1), 17075. https://doi.org/10.1038/micronano.2017.75.

(2) Ahn, S. H.; Yang, S.; Miller, M.; Ganapathisubramanian, M.; Menezes, M.; Choi, J.; Xu, F.; Resnick, D. J.; Sreenivasan, S. V. High-Performance Wire-Grid Polarizers Using Jet and Flash™ Imprint Lithography. *J. MicroNanolithography MEMS MOEMS* **2013**, *12* (3), 031104. https://doi.org/10.1117/1.JMM.12.3.031104.

(3) Pallares, R. M.; Su, X.; Lim, S. H.; Thanh, N. T. K. Fine-Tuning of Gold Nanorod Dimensions and Plasmonic Properties Using the Hofmeister Effects. *J. Mater. Chem. C* **2016**, *4* (1), 53–61. https://doi.org/10.1039/C5TC02426A.

(4) Catrysse, P. B.; Fan, S. Nanopatterned Metallic Films for Use As Transparent Conductive Electrodes in Optoelectronic Devices. *Nano Lett.* **2010**, *10* (8), 2944–2949. https://doi.org/10.1021/nl1011239.

(5) van de Groep, J.; Spinelli, P.; Polman, A. Transparent Conducting Silver Nanowire Networks. *Nano Lett.* **2012**, *12* (6), 3138–3144. https://doi.org/10.1021/nl301045a.

(6) Proust, J.; Bedu, F.; Gallas, B.; Ozerov, I.; Bonod, N. All-Dielectric Colored Metasurfaces with Silicon Mie Resonators. *ACS Nano* **2016**, *10* (8), 7761–7767. https://doi.org/10.1021/acsnano.6b03207.

(7) Seo, K.; Wober, M.; Steinvurzel, P.; Schonbrun, E.; Dan, Y.; Ellenbogen, T.; Crozier, K. B. Multicolored Vertical Silicon Nanowires. *Nano Lett.* **2011**, *11* (4), 1851–1856. https://doi.org/10.1021/nl200201b.

(8) Gawlik, B. M.; Cossio, G.; Kwon, H.; Jurado, Z.; Palacios, B.; Singhal, S.; Alù, A.; Yu, E. T.; Sreenivasan, S. V. Structural Coloration with Hourglass-Shaped Vertical Silicon Nanopillar Arrays. *Opt. Express* **2018**, *26* (23), 30952. https://doi.org/10.1364/OE.26.030952.

(9) Moitra, P.; Slovick, B. A.; li, W.; Kravchencko, I. I.; Briggs, D. P.; Krishnamurthy, S.; Valentine, J. Large-Scale All-Dielectric Metamaterial Perfect Reflectors. *ACS Photonics* **2015**, *2* (6), 692–698. https://doi.org/10.1021/acsphotonics.5b00148.

(10) Boden, S. A.; Bagnall, D. M. Optimization of Moth-Eye Antireflection Schemes for Silicon Solar Cells. *Prog. Photovolt. Res. Appl.* **2010**, *18* (3), 195–203. https://doi.org/10.1002/pip.951.

(11) Boden, S. A.; Bagnall, D. M. Nanostructured Biomimetic Moth-Eye Arrays in Silicon by Nanoimprint Lithography; Martin-Palma, R. J., Lakhtakia, A., Eds.; San Diego, CA, 2009; p 74010J. https://doi.org/10.1117/12.826201.

(12) Huang, Y.-F.; Chattopadhyay, S.; Jen, Y.-J.; Peng, C.-Y.; Liu, T.-A.; Hsu, Y.-K.; Pan, C.-L.; Lo, H.-C.; Hsu, C.-H.; Chang, Y.-H.; et al. Improved Broadband and Quasi-Omnidirectional Anti-Reflection Properties with Biomimetic Silicon Nanostructures. *Nat. Nanotechnol.* **2007**, *2* (12), 770–774. https://doi.org/10.1038/nnano.2007.389.

(13) Li, X.; Li, P.-C.; Ji, L.; Stender, C.; McPheeters, C.; Tatavarti, S. R.; Sablon, K.; Yu, E. T. Subwavelength Nanostructures Integrated with Polymer-Packaged Iii–v Solar Cells for Omnidirectional, Broad-Spectrum Improvement of Photovoltaic Performance. *Prog. Photovolt. Res. Appl.* **2015**, *23* (10), 1398–1405. https://doi.org/10.1002/pip.2565.

(14) Wang, W.-C.; Lin, C.-W.; Chen, H.-J.; Chang, C.-W.; Huang, J.-J.; Yang, M.-J.; Tjahjono, B.; Huang, J.-J.; Hsu, W.-C.; Chen, M.-J. Surface Passivation of Efficient Nanotextured Black Silicon Solar Cells Using Thermal Atomic Layer Deposition. *ACS Appl. Mater. Interfaces* **2013**, *5* (19), 9752–9759. https://doi.org/10.1021/am402889k.

(15) Na, H.; Endoh, T. A Multi-Pillar Vertical Metal–Oxide–Semiconductor Field-Effect Transistor Type Dynamic Random Access Memory Core Circuit for Sub-1 V Core Voltage Operation without Overdrive Technique. *Jpn. J. Appl. Phys.* **2013**, *52* (4S), 04CE08. https://doi.org/10.7567/JJAP.52.04CE08.

(16) Chung, H.; Kim, H.; Kim, H.; Kim, K.; Kim, S.; Song, K.-W.; Kim, J.; Oh, Y. C.; Hwang, Y.; Hong, H.; et al. Novel $4F^2$ DRAM Cell with Vertical Pillar Transistor(VPT). In *2011 Proceedings of the European Solid-State Device Research Conference (ESSDERC)*; IEEE: Helsinki, Finland, 2011; pp 211–214. https://doi.org/10.1109/ESSDERC.2011.6044197.

(17) Sun, Y.; Yu, H. Y.; Singh, N.; Le, T. T.; Gnani, E.; Baccarani, G.; Leong, K. C.; Lo, G. Q.; Kwong, D. L. Junction-Less Stackable SONOS Memory Realized on Vertical-Si-Nanowire for 3-D Application. In *Proceedings of 2011 International Symposium on VLSI Technology, Systems and Applications*; 2011; pp 1–2. https://doi.org/10.1109/VTSA.2011.5872271.

(18) Park, H. J.; Xu, T.; Lee, J. Y.; Ledbetter, A.; Guo, L. J. Photonic Color Filters Integrated with Organic Solar Cells for Energy Harvesting. *ACS Nano* **2011**, *5* (9), 7055–7060. https://doi.org/10.1021/nn201767e.

(19) Wen, L.; Chen, Q.; Song, S.; Yu, Y.; Jin, L.; Hu, X. Photon Harvesting, Coloring and Polarizing in Photovoltaic Cell Integrated Color Filters: Efficient Energy Routing Strategies for Power-Saving Displays. *Nanotechnology* **2015**, *26* (26), 265203. https://doi.org/10.1088/0957-4484/26/26/265203.

(20) Lee, K.-T.; Lee, J. Y.; Xu, T.; Park, H. J.; Guo, L. J. Colored Dual-Functional Photovoltaic Cells. *J. Opt.* **2016**, *18* (6), 064003. https://doi.org/10.1088/2040-8978/18/6/064003.

(21) Lee, J. Y.; Lee, K.-T.; Seo, S.; Guo, L. J. Decorative Power Generating Panels Creating Angle Insensitive Transmissive Colors. *Sci. Rep.* **2015**, *4* (1), 4192. https://doi.org/10.1038/srep04192.

(22) Dhindsa, N.; Walia, J.; Saini, S. S. A Platform for Colorful Solar Cells with Enhanced Absorption. *Nanotechnology* **2016**, *27* (49), 495203. https://doi.org/10.1088/0957-4484/27/49/495203.

(23) Cao, A.; Sudhölter, E.; de Smet, L. Silicon Nanowire-Based Devices for Gas-Phase Sensing. *Sensors* **2013**, *14* (1), 245–271. https://doi.org/10.3390/s140100245.

(24) Field, C. R.; In, H. J.; Begue, N. J.; Pehrsson, P. E. Vapor Detection Performance of Vertically Aligned, Ordered Arrays of Silicon Nanowires with a Porous Electrode. *Anal. Chem.* **2011**, *83* (12), 4724–4728. https://doi.org/10.1021/ac200779d.

(25) Zhao, H. Vertical Silicon Nanowire Arrays for Gas Sensing. 97.

(26) Park, H.; Crozier, K. B. Vertically Stacked Photodetector Devices Containing Silicon Nanowires with Engineered Absorption Spectra. *ACS Photonics* **2015**, *2* (4), 544–549. https://doi.org/10.1021/ph500463r.

(27) Park, H.; Dan, Y.; Seo, K.; Yu, Y. J.; Duane, P. K.; Wober, M.; Crozier, K. B. Filter-Free Image Sensor Pixels Comprising Silicon Nanowires with Selective Color Absorption. *Nano Lett.* **2014**, *14* (4), 1804–1809. https://doi.org/10.1021/nl404379w.

(28) Park, H.; Crozier, K. B. Multispectral Imaging with Vertical Silicon Nanowires. *Sci. Rep.* **2013**, *3*, 2460. https://doi.org/10.1038/srep02460.
(29) Kim, W.-K.; Lee, S.; Hee Lee, D.; Hee Park, I.; Seong Bae, J.; Woo Lee, T.; Kim, J.-Y.; Hun Park, J.; Chan Cho, Y.; Ryong Cho, C.; et al. Cu Mesh for Flexible Transparent Conductive Electrodes. *Sci. Rep.* **2015**, *5* (1), 10715. https://doi.org/10.1038/srep10715.
(30) Chang, S.; Oh, J.; Boles, S. T.; Thompson, C. V. Fabrication of Silicon Nanopillar-Based Nanocapacitor Arrays. *Appl. Phys. Lett.* **2010**, *96* (15), 153108. https://doi.org/10.1063/1.3374889.
(31) Cherala, A.; Chopra, M.; Yin, B. A.; Mallavarapu, A.; Singhal, S.; Abed, O.; Bonnecaze, R. T.; Sreenivasan, S. V. Nanoshape Imprint Lithography for Fabrication of Nanowire Ultracapacitors. *IEEE Trans. Nanotechnol.* **2016**, *15*, 448–456. https://doi.org/10.1109/tnano.2016.2541859.
(32) Madsen, M. H.; Hansen, P.-E. Scatterometry—Fast and Robust Measurements of Nano-Textured Surfaces. *Surf. Topogr. Metrol. Prop.* **2016**, *4* (2), 023003. https://doi.org/10.1088/2051-672X/4/2/023003.
(33) Nagasaki, Y.; Suzuki, M.; Takahara, J. All-Dielectric Dual-Color Pixel with Subwavelength Resolution. *Nano Lett.* **2017**, *17* (12), 7500–7506. https://doi.org/10.1021/acs.nanolett.7b03421.
(34) Decker, M.; Staude, I. Resonant Dielectric Nanostructures: A Low-Loss Platform for Functional Nanophotonics. *J. Opt.* **2016**, *18* (10), 103001. https://doi.org/10.1088/2040-8978/18/10/103001.
(35) MOXTEK. Wire-Grid Polarizing Beamsplitters https://moxtek.com/optics-product/polarizing-beamsplitter/ (accessed Nov 5, 2019).
(36) Ahn, S. H.; Miller, M.; Yang, S.; Ganapathisubramanian, M.; Menezes, M.; Singh, V.; Wan, F.; Choi, J.; Xu, F.; LaBrake, D.; et al. High Volume Nanoscale Roll-Based Imprinting Using Jet and Flash Imprint Lithography. 9.
(37) Wu, H.; Kong, D.; Ruan, Z.; Hsu, P.-C.; Wang, S.; Yu, Z.; Carney, T. J.; Hu, L.; Fan, S.; Cui, Y. A Transparent Electrode Based on a Metal Nanotrough Network. *Nat. Nanotechnol.* **2013**, *8* (6), 421–425. https://doi.org/10.1038/nnano.2013.84.
(38) Ghaznavi, Z. Roll-to-Roll Nanofabrication Process for Flexible Cu Metal Mesh Transparent Conducting Electrodes. Masters Thesis. 2019.
(39) Kumar, A.; Zhou, C. The Race To Replace Tin-Doped Indium Oxide: Which Material Will Win? *ACS Nano* **2010**, *4* (1), 11–14. https://doi.org/10.1021/nn901903b.
(40) CMF introduction http://cvrl.ioo.ucl.ac.uk/database/text/intros/introcmfs.htm (accessed Nov 3, 2019).
(41) Colour matching functions http://cvrl.ioo.ucl.ac.uk/cmfs.htm (accessed Nov 3, 2019).
(42) Ford, A.; Roberts, A. Colour Space Conversions. **1998**, 31.
(43) Feature Based Panoramic Image Stitching - MATLAB & Simulink https://www.mathworks.com/help/vision/examples/feature-based-panoramic-image-stitching.html (accessed Nov 3, 2019).
(44) Singhal, S.; Grigas, M. A.; Sreenivasan, S. V. Mechanics-Based Approach for Detection and Measurement of Particle Contamination in Proximity Nanofabrication Processes. *J. Micro Nano-Manuf.* **2016**, *4* (3), 031004. https://doi.org/10.1115/1.4033742.

(45) Bailey, T.; Smith, B.; Choi, B. J.; Colburn, M.; Meissl, M.; Sreenivasan, S. V.; Ekerdt, J. G.; Willson, C. G. Step and Flash Imprint Lithography: Defect Analysis. *J. Vac. Sci. Technol. B Microelectron. Nanometer Struct.* **2001**, *19* (6), 2806. https://doi.org/10.1116/1.1420203.
(46) Groves, T. R. 3 - Electron Beam Lithography. In *Nanolithography*; Feldman, M., Ed.; Woodhead Publishing, 2014; pp 80–115. https://doi.org/10.1533/9780857098757.80.
(47) Armacost, M.; Hoh, P. D.; Wise, R.; Yan, W.; Brown, J. J.; Keller, J. H.; Kaplita, G. A.; Halle, S. D.; Muller, K. P.; Naeem, M. D.; et al. Plasma-Etching Processes for ULSI Semiconductor Circuits. *IBM J. Res. Dev.* **1999**, *43* (1.2), 39–72. https://doi.org/10.1147/rd.431.0039.
(48) Mallavarapu, A. PhD Dissertation, 2020.
(49) Madsen, M. H.; Hansen, P.-E. Imaging Scatterometry for Flexible Measurements of Patterned Areas. *Opt. Express* **2016**, *24* (2), 1109. https://doi.org/10.1364/OE.24.001109.
(50) Faria-Briceno, J. J.; Zhu, R.; Sasidharan, V.; Neumann, A.; Singhal, S.; Sreenivasan, S. V.; Brueck, S. R. J. Optical Angular Scatterometry: In-Line Metrology Approach for Roll-to-Roll and Nanoimprint Fabrication. *J. Vac. Sci. Technol. B* **2019**, *37* (5), 052904. https://doi.org/10.1116/1.5119707.
(51) Hirsch, J.; Curcio, C. A. The Spatial Resolution Capacity of Human Foveal Retina. *Vision Res.* **1989**, *29* (9), 1095–1101. https://doi.org/10.1016/0042-6989(89)90058-8.
(52) Williams, D. R. Seeing through the Photoreceptor Mosaic. *Trends Neurosci.* **1986**, *9*, 193–198. https://doi.org/10.1016/0166-2236(86)90058-5.
(53) XIMEA - New xiSpec Hyperspectral Multi-Linescan Camera model available https://www.ximea.com/en/products-news/hyperspectral-linescan-camera (accessed Nov 3, 2019).
(54) Hyperspectral Imaging. *Delta Optical Thin Film A/S*, 2017.
(55) Communicatie, F. M. &. Resonon, Inc. Pika XC2 Hyperspectral Imaging Camera | Geo-matching.com https://geo-matching.com/thermal-multi-and-hyperspectral-cameras/pika-xc2-hyperspectral-imaging-camera (accessed Nov 3, 2019).